THE PRODUCTION AND EVALUATION OF PHOTODETECTORS FOR THE LHCB RICH SYSTEM AND A STUDY OF THE SENSITIVITY TO VERY RARE HADRONIC B DECAYS

Charlotte Newby
Linacre College

A thesis submitted in partial fulfilment of the
requirements for the degree of Doctor of Philosophy at
the University of Oxford

Trinity Term, 2005

THE PRODUCTION AND EVALUATION OF
PHOTODETECTORS FOR THE LHCB RICH SYSTEM AND A
STUDY OF THE SENSITIVITY TO VERY RARE HADRONIC B
DECAYS

Charlotte Newby
Linacre College

A thesis submitted in partial fulfilment of the requirements for the degree
of Doctor of Philosophy at the University of Oxford

Trinity Term, 2005

Abstract

The LHCb experiment will operate at the Large Hadron Collider (LHC) at CERN which will begin operating in 2007. LHCb will make precision measurements of CP violation in the B system and search for rare B decays. The LHCb Ring Imaging Cherenkov (RICH) system provides the particle identification vital for carrying out these studies. The photodetectors that will be used in the RICH system are Hybrid Photon Detectors (HPD).

In this thesis the production and evaluation of anodes for the first prototype HPDs able to be read out at the at the LHC bunch crossing rate of 40 MHz is described. Two anodes that underwent testing were used to produce two prototype 40MHz HPDs. These HPDs underwent beam tests that took place at CERN in Autumn 2003. These beam tests were performed to evaluate HPD performance and the performance of the aerogel radiator and are compared with expectation.

The RICH is expected to play a vital role in the search for very rare hadronic decays such as $B_d^0 \to K^+K^-$ and $B_s^0 \to \pi^+\pi^-$. The observation of these decay modes is shown to be possible within one year of nominal LHCb operation for assumed branching ratios one tenth that of $B_d^0 \to \pi^+\pi^-$ and $B_s^0 \to K^+K^-$ respectively. By placing tighter requirements on the particle identification provided by the RICH, it is shown that an observation remains possible within the lifetime of the experiment for branching ratios suppressed by a further factor of ten. Finally studies are performed to investigate how well the CP asymmetry could be measured in the decay $B_d^0 \to K^+K^-$.

Acknowledgements

Many people have helped and supported me throughout the course of my DPhil, however I would like to mention those who deserve particular thanks:

Neville Harnew for giving me the opportunity to work with the LHCb group at Oxford and at CERN.

Guy Wilkinson for his excellent supervision, for letting me get on with it and providing support and advice whenever needed.

Nigel Smale for looking after me in my first year at Oxford and for his practical advice on thesis writing.

Ken Wyllie for giving me the opportunity to work with him at CERN and to the rest of the HPD team, who were a pleasure to work with and without whose efforts, the work described in this thesis would not have been possible. Particular thanks to Thierry Gys and Matthias Moritz for their advice and encouragement.

Marta Calvi and Sajan Easo and the rest of the group involved in the aerogel beam test, whose advice and understanding was indispensable.

My family and friends who have supported me throughout. In particular my mother, who has given endless support and advice; Frin, who was in it with me all the way; Dan, for listening, helping and encouraging me to keep going and Jonas Rademacker for his B physics knowledge and for all his help.

Table of Contents

List of Figures

List of Tables

Chapter 1

CP Violation

1.1 Introduction

The Standard Model of particle physics provides a complete description of the fundamental particles and their interactions. A review of the Standard Model can be found in [eid04] . The discovery of the Higgs boson is awaited to verify the Standard Model experimentally, yet it is already clear that it must be extended to include gravity and massive neutrinos. The LHC will allow the investigation of a new energy scale which is expected to reveal not only the mechanism by which particles acquire mass through the discovery of the Higgs boson but also other new physics beyond the Standard Model such as supersymmetry [eli04].

The parity operation, P, reverses the sign of all spatial coordinates and, up until 1957 when it was shown not to be conserved in beta decay of Cobalt-60 [wu57], this was thought to be a symmetry of the weak interaction. Following this discovery it was thought that the weak interaction was symmetric under the combined operation of P and charge conjugation, C, where the C operation reverses the electric charge and all internal quantum numbers. However, in 1964 CP violation was observed in kaon decays [chr64] and has since been seen in the B sector. The mechanism for CP violation is included in the Standard Model and studies of CP violation in the

B sector test this description and attempt to over-constrain the parameters involved. This work has been started by the Babar and Belle experiments operating at the $\Upsilon(4S)$ resonance (the so-called "B factories") and will be continued at LHCb. The large $b\overline{b}$ cross section of the LHC will provide a larger sample of B mesons to study and LHCb will also have access to the B_s sector which is unavailable at the B factories.

Measurements of the parameters that describe CP violation in the Standard Model test the theory. Any discrepancies that appear in the measurements of these parameters obtained by different methods could indicate the presence of New Physics. An indication that new contributions should be expected already exists: the universe contains more matter than anti-matter. If we assume that the universe had equal amounts of matter and anti-matter when it began, this asymmetry must have been generated by a process termed baryogenesis. In order to generate a matter-antimatter asymmetry the baryogenetic mechanism must violate CP [sak67]. The level of CP violation that the Standard Model predicts would not be sufficient to generate this asymmetry [har98], thus indicating sources of CP violation beyond the Standard Model.

In the following section discrete symmetries and CP violation will be discussed in more detail. This is followed by a derivation, in general terms, of the phenomenology of neutral B mesons including how mixing and CP violation occur. This is then put into the context of the Standard Model and in particular the CKM matrix. Finally the importance of charmless B meson decays is discussed, paying particular attention to the rare decays $B_d \to K^+K^-$ and $B_s \to \pi^+\pi^-$. A measurement of these channels would provide useful insight into the charmless B decay process and be a useful tool when trying to extract the unitarity triangle angle γ from such decays. The unitarity triangle is introduced in section 1.4.1.

1.2 Charge Conjugation, Parity and Time Reversal

Physical laws are invariant under translations in time, space and rotations and these continuous symmetry operations imply the conservation of energy, linear momentum and angular momentum respectively. Another set of symmetry operations are discrete symmetries. Three of these are Charge Conjugation, C, Parity, P, and Time Reversal, T. C is to change particle into anti-particle, P is the inversion of all spatial coordinates, $(x \to -x, y \to -y, z \to -z)$, and T reverses the direction of time and therefore the direction of motion. Although conserved in strong and electromagnetic interactions, P and C are violated in weak interactions. P was first shown to be violated in beta decay of cobalt atoms [wu57]. In addition, although most weak interactions are invariant under the combined operation CP, CP violation is observed in the decay of neutral K and B mesons [chr64], [bab01], [bel01]. CPT is an exact symmetry of a quantum field theory thus retaining Lorentz invariance and causality. CPT invariance can be tested for instance by comparing the mass of K^0 mesons and $\bar{K}^0$ with the result

$\left|m_{\bar{K}^0} - m_{K^0}/m_{K^0}\right| < 10^{-18}$ at 95% confidence level [eid04]. If CPT is conserved, but CP violated, then T symmetry is also violated in weak decays.

1.3 Neutral B Mesons: mixing and CP violation

1.3.1 Introduction

Two types of neutral B meson produced at the LHC are studied in this thesis. B_d mesons and B_s mesons each contain one b-type quark and one d or s-type quark respectively. The flavour eigenstates of these systems are:

$$B_d = (\bar{b}, d), \bar{B}_d = (b, \bar{d});$$
$$B_s = (\bar{b}, s), \bar{B}_s = (b, \bar{s}). \tag{1.1}$$

The flavour eigenstates are not CP eigenstates however the linear combinations,

$$\left|B_1^0\right\rangle = \frac{1}{\sqrt{2}}(\left|B^0\right\rangle - \left|\bar{B}^0\right\rangle)$$
$$\left|B_2^0\right\rangle = \frac{1}{\sqrt{2}}(\left|B^0\right\rangle + \left|\bar{B}^0\right\rangle) \tag{1.2}$$

are CP eigenstates. Flavour eigenstates are also not eigenstates of the Hamiltonian which have definite mass and lifetime. The flavour eigenstates mix to form the mass eigenstates B_H and B_L.

$$B_{H,L} = p\left|B_{d,s}\right\rangle \mp q\left|\bar{B}_{d,s}\right\rangle \tag{1.3}$$

where the subscripts H and L denote the "heavy" and "light" physical states and the complex coefficients p and q obey the following normalisation condition

$$|p|^2 + |q|^2 = 1. \qquad 1.4$$

If CP is conserved, the mass eigenstates are identical to the CP eigenstates. CP violation can manifest itself in three ways. There can be CP violation in the decay, where the amplitude for a decay and its CP conjugate process have different magnitudes. As B_H and B_L are not CP eigenstates then there is in principle CP violation in the mixing if $|q/p| \neq 1$, however this is expected to be negligible in the B sector. The manifestation of CP violation that is relevant to this thesis is CP violation in the interference between decays with and without mixing. This can be seen when $B_{d,s}$ and $\overline{B}_{d,s}$ decay into the same final state.

1.3.2 Mixing of B mesons

For an unstable particle with mass M and lifetime, $\tau = 1/\Gamma$, the Schrödinger equation for an arbitrary linear superposition of the flavour eigenstates, $a|B_{d,s}\rangle + b|\overline{B}_{d,s}\rangle$ is:

$$i\frac{d}{dt}\begin{pmatrix} a \\ b \end{pmatrix} = H\begin{pmatrix} a \\ b \end{pmatrix} = (M - \frac{i}{2}\Gamma)\begin{pmatrix} a \\ b \end{pmatrix} \qquad 1.5$$

where M and Γ are Hermitian matrices so that their off diagonal elements are complex conjugates of each other. It should be noted that H is not Hermitian as the $B^0_{d,s} - \overline{B}^0_{d,s}$ system decays and therefore probability is not conserved.

CPT invariance guarantees that particles and anti-particles have equal masses and lifetimes giving:

$$\mathrm{i}\frac{\mathrm{d}}{\mathrm{dt}}\begin{pmatrix} a \\ b \end{pmatrix} = \begin{pmatrix} M_{11} - \frac{i}{2}\Gamma_{11} & M_{12} - \frac{i}{2}\Gamma_{12} \\ M_{12}^{*} - \frac{i}{2}\Gamma_{12}^{*} & M_{11} - \frac{i}{2}\Gamma_{11} \end{pmatrix}\begin{pmatrix} a \\ b \end{pmatrix}. \qquad 1.6$$

The difference in mass and lifetime between the two mass eigenstates is here defined to be

$$\left.\begin{aligned} \Delta m &\equiv M_H - M_L \\ \Delta\Gamma &\equiv \Gamma_H - \Gamma_L. \end{aligned}\right. \qquad 1.7$$

Finding the eigenvalues of Equation 1.5

$$(M_{11} - i\Gamma_{11} - \lambda) - F^2 = 0\text{, where, } F = \sqrt{(M_{12} - i\Gamma_{12})(M_{12}^{*} - i\Gamma_{12}^{*})} \qquad 1.8$$

gives $\lambda_{H,L} = (M_{11} - \frac{i}{2}\Gamma_{11}) \pm F$. Writing the eigenvalues as $\lambda_{H,L} = M_{H,L} - \frac{i}{2}\Gamma_{H,L}$ and equating real and imaginary parts gives:

$$M_H = M_{11} + \mathcal{R}e F,\ M_L = M_{11} - \mathcal{R}e F \qquad 1.9$$

$$\Gamma_H = \Gamma_{11} - 2\mathit{Im}F,\ \Gamma_L = \Gamma_{11} + 2\mathit{Im}F \qquad 1.10$$

The difference in mass and width of the two mass eigenstates are given by:

$$\Delta m = 2\mathcal{R}e F \qquad 1.11$$

$$\Delta\Gamma = -4\mathit{Im}F, \qquad 1.12$$

which gives

$$\Delta m - \frac{i}{2}\Delta\Gamma = 2F. \qquad 1.13$$

The mass eigenstates B_H and B_L are given in equation 1.3.

The eigenvectors are:

$$\bar{\upsilon}_{H,L} = \begin{pmatrix} p \\ \mp q \end{pmatrix} \qquad 1.14$$

with

$$\begin{aligned}
\frac{q}{p} &= -\frac{F}{M_{12} - \frac{i}{2}\Gamma_{12}} \\
&= -\frac{\frac{1}{2}(\Delta m - \frac{i}{2}\Delta\Gamma)}{M_{12} - \frac{i}{2}\Gamma_{12}} \\
&= -\frac{M_{12}^{*} - \frac{i}{2}\Gamma_{12}^{*}}{\frac{1}{2}(\Delta m - \frac{i}{2}\Delta\Gamma)}.
\end{aligned} \qquad 1.15$$

1.3.3 Time evolution of neutral B mesons

With knowledge of the relationship between the mass and flavour eigenstates it is possible to deduce how the $B_{d,s}$ and $\overline{B}_{d,s}$ evolve in time. From Equation 1.3 one obtains

$$\begin{aligned}
\left|B_{d,s}\right\rangle &= \frac{1}{2p}\left[\left|B_H\right\rangle + \left|B_L\right\rangle\right] \\
\left|\overline{B}_{d,s}\right\rangle &= \frac{1}{2q}\left[-\left|B_H\right\rangle + \left|B_L\right\rangle\right].
\end{aligned} \qquad 1.16$$

The time evolution of the flavour eigenstates depends on the time evolution of the mass eigenstates which is trivially shown to be

$$\left|B_{H,L}(t)\right\rangle = e^{-i(M_{H,L} - \frac{i}{2}\Gamma_{H,L})t}\left|B_{H,L}\right\rangle. \qquad 1.17$$

Again using Equation 1.3 one obtains

$$\begin{aligned}
\left|B_H(t)\right\rangle &= e^{-i(M_H - \frac{i}{2}\Gamma_H)t}\left(p\left|B_{d,s}\right\rangle - q\left|\overline{B}_{d,s}\right\rangle\right) \\
\left|B_L(t)\right\rangle &= e^{-i(M_L - \frac{i}{2}\Gamma_L)t}\left(p\left|B_{d,s}\right\rangle + q\left|\overline{B}_{d,s}\right\rangle\right).
\end{aligned} \qquad 1.18$$

Substituting this into the time-dependent version of Equation 1.4 gives

$$\begin{aligned} \left|B_{d,s}(t)\right\rangle &= \frac{1}{2p}\left[e^{-i(M_H-\frac{i}{2}\Gamma_H)t}\left(p\left|B_{d,s}\right\rangle - q\left|\overline{B}_{d,s}\right\rangle\right) + e^{-i(M_L-\frac{i}{2}\Gamma_L)t}\left(p\left|B_{d,s}\right\rangle + q\left|\overline{B}_{d,s}\right\rangle\right)\right] \\ \left|\overline{B}_{d,s}(t)\right\rangle &= \frac{1}{2q}\left[e^{-i(M_L-\frac{i}{2}\Gamma_L)t}\left(p\left|B_{d,s}\right\rangle + q\left|\overline{B}_{d,s}\right\rangle\right) - e^{-i(M_H-\frac{i}{2}\Gamma_H)t}\left(p\left|B_{d,s}\right\rangle - q\left|\overline{B}_{d,s}\right\rangle\right)\right] \end{aligned} \tag{1.19}$$

In the B_d system these equations can be simplified as $\Delta\Gamma \approx 0$. They therefore become

$$\begin{aligned} \left|B(t)\right\rangle &= \frac{1}{2}e^{-\frac{\Gamma t}{2}}\left[e^{-iM_H t}\left(\left|B\right\rangle - \frac{q}{p}\left|\overline{B}\right\rangle\right) - e^{-iM_L t}\left(\left|B\right\rangle + \frac{q}{p}\left|\overline{B}\right\rangle\right)\right] \\ \left|\overline{B}(t)\right\rangle &= \frac{1}{2}e^{-\frac{\Gamma t}{2}}\left[e^{-iM_H t}\left(\frac{p}{q}\left|B\right\rangle - \left|\overline{B}\right\rangle\right) + e^{-iM_L t}\left(\frac{p}{q}\left|B\right\rangle + \left|\overline{B}\right\rangle\right)\right]. \end{aligned} \tag{1.20}$$

The first equation describes the time evolution of a particle that is created as a B_d at t = 0 and the second describes the time evolution of a particle that is created as a $\overline{B}_d$ at t = 0. If A_f is the amplitude for B_d to decay to the final state f and $\overline{A}_f$ is the amplitude for $\overline{B}_d$ to decay to the same final state,

$$\begin{aligned} A_f(t) &= \frac{1}{2}e^{-\frac{\Gamma t}{2}}\left[e^{-iM_H t}\left(A_f - \frac{q}{p}\overline{A}_f\right) - e^{-iM_L t}\left(A_f + \frac{q}{p}\overline{A}_f\right)\right] \\ &= \frac{1}{2}e^{-\frac{\Gamma t}{2}}A_f\left[e^{-iM_H t}\left(1 - \frac{q}{p}\frac{\overline{A}_f}{A_f}\right) - e^{-iM_L t}\left(1 + \frac{q}{p}\frac{\overline{A}_f}{A_f}\right)\right] \end{aligned} \tag{1.21}$$

The decay rate is the square of this amplitude which gives

$$\begin{aligned} \left|A_f(t)\right|^2 = \Gamma(B_d \to f) = \frac{1}{4}e^{-\Gamma t}\left|A_f\right|^2\Big[2 + 2\left|\lambda_f\right|^2 &+ (1 - \lambda_f + \lambda_f^{\,*} - \left|\lambda_f\right|^2)e^{-i\Delta mt} \\ &+ (1 + \lambda_f - \lambda_f^{\,*} - \left|\lambda_f\right|^2)e^{+i\Delta mt}\Big] \end{aligned} \tag{1.22}$$

where $\lambda_f = \frac{q}{p}\frac{\overline{A}_f}{A_f}$.

This expression becomes

$$\Gamma(\mathrm{B_d} \to \mathrm{f}) = \frac{1}{2} e^{-\Gamma t} \left|\mathrm{A_f}\right|^2 \Big[1 + \left|\lambda_f\right|^2 + (1 - \left|\lambda_f\right|^2) \cos(\Delta \mathrm{mt}) \\ -2 Im(\lambda_f) \sin(\Delta \mathrm{mt}) \Big]. \qquad 1.23$$

The corresponding expression for the decay rate of a state that is created as $\overline{\mathrm{B}}_{\mathrm{d}}$ at time t=0 is

$$\Gamma(\overline{\mathrm{B}}_{\mathrm{d}} \to \mathrm{f}) = \frac{1}{2} e^{-\Gamma t} \left|\mathrm{A_f}\right|^2 \Big[1 + \left|\lambda_f\right|^2 + (1 - \left|\lambda_f\right|^2) \cos(\Delta \mathrm{mt}) \\ + 2 Im(\lambda_f) \sin(\Delta \mathrm{mt}) \Big]. \qquad 1.24$$

1.3.4 Asymmetry measurement

In order to search for CP violation in the neutral B meson system one typically studies the time dependent asymmetry between the decay of $\mathrm{B_{d,s}}$ and $\overline{\mathrm{B}}_{\mathrm{d,s}}$ mesons into a CP eigenstate state f. The quantity that is measured is the asymmetry between the decay rates to the final state f for $\mathrm{B_{d,s}}$ and $\overline{\mathrm{B}}_{\mathrm{d,s}}$. This is given by

$$\mathrm{A_{CP}}(\mathrm{t}) = \frac{\Gamma(\mathrm{B_{d,s}} \to \mathrm{f}) - \Gamma(\overline{\mathrm{B}}_{\mathrm{d,s}} \to \mathrm{f})}{\Gamma(\mathrm{B_{d,s}} \to \mathrm{f}) + \Gamma(\overline{\mathrm{B}}_{\mathrm{d,s}} \to \mathrm{f})}. \qquad 1.25$$

In the $\mathrm{B_d}$ system, using equations 1.23 and 1.24 this can be written

$$\mathrm{A_{CP}}(\mathrm{t}) = \frac{(1 - \left|\lambda_f\right|^2) \cos(\Delta \mathrm{mt}) + 2 Im(\lambda_f) \sin(\Delta \mathrm{mt})}{1 + \left|\lambda_f\right|^2}$$

$$= \mathrm{A} \cos(\Delta \mathrm{mt}) + \mathrm{B} \sin(\Delta \mathrm{mt})$$

1.26

1.27

Figure 1-1: The B_d can decay directly to the final state f or can first oscillate into a $\overline{B}_d$

where $A = \left(1-\left|\lambda_f\right|^2\right)\Big/1+\left|\lambda_f\right|^2$ and $B = 2Im(\lambda_f)/1+\left|\lambda_f\right|$. The quantity Δm_d is determined from the proper time distributions of B_d candidates and the average of all current measurements [eid04] is

$$\Delta m_d = 0.505 \pm 0.005 \text{ ps}^{-1}. \qquad 1.28$$

The phase difference between the two decay paths shown in Figure 1-1 is measured and can be accessed through the parameters A and B as it is related to the phase of λ_f. A_{CP} will be non-zero firstly if the value of $\lambda_f \neq 1$, leading to the cosine term being non-zero. The quantity λ_f is defined in equation 1.22; assuming no CP violation in the mixing, $\lambda_f \neq 1$ if $\left|\overline{A}_f/A_f\right| \neq 1$, which would occur if there were CP violation in the decay. The possibility remains that $\lambda_f = 1$, yet $Im\lambda_f \neq 0$ which would occur if there were interference between decays with and without mixing and would lead to A_{CP} being non-zero. This latter possibility is the one that occurs in the “golden channel” $B_d \rightarrow J/\psi K_s$ as discussed in section 1.4.2.

It should be noted that the simplification $\Delta\Gamma \approx 0$, made above for the B_d system, is not valid in the B_s system as $\left|\Delta\Gamma_s/\Gamma_s\right|$ is expected to be of the order of 10% [vag203]. In addition the value of Δm_s is larger than Δm_d resulting in a much shorter oscillation period to resolve. A measurement of this quantity is yet to be made with the current experimental limit being

$$\Delta m_s > 14.5\ \mathrm{ps}^{-1} \qquad 1.29$$

at 95% confidence level [ckm05]. In the B_s case the expression for the asymmetry is

$$A_{CP}(t) = \frac{A\cos(\Delta m t) + B\sin(\Delta m t)}{\cosh\left(\frac{\Delta\Gamma}{2}t\right) - C\sinh\left(\frac{\Delta\Gamma}{2}t\right)} \qquad 1.30$$

where $C = \frac{2Re(\lambda_f)}{1+\left|\lambda_f\right|^2}$ [vag203].

1.4 CP Violation in the Standard Model

1.4.1 The CKM matrix and the unitarity triangle

In the Glashow-Weinberg-Salam model of electroweak interactions [gla61], [wei67], [sal68], quarks are represented by weak isodoublets of left handed quarks and isosinglets of right handed quarks. Quarks within an isodoublet transform into each other under weak isospin transformations, for example

$$q_L = \begin{pmatrix} u \\ \tilde{d} \end{pmatrix}_L, \qquad 1.31$$

where L indicates that the doublet is left-handed. The u-quark has weak isospin quantum number $I_3 = +1/2$ and the d-quark has weak isospin $I_3 = -1/2$. These eigenstates of the weak interaction are not the same as the quark mass eigenstates and in fact the quarks that undergo weak interactions are, in general, superpositions of the mass eigenstates. In the case of down-type quarks, the mass eigenstates and weak eigenstates are related to each other by the Cabibbo-Kobayashi-Maskawa (CKM) matrix [cab63], [kob72].

$$\begin{pmatrix} \tilde{d} \\ \tilde{s} \\ \tilde{b} \end{pmatrix} = V_{CKM} \begin{pmatrix} d \\ s \\ b \end{pmatrix} \qquad 1.32$$

where $V_{CKM} = \begin{pmatrix} V_{ud} & V_{us} & V_{ub} \\ V_{cd} & V_{cs} & V_{cb} \\ V_{td} & V_{ts} & V_{tb} \end{pmatrix}$.

The CKM matrix must be unitary giving

$$V_{CKM} V_{CKM}^{\dagger} = \mathbf{I}, \qquad 1.33$$

where **I** is the identity matrix. This leads to 9 unitarity conditions, six of which can be represented as triangles in the complex plane whose three sides add up to 0. These relations are,

$$\begin{gathered} V_{ud}^{*} V_{us} + V_{cd}^{*} V_{cs} + V_{td}^{*} V_{ts} = 0, \\ V_{cd}^{*} V_{ud} + V_{cs}^{*} V_{us} + V_{cb}^{*} V_{ub} = 0, \\ V_{us}^{*} V_{ub} + V_{cs}^{*} V_{cb} + V_{ts}^{*} V_{tb} = 0, \\ V_{cd}^{*} V_{td} + V_{cs}^{*} V_{ts} + V_{cb}^{*} V_{tb} = 0, \\ V_{ud}^{*} V_{td} + V_{us}^{*} V_{ts} + V_{ub}^{*} V_{tb} = 0, \\ V_{ub}^{*} V_{ud} + V_{cb}^{*} V_{cd} + V_{tb}^{*} V_{td} = 0. \end{gathered}$$

Figure 1-2: The unitarity triangle which represents $\mathrm{V}_{\mathrm{ub}}^{*}\mathrm{V}_{\mathrm{ud}}+\mathrm{V}_{\mathrm{cb}}^{*}\mathrm{V}_{\mathrm{cd}}+\mathrm{V}_{\mathrm{tb}}^{*}\mathrm{V}_{\mathrm{td}}=0$ as a triangle in the complex plane. The triangle has been re-scaled by dividing by $\left|\mathrm{V}_{\mathrm{cd}}\mathrm{V}_{\mathrm{cb}}^{*}\right|$ and the coordinates of the apex are (ρ,η).

Without CP violation all elements are real and the area of each of these triangles would be zero. Only the last two of the six relations yield non-trivial triangles where all of the sides are of the same magnitude. This can be seen when considering the Wolfenstein parametrization [wol83] of the CKM matrix,

$$\mathrm{V}_{\mathrm{CKM}}=\begin{pmatrix} 1-\lambda^{2}/2 & \lambda & \mathrm{A}\lambda^{3}(\rho-\mathrm{i}\eta) \\ -\lambda & 1-\lambda^{2}/2 & \mathrm{A}\lambda^{2} \\ \mathrm{A}\lambda^{3}(1-\rho-i\eta) & -\mathrm{A}\lambda^{2} & 1 \end{pmatrix}+O(\lambda^{4}). \qquad 1.35$$

where $\lambda=\sin\theta_C=0.22$ with θ_C being the Cabibbo angle. A, ρ and η are real parameters and η parametrises a CP violating phase. The two non trivial unitarity triangles coincide up to $O(\lambda^3)$. The unitarity triangle is shown in Figure 1-2. The angles β and γ are defined as shown with the third angle α defined as $\alpha = \pi - (\beta+\gamma)$. It can be seen in from expression 1.35 that up to

$O(\lambda^3)$ there are only two complex elements of the CKM matrix, V_{td} and V_{ub}. These elements have phases $-\beta$ and $-\gamma$.

1.4.2 Existing constraints

The existing constraints on the elements of the CKM matrix and the parameters of the unitarity triangle are summarised here. Values are taken from [eid04] and [ckm05]:

- $|V_{ud}|$ = 0.9738 ± 0.0005 from nuclear β decay and neutron decay.

- $|V_{us}|$ = 0.2200 ± 0.0026 from semi-leptonic kaon decays.

- $|V_{cd}|$ = 0.224 ± 0.0012 from di-muon production in deep inelastic scattering (DIS) of neutrinos and anti-neutrinos on neutrons.

- $|V_{cs}|$ = 1.04 ± 0.16 also from DIS of neutrinos and semi-leptonic D decays.

- $|V_{cs}|$ = 0.996 ± 0.013 determined by considering the ratio of hadronic W decays to leptonic decays. This measurement assumes 3 generations and it tests unitarity rather than constrain $|V_{cs}|$.

- $|V_{cb}|$ = 0.0413 ± 0.0015 from semi-leptonic B decays.

- $|V_{ub}|$ = 0.00367 ± 0.00047 from semi-leptonic B decays.

- $\frac{|V_{tb}|^2}{|V_{td}|^2+|V_{ts}|^2+|V_{tb}|^2} = 0.94^{+0.31}_{-0.24}$ from semi-leptonic top decays.

The data do not rule out the possibility of the number of generations being greater than 3. However, assuming 3 generations and imposing the unitarity of the matrix, the limits on the 9 CKM elements are as follows:

$$\begin{pmatrix} 0.9739-0.9751 & 0.221-0.227 & 0.0029-0.0045 \\ 0.221-0.227 & 0.9730-0.9744 & 0.039-0.044 \\ 0.0048-0.014 & 0.037-0.043 & 0.9990-0.9992 \end{pmatrix}. \qquad 1.36$$

The current knowledge of Δm_d and Δm_s given in equations 1.28 and 1.29 leads to the following constraint on one side of the unitarity triangle:

$$|V_{tb}^* \cdot V_{td}| = 0.0083 \pm 0.0016 \qquad 1.37$$

and also

$$\frac{|V_{td}|}{|V_{ts}|} < 0.25. \qquad 1.38$$

In addition, assuming 3 generations implies $|V_{ts}| \approx |V_{cb}|$ which gives $|V_{td}| < 0.011$.

All of the above concern measurements of the magnitudes of CKM elements. In addition to these there exist measurements of actual CP violating effects which constrain the position of the apex of the triangle, and the internal angles.

A measurement of

$$\varepsilon_K = \frac{2}{3}\eta_{+-} + \frac{1}{3}\eta_{00} \qquad 1.39$$

where η_{+-} and η_{00} are the amplitudes of K_L^0 to K_S^0 decaying to pairs of charged and neutral pions respectively, helps constrain the unitarity triangle further. The average value $|\varepsilon_K| = (2.282 \pm 0.017) \times 10^{-3}$ constrains the apex of the triangle to the hyperbola seen in Figure 1-3.

At this time the best measurements of the quantity sin2β come from the Babar and Belle experiments from measurements of $B_d \rightarrow J/\psi K_s$. Their results when averaged give sin2β = 0.736 ± 0.049. As discussed in section 1.3.4, in this channel there is CP violation in the interference between mixing and decay. This result provides a benchmark for such CP violating

Figure 1-3: Global CKM fit. Shaded areas show confidence levels ≥ 5%. The fit includes the constraints on $|V_{ub}|, |V_{us}|, |V_{cd}|, |V_{cs}|, |V_{cb}|, |V_{ub}|, |\varepsilon_K|, \Delta m_d, \Delta m_s, |V_{ts}|, \sin 2\beta$ and $\sin 2\alpha$.

Figure 1-4: Box diagrams representing the mixing of B mesons, by replacing all d quarks with an s quark one obtains the mixing diagram for B_s mesons.

effects in the Standard Model. The decay $B \rightarrow \rho\rho$ provides the current best measurement of the angle $\alpha = (94 \pm 19)^{\circ}$ for confidence level greater than 90%. No precise measurements have yet been made of the angle γ, although initial studies in $B_d \rightarrow DK$ decays appear promising.

The constraints on the unitarity triangle from the latest measurements, as shown in [ckm05] in April 2005, are seen in Figure 1-3.

1.5 Two-body charmless B decays

The two parameters in the CKM matrix which involve significant complex components and therefore provide access to the angles of the Unitarity Triangle are V_{ub} and V_{td}. V_{td} is involved in the mixing "box" diagram shown in Figure 1-4. The figure shows the process by which the mixing discussed in 1.3.2 occurs. Charmless two-body decays involve the second element, V_{ub}, as is shown in Figure 1-5, showing the tree diagram for the decay $B_d \rightarrow \pi^+\pi^-$.

1.5.1 Charmless B decays and α

Decays such as $B_d \to \pi^+\pi^-$ are traditionally thought of as a way to access the CKM angle α. A measurement of the asymmetry defined in Equation 1.26 results in the determination of a value for $\lambda_f = \frac{q}{p}\frac{\overline{A}_f}{A_f}$. In the B_d system $\Delta\Gamma_B << \Delta m_B$ and equation simplifies as

$$\frac{q}{p} = -\frac{M_{12}^*}{|M_{12}|}. \qquad 1.40$$

The matrix element M_{12} receives contribution from all up-type quarks, however these contributions depend on m^2. Hence in the Standard Model the top contributions are dominant with,

$$\frac{q}{p} = \frac{V_{tb}^* V_{td}}{V_{tb} V_{td}^*} e^{2i\xi_B}. \qquad 1.41$$

The phase ξ_B is arbitrary. The ratio of the amplitudes of the final state $\pi^+\pi^-$ are given by

1.42

Figure 1-5: Feynman diagram of the tree decay $B_d \to \pi^+\pi^-$

$$\frac{\overline{\mathrm{A}}_{\pi\pi}}{\mathrm{A}_{\pi\pi}} = \eta_{\pi\pi} \frac{\mathrm{V}_{\mathrm{ub}}\mathrm{V}_{\mathrm{ud}}^{*}}{\mathrm{V}_{\mathrm{ub}}^{*}\mathrm{V}_{\mathrm{ud}}} \mathrm{e}^{-2i\xi_B} ,$$

where $\eta_{\pi\pi}$ is the CP eigenstate, which is equal to 1 and it is assumed there are no phase differences between the mixing and tree diagrams. This gives

$$\lambda_{\pi\pi} = \left(\frac{\mathrm{V}_{\mathrm{tb}}^{*}\mathrm{V}_{\mathrm{td}}}{\mathrm{V}_{\mathrm{tb}}\mathrm{V}_{\mathrm{td}}^{*}}\right)\left(\frac{\mathrm{V}_{\mathrm{ud}}^{*}\mathrm{V}_{\mathrm{ub}}}{\mathrm{V}_{\mathrm{ud}}\mathrm{V}_{\mathrm{ub}}^{*}}\right) = \sin(2\alpha) . \qquad 1.43$$

In reality there are contributions to the amplitude $\mathrm{A}_{\pi\pi}$ other than the tree diagram shown in Figure 1-5. Penguin processes also contribute, the Feynman diagram for which can be seen in Figure 1-6. The quark in the virtual loop in Figure 1-6 can be either u, c or t, however once more the contribution form the t quark dominates. Although the weak parts of the amplitude and phase are easily calculable the hadronic parts are not, resulting in an unknown contribution to both. Therefore α cannot be easily extracted

Figure 1-6: Feynman diagram of the penguin decay $\mathrm{B}_{\mathrm{d}} \rightarrow \pi^{+}\pi^{-}$

from the measurement.

An alternative method has been suggested [fle99], [fle04] where the results from $B_d \rightarrow \pi^+\pi^-$ are combined with either those from $B_s \rightarrow K^+K^-$ or $B_d \rightarrow K\pi$ in order to extract the angle γ. The method uses as an input the angle β as measured through the "Golden-channel" $B_d \rightarrow J/\psi K_s$ and exploits the fact that the decays $B_d \rightarrow \pi^+\pi^-$ and $B_s \rightarrow K^+K^-$ are identical under an interchange of down and strange quarks. The decay $B_d \rightarrow K^+\pi^-$ may be used as an alternative to $B_s \rightarrow K^+K^-$ as these two decays differ only by the flavour of the spectator quark involved.

1.5.2 Relative branching ratios

The method for extracting the angle γ involves the comparison of two topologically similar decay channels. The branching ratios of these decay channels are significantly different due to the different quark transitions involved. The decay $B_d \rightarrow K^+\pi^-$ has a tree and penguin contribution the diagrams for which are identical to those shown in Figure 1-5 and Figure 1-6 but with the non-spectator d quark replaced by an s quark.

With reference to the Wolfenstein parameterisation of the CKM matrix in equation 1.8, it can be seen that in the $B_d \rightarrow K^+\pi^-$ decay the penguin diagram is dominant as it involves V_{tb} and V_{ts} whereas the tree decay involves the doubly Cabibbo suppressed transition $b \rightarrow u$. In turn the decay

$B_d \to \pi^+\pi^-$ is suppressed with respect to $B_d \to K^+\pi^-$ as b→u and t→d transitions are involved in both tree and penguin diagrams. Measurements indicate that $BR(B_d \to K^+\pi^-) \approx 4\times BR(B_d \to \pi^+\pi^-)$ [eid04].

Other charmless two-body decays are considered in this thesis and in some cases a measurement of the branching ratio has not yet been made.

	# Events	**Branching Ratio ($\times 10^{-6}$)**	**Comment**
$B_d^0 \to K^+K^-$	40.5k	0.48	Estimated as 1/10 $B_d^0 \to \pi^+\pi^-$
$B_d^0 \to K^+\pi^-$	139.5k	18.5±1.2	Measured
$B_d^0 \to \pi^+\pi^-$	213k	4.8±0.5	Measured
$B_s^0 \to K^+K^-$	39.5k	18.5	Estimated as $B_d^0 \to K^+\pi^-$
$B_s^0 \to \pi^+K^-$	63.5k	4.8	Estimated as $B_d^0 \to \pi^+\pi^-$
$B_s^0 \to \pi^+\pi^-$	28k	1.85	Estimated as 1/10 $B_s^0 \to K^+K^-$
$\Lambda_b \to pK^-$	52.5k	18.5	Estimated as $B_d^0 \to K^+\pi^-$
$\Lambda_b \to p\pi^-$	52k	4.8	Estimated as $B_d^0 \to \pi^+\pi^-$

Table 1.1: Size of the Monte Carlo samples used in the study discussed in Chapter 5, along with the assumed branching ratios. The measured branching ratios are taken from [eid04].

Estimates are made by considering the Cabibbo suppression involved in that particular decay in comparison to $B_d \to \pi^+\pi^-$ and $B_d \to K^+\pi^-$. A summary of the branching ratios assumed in this thesis is given in Table 1.1

1.5.3 $B_d \to K^+K^-$ and $B_s \to \pi^+\pi^-$

The decays $B_d \rightarrow K^+K^-$ and $B_s \rightarrow \pi^+\pi^-$ may only occur via two heavily suppressed exchange and penguin annihilation processes. The Feynman diagrams for these processes are shown in Figure 1-7. These diagrams also contribute to the amplitude for $B_d \rightarrow \pi^+\pi^-$, $B_d \rightarrow K^+\pi^-$ and $B_s \rightarrow K^+K^-$, however their contribution is generally assumed to be negligible. A measurement of the branching ratios of $B_d \rightarrow K^+K^-$ and $B_s \rightarrow \pi^+\pi^-$ will confirm if this assumption is valid. The assumed branching ratios used here for these channels are also given in Table 1.1. If enhanced branching ratios were measured for these channels this could indicate the

Figure 1-7: The two contributions to the amplitude for $B_d \rightarrow K^+K^-$. Interchanging d and s quarks gives the diagrams for $B_s \rightarrow \pi^+\pi^-$.

presence of physics beyond the Standard Model.

In addition to the determination of the contribution these diagrams make to the amplitude of other two-body decays the angle γ can be extracted from the combined measurement of $B_d \rightarrow K^+K^-$ and $B_s \rightarrow \pi^+\pi^-$. The two decays are identical under an interchange of down and strange quarks and therefore it is possible to extract the angle γ using the same method as proposed in [fle04] for $B_d \rightarrow \pi^+\pi^-$ and $B_s \rightarrow K^+K^-$. The precision on the γ found using this method would however be poorer due to the reduced statistics.

1.6 New contributions to CP violation

If physics beyond the Standard Model is present then there may exist a number of heavy particles that have not yet been observed. These particles would make a contribution to loop processes such as the penguin diagram in Figure 1-6. $B_{d,s} \rightarrow \pi^+\pi^-$, $B_{d,s} \rightarrow K^+K^-$ and $B_d \rightarrow K^+\pi^-$ are all affected by penguin processes and for this reason are susceptible to contributions by this new physics. Other theoretically clean methods of measuring the angle γ are available, for example $B_d \rightarrow D^*\pi$. $B_d \rightarrow D^*\pi$ does not suffer from penguin contributions and can also be used to extract the angle γ. A difference in the angle measured in the two cases could indicate the presence of non-Standard Model contributions to the loop diagram.

Chapter 2

The LHCb Experiment

2.1 The LHC

The Large Hadron Collider (LHC) will collide two proton beams with a centre-of-mass energy of 14 TeV and a bunch crossing frequency of 40 MHz. The first collisions will take place in mid 2007. An artist's impression of the LHC is shown in Figure 2-1. With interactions taking place at the TeV energy scale, observations of physics beyond the Standard Model are expected.

Four experiments will operate at the LHC: two general purpose detectors,

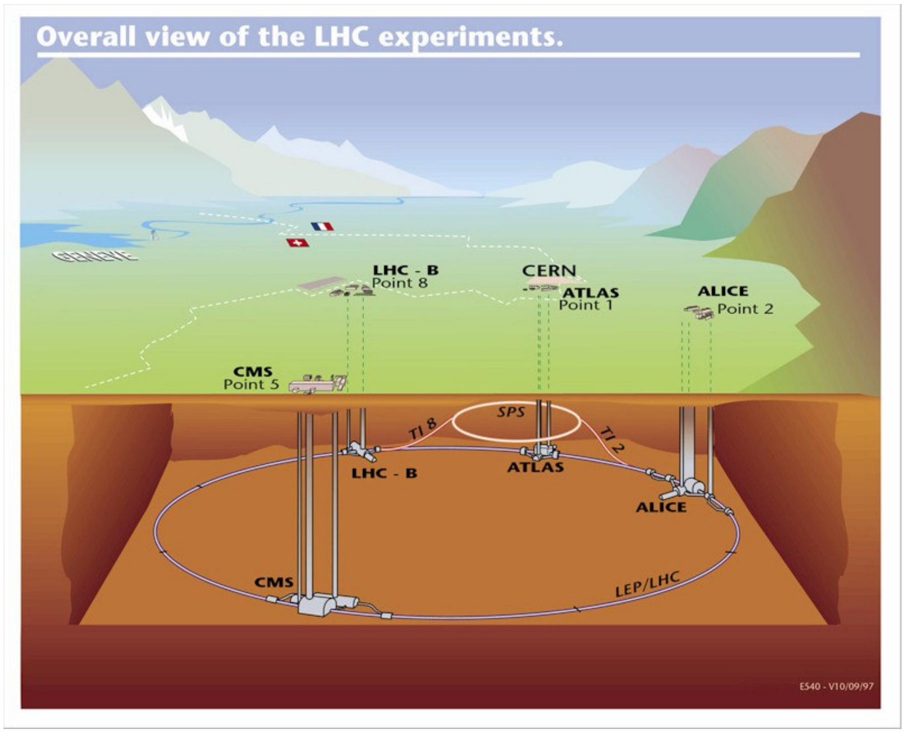

Figure 2-1: An artist's impression of the LHC showing the four interaction points and the SPS, the final component in the acceleration chain that provides the protons to the LHC.

ATLAS (A Toroidal LHC Apparatus) and CMS (Compact Muon Solenoid); a heavy ion experiment, ALICE (A Large Ion Collider Experiment) and a dedicated B-Physics experiment, LHCb. Both ATLAS and CMS will operate at a luminosity of 10^{34} $cm^{-2}s^{-1}$ and focus on searches for the Higgs Boson and direct production of new heavy particles predicted by theories such as supersymmetry. The ALICE experiment is designed to study the collisions of heavy ions which are also possible at the LHC. Particles will interact strongly at high energy densities; in these conditions the formation of a quark-gluon plasma is expected. The properties of this new state of matter will be studied, possibly providing information on the conditions at the beginning of the universe and shedding new light on Quantum Chromodynamics, the theory describing interactions

Figure 2-2: Feynman diagrams of heavy flavour production processes in pp collisions. (a,b) are the leading order processes. (c,d,e) show pair creation, flavour excitation and gluon splitting respectively. (f) shows the process for events classified as gluon splitting, but of flavour excitation in character.

between quarks and gluons. The LHCb experiment is described in detail in the following sections.

2.2 The Experiment

2.2.1 Overview

LHCb will take advantage of the copious number of b-hadrons that will be produced at the LHC. The experiment is designed to make precision measurements of CP violation in the B sector, look for rare B decays and to make some charm physics studies.

The experiment will operate at an average luminosity of $2\times10^{32}\text{cm}^{-2}\text{s}^{-1}$, which is lower than the design luminosity at the ATLAS and CMS interaction points. This will be achieved by de-focusing the beams at the interaction region.

Figure 2-3: Polar angles of b and $\overline{\text{b}}$ with respect to the beam direction. The shaded part represents the direction selected in LHCb

Even at this relatively low luminosity, the high $b\bar{b}$ cross section of 500 μb, will lead to the production of 10^{12} $b\bar{b}$ events per year. The luminosity is chosen such that the number of single proton-proton interactions per bunch crossing is maximised, which simplifies triggering and analysis. With the total inelastic cross section at the LHC being 80 mb, the task is more difficult for ATLAS and CMS who will have up to 20 overlapping interactions in each bunch crossing. The low luminosity running not only has the advantage that LHCb will be able to take data from the beginning of LHC operation, but also that the detector can be designed so that the silicon of the vertex detector approaches to within 1 cm of the beam. At higher luminosity the close proximity of the silicon to the beam would be prohibited by radiation damage considerations.

The processes that lead to the production of bottom quarks in proton-proton

Figure 2-4: The LHCb detector in the non-bending (transverse) plane. Note that the green shading in RICH2 indicates the position of the photodetectors. The orientation of the photodetectors differs in the two RICHes.

collisions include the lowest order processes, gluon-gluon fusion and quark-antiquark annihilation. The Feynman diagrams for all production processes are shown in Figure 2-2. In the parton-parton centre-of-mass frame the quark and anti-quark are produced back-to-back [ell90]. In the lab frame, in the plane transverse to the beam, the quark and anti-quark are also back-to-back. As the quark and gluon constituents carry only a fraction of the total proton momentum and the probability is high that the partons involved in the interaction will have very different momenta. As a result, the quark and anti-quark are boosted along the beam direction and are generally seen in the same cone around the beam, either in the forward or the backward direction. This can be seen in Figure 2-3 where the polar angles of the two b-hadrons are plotted as calculated using the PYTHIA event generator [sjos01]. The LHCb detector has been designed to cover the forward cone[1] and its layout is shown in Figure 2-4. The fact that both quark and anti-quark are found in the same cone is a great advantage as the decay of the non-signal hadron in the event can be used to give an indication of the initial state flavour of the B-hadron of interest. This process is known as flavour tagging. The LHC optics have been modified to displace the interaction point for LHCb such that the asymmetric detector can be accommodated in an existing cavern. This cavern is IP8, previously used by the DELPHI (DEtector with Lepton, Photon and Hadron Identification) experiment.

The experiment has an angular acceptance of 300 mrad (horizontal) × 250 mrad (vertical) and is made up of a number of sub-detectors. Surrounding the interaction region is the VErtex LOcator (VELO). This detector uses silicon micro-strip detectors

---

[1] Although instrumenting both the forward and backward cone would double the statistics, the additional engineering and detector costs were prohibitive.

to measure primary and secondary vertex locations with high accuracy. The two most upstream planes of the VELO are used as a "Pile-up" veto counter used to reject events with more than one primary vertex. The Ring Imaging Cherenkov (RICH) system is used to identify charged particles and comprises of two RICH detectors, one immediately after the VELO (RICH1) and the other downstream of the magnet (RICH2). The dipole magnet provides a magnetic field with a field integral of 4 Tm. Four tracking stations, TT (Trigger Tracker) before the magnet, and T1, T2 and T3 after the magnet provide information on how the particle trajectories are affected by the field. The calorimeters and muon system are furthest away form the interaction point and are used to identify electrons, hadrons and muons for the trigger and offline analysis. In the following sections the components of the LHCb detector are discussed in further detail. Particular attention is paid to the RICH system as much of the work presented in this thesis is directly related to this sub-detector.

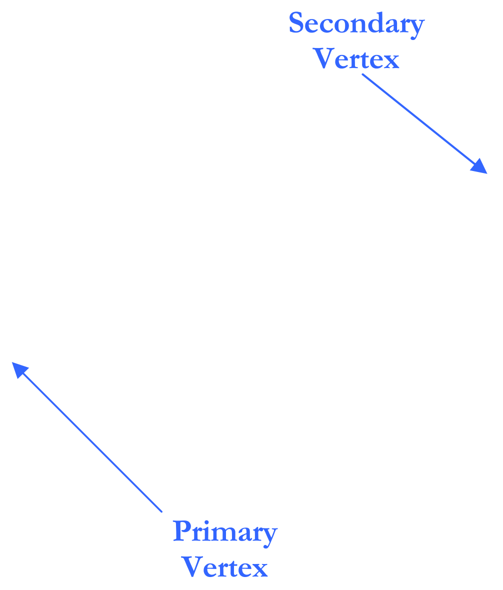

Figure 2-5: A typical B event in LHCb. The distance of flight of the B meson from the primary vertex before decaying is shown by the red arrow.

2.2.2 The Vertex Locator and Pile-up System

When B-hadrons are produced inside the LHCb acceptance they will typically fly ~ 1cm from the primary interaction vertex before decaying. The separation between the secondary and primary vertices sets B-hadron decays of interest apart from other inelastic pp interactions. A schematic of a typical LHCb B-event is shown in Figure 2-5 where this vertex separation can be seen. The VELO has been designed to reconstruct primary and secondary vertices with high precision. In an average event primary vertices are reconstructed with a resolution of 42 μm in the z direction and 10 μm perpendicular to the beam. Impact parameters are measured with a resolution of approximately 20 μm and the resolution on the lifetime of a B-hadron is of the order 40 fs [lhcb03]. The information it provides is used in the Level-1 trigger in order to distinguish B-events from minimum bias events that have passed the Level-0 trigger. Also, vertex separation and impact parameter cuts are used in offline analysis to further

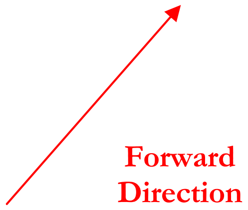

Figure 2-6: Arrangement of detector planes in the VELO. Pile-up veto planes are shown in white.

suppress background. In Chapter 5 details of how this is done for two-body decays and the performance of these cuts are given. Vertex information is also used along with a momentum measurement, to measure the proper lifetime of the B-mesons, which is needed for most CP violation measurements, and must be done with high precision when measuring the rapid oscillation frequency of the B_s.

Figure 2-6 shows the detector arrangement. The VELO is made up of planes of 220 μm thick silicon microstrip sensors placed perpendicular to the beam. Each plane is made up of two detectors placed back-to-back: one with circular strips that measure the r-coordinate of the track and another with radial strips that measure the ϕ-coordinate. The strip pitch has been chosen to ensure that the occupancy per channel varies by no more than a factor of three across the full radius of the detector. The pitch is fine at small radii and increases with radius, resulting in fewer strips at large radii where the occupancy is low. The pitch range is approximately 35 -100 μm.

Two planes of silicon placed upstream of the interaction point are used as a pile-up veto counter; they are shown in white in Figure 2-6. These planes contain circular strips with pitch decreasing with radius. The pile-up veto planes are used to reconstruct the primary vertices so that events containing more than one proton-proton interaction can be rejected. Lines are drawn between the hits on the circular strips and a postulated primary vertex position on the z axis. The number of hits found on the line is histogrammed and the number of peaks found in this histogram gives the number of interactions. It is desirable to veto events containing multiple interactions because background events with two or more interactions are more likely to pass the Level-0

Figure 2-7: A photograph of the LHCb dipole magnet in the LHCb cavern showing members of the collaboration standing at the downstream end of the magnet.

trigger. In addition, signal events containing a second primary vertex are harder to reconstruct offline. In particular they introduce an ambiguity in the proper time reconstruction, as it is not a priori known which primary vertex a B-hadron originated from. It is therefore favourable to reject these events at the earliest opportunity. The calculation of the number of interactions in the event is done quickly enough so that the result can be used in the Level-0 trigger decision. The pile-up veto will reject ~80% of multiple proton-proton interactions and keep ~95% of single interactions [lhcb98].

2.2.3 The tracking stations and the dipole magnet

In order to determine the momentum of particles passing through the LHCb detector, particles are tracked by one station before the magnet (TT) and three stations after the magnet (T1-T3). A dipole magnet is used to provide high magnetic field over a short length with field integral 4 Tm. The dipole magnet is not superconducting and it is therefore possible to invert the polarity of the magnetic field between LHC fills, which will allow some charge dependent systematic errors to be identified and accounted for. A photograph of the magnet after installation in IP8 in 2004 is shown in Figure 2-7.

The first tracking station, TT (trigger tracker), is positioned after RICH 1 and before the dipole magnet. The fringe field on the upstream side of the magnet provides an integrated bending field of 0.15 Tm prior to TT. Hence the deflection observed in this station can be used to calculate the transverse momentum of tracks, information which is used in the Level-1 trigger. After the magnet there are a further three tracking stations, T1, T2 and T3. In order to maintain low occupancy across the detector and minimise cost two different technologies are used in the tracking stations. The TT station and the inner tracker region of the T1-T3 stations, where particle flux is high, use silicon microstrip technology. An outer tracker made using straw tubes surrounds the inner tracker in T1-T3. The detector arrangement in these three stations is shown in Figure 2-9.

Figure 2-8: The arrangement of the four TT detector planes.

Figure 2-9: The detector arrangement of the tracking stations T1-T3. The silicon microstrip detectors (orange) are surrounded by straw tube detectors (blue).

The TT station covers the full detector acceptance and consists of four silicon microstrip detector planes arranged in pairs separated by 30 cm, as shown in Figure 2-8. The silicon strips have a pitch of ~200 μm. The planes are arranged in a *xuvx* configuration where the *x* planes have strips aligned vertically and the *u* and *v* planes have their strips aligned at a stereo angle of +5° and −5° respectively in order to provide a two-dimensional measurement.

A *xuvx* arrangement is again used for the four layers in each of the stations T1-T3, however in this case the layers are equally spaced. The inner tracker silicon detector ladders are arranged in a cross shape around the beam line as seen in Figure 2-9. The straw tube outer tracker consists of cathode tubes, made from an inner layer of Kapton XC and an outer layer of aluminium, surrounding a 25 μm gold anode wire. Each tube is 5 mm in diameter and tubes are arranged with 6 mm pitch. The detector also contains a CF_4 mixture drift gas which ensures fast collection of the drift signals. Charged particles ionize this gas as they pass through and electrons are collected on the anode wires. The drift signals are collected within 50 ns, which is the length of two bunch crossing intervals. The drift time means that the chance is always present that an event accepted by the trigger contains hits from either the previous or the following bunch crossing. The detector performance is assessed in Section 2.6.

2.2.4 The calorimeters

The calorimeters are required to distinguish electrons, photons and hadrons and to provide information about their position and energy. This information is used in the Level-0 trigger and in the offline analysis. The electromagnetic calorimeter (ECAL) is also used to reconstruct photons and π^0 mesons that may come from some B-decay channels. The calorimeters are designed to have resolutions of

$$\frac{\sigma(E)}{E} = \frac{10\%}{\sqrt{E}} \oplus 1.5\%$$
$$\frac{\sigma(E)}{E} = \frac{80\%}{\sqrt{E}} \oplus 10\%$$

for the electromagnetic calorimeter and hadron calorimeter (I 2.1 ectively [lhcb00]. The resolutions are sufficient to provide the necessary hadron rejection in the ECAL, as well as π^0 reconstruction.

The ECAL is a "shashlik" calorimeter made of layers of lead and scinitillator read out using wave length shifting optical fibres. There are 70 alternating layers in the ECAL of 2mm thick lead followed by 4 mm plastic scintillator. The ECAL has a depth of 25 X_0 (where X_0 = 1.6 is the radiation length). The ECAL is segmented in the plane transverse to the beam direction. In order to minimise the number of channels and because the hit density decreases as the distance from the beam line increases, the granularity is variable. The detector is divided into three sections with the section closest to the beam having the finest granularity and the section furthest from the beam having the coarsest.

In order to suppress the large charged pion background to the electron signal and to improve electron photon separation a scintillator pad detector (SPD)/preshower (PS) is included before the ECAL. This consists of a 15 mm thick layer of SPD scintillator and 15 mm of PS scintillator separated by 12 mm of lead. The granularity in the transverse plane matches that of the ECAL. The PS provides information which can be used to distinguish electrons and pions. An electromagnetic shower due to an electron will begin to develop in the preshower detector whereas only a very small fraction of the

Figure 2-10: Schematic drawing showing the layout of the SPD, PS and ECAL. Electrons first produce a signal in the SPD, the photon shower begins in the lead converter, whereas the pion shower doesn't begin until the pion enters the ECAL.

pions will interact. The SPD allows better separation of electrons and photons as the charged electrons will produce a signal in the SPD but photons will not. A schematic of the SPD, PS and ECAL is shown in Figure 2-10.

The HCAL is a sampling calorimeter made up of alternating layers of iron and scintillator. The total depth of the HCAL is 7.3 λ_I, where λ_I is the nuclear interaction length. The transverse granularity of the detector is coarser than the ECAL granularity with one HCAL component for every four ECAL components.

A single wavelength shifting fibre is coupled to each scintillator pad in the SPD/PS detector. Each fibre is then read out by a single channel of a 64 anode Multi-anode photomultiplier tube. Wavelength shifting fibres are also used in the ECAL and HCAL. In this case however the bunch of fibres coming from one module are read out using a single photomultipler tube.

2.2.5 The muon system

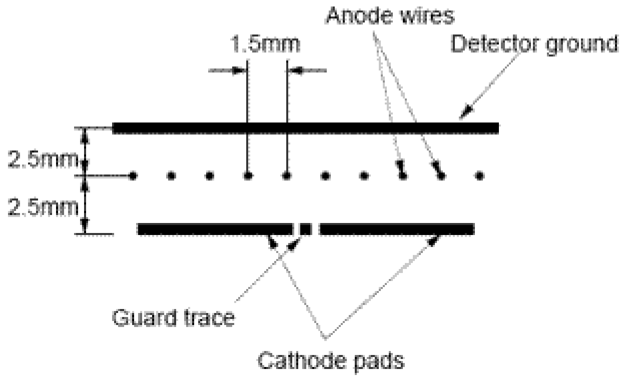

Figure 2-11: Schematic of a MWPC sensitive gap used in the LHCb muon system.

The muon detector is made up of 5 detector planes (M1-M5) and three layers of steel. M1 is located in front of the preshower detector. After the HCAL are four more muon detector planes M2-M5 separated by three 80 cm thick iron muon shields. The total absorber-thickness from M1 to M5 is 20 λ_I and in order to penetrate the detector and reach muon station M5 a muon must have a minimum energy of 6 GeV.

Multi-wire proportional chambers have been chosen as the detector technology for the muon system. A schematic of the sensitive gap used in these detectors is shown in Figure 2-11. The cathode pads are grounded and the anode wires are kept at a positive potential. The gap is filled with a gas mixture of $Ar/CO_2/CF_4$ in the proportions 40:50:10. As charged particles pass through the chamber they ionize the gas. Electrons are accelerated by the electric field towards the anode wires. As the electrons gain energy they cause more ionization in the gas thus multiplying the signal

Figure 2-12: Track finding by the muon trigger. For each hit in M3, hits are sought in the highlighted fields of interest in M2, M4 and M5. An extrapolation is made to M1 from the hits in M2 and M3. The closest M1 hit to the extrapolated line is chosen. Using the hits in M1 and M2 p_T is calculated assuming the particle originated at the interaction point and underwent a single kick from the magnet.

measured on the anode wire. M1 contains two of these sensitive gaps while M2-M5 contain four.

The muon system is used both in the Level-0 trigger to identify high p_T muons and to reconstruct muons in offline analysis. In order to pass the Level-0 trigger, muons must pass through all 5 muon detector planes. A line is projected from all hits in M3 to the interaction point. Hits are then sought in fields of interest around this line in planes M2, M4 and M5. When hits have been found in these four planes an extrapolation is made to M1 using the hits in M2 and M3. The hit closest to the extrapolated point is chosen as the M1 hit. The p_T of the muon is calculated using the hits in M1 and M2, assuming that the particle has come from the interaction point and has undergone a kick from the magnet. This procedure is illustrated in Figure 2-12.

2.2.6 The LHCb trigger

The presence of secondary vertices and particles with high p_T distinguish events containing a B-hadron from the large inelastic pp background. In order to isolate the interesting events three trigger levels are used to filter the data. These are referred to as Level-0, Level-1 and the High Level Trigger (HLT).

At Level-0 data from the calorimeters and muon system are used to select events containing high transverse momentum (p_T) electrons, photons, hadrons and muons. Such signatures are characteristic of the decay of heavy hadrons. Events found by the pile-up veto to contain multiple pp interactions are also rejected at this stage. This trigger must operate at the bunch crossing frequency of 40 MHz. The trigger latency is ~4 μs which includes the algorithm execution time and the time for the transfer of the decision to the front-end electronics. Data must be stored for the duration of the trigger latency in pipelines on board the Level-0 electronics. The data rate is reduced by a factor of 40 at this stage.

At Level-1 the primary vertex is found using information from the VELO. VELO tracks that have an impact parameter in the range 0.15 to 3 mm are then reconstructed and matched to candidate particles with high p_T that were selected at Level-0. The reconstructed VELO tracks are also combined with hits in the TT. The momentum of the track is determined by fitting the slope of the track at the VELO and at the TT, taking account of the integral of magnetic field in this region. Events are selected which have a minimum number of tracks passing certain p_T and impact parameter criteria. In addition, events with high mass di-muons are also retained. This trigger operates at the Level-0 accept rate of ~1 MHz. The latency of this trigger has an average value of 120 μs and data are stored in buffers in the Level-1 electronics for this time. This stage results in a further suppression of the data by a factor of 25.

The HLT uses the full tracking information to reject as quickly as possible events that do not contain interesting B-decays. The HLT is executed on a farm of processors. The algorithms that are executed will firstly confirm the measurements made at Level-1 with better resolution and secondly make a selection of events that contain the final states of particular B-decay modes. The output of the HLT after these algorithms will be of the order of a few hundred Hz. In addition, certain high rate calibration channels, such as events containing J/Ψs and D^*s will be selected. The total output rate will be approximately 2 kHz.

2.3 The RICH system

In order to achieve the physics goal of measuring CP asymmetries precisely, LHCb must be able to identify pions and kaons over a large momentum range. Without this ability it would be impossible to make meaningful measurements in a variety of B-decay channels. An example of this is seen in the decay $B_d \to K^+K^-$ which is studied in Chapter 5. In order to make a measurement of the CP asymmetry in this decay the signal must first be extracted from other two-body backgrounds that have the same event topology but contain pions and protons in the final state. Figure 2-13 shows how the signal from $B_d \to K^+K^-$ is swamped by these backgrounds if there are no RICH detectors to provide charged hadron identification and the improved situation where this identification is provided by the RICH system. The LHCb RICH system allows this signal to be extracted from the background and is also essential in the extraction of many other decays of interest in the B-meson systems.

Figure 2-13: The left hand figure shows how the two-body backgrounds swamp the $B_d \to K^+K^-$ signal without the particle identification of the RICH system. The right hand figure shows the improved situation where particle identification from the RICH system is available. Note the change in colour of the signal peak from black to white between the two plots.

In addition the RICH system is also used to identify the initial flavour of the signal hadron by considering the decay of the non-signal hadron in the event, a process known as flavour tagging. The charge of kaons in the final states of the decay of the non-signal B-hadron is used to identify the initial flavour of the signal hadron. When the quark decays $\mathrm{b} \rightarrow \mathrm{c} \rightarrow \mathrm{s}$ the charge of the kaon in the final state is the same as that of the decaying B-hadron. The RICH system plays an important role in the identification of these kaons.

2.3.1 Cherenkov Radiation

A particle travelling through a medium will emit Cherenkov radiation if its velocity is greater than the velocity of light in that medium. Cherenkov radiation is emitted in a cone around the particle's trajectory at a characteristic angle, θ_C, defined by the following relation:

$$\cos\theta_{\mathrm{C}} = \frac{1}{\mathrm{n}\beta} = \frac{1}{\mathrm{n}}\sqrt{1+\left(\frac{\mathrm{m}}{\mathrm{p}}\right)^2}, \qquad 2.2$$

where n is the refractive index of the medium, β=v/c, m is the particle's mass, p its momentum and the units assume c=1.

The number of photons emitted in a radiator is given by the following relation:

$$N_p = 2\pi\alpha L z^2 \int \frac{1}{\lambda^2}\left[1 - \frac{1}{(\beta n(\lambda))^2}\right] d\lambda \qquad 2.3$$

[eid04] where α is the fine-structure constant, L is the radiator length in cm, z is the charge of the particle in units of e and λ is the wavelength of the emitted photon. The distribution of photons in the azimuthal angle ϕ is flat.

Both equation 2.2 and 2.3 can be used to give information on m/p. As the momentum of a particle is known from the measurement made by the tracking system, the particle's mass can be determined and the particle is thus identified. For a more detailed discussion of Cherenkov radiation see [jac75]

2.3.2 The RICH detectors

The Cherenkov radiation phenomenon is exploited in the RICH detectors in order to perform particle identification. Both detectors measure the angle, θ_C, at which Cherenkov photons have been emitted. This is done by reflecting the photons using a series of mirrors onto a plane of photodetectors that are positioned outside of the detector acceptance. At the photodetector plane rings of photons are detected, the radius of which are directly related to θ_C.

Schematic drawings of the two LHCb RICH detectors are shown in Figure 2-14. These two detectors provide particle identification over the momentum range 1-150 GeV/c.

Figure 2-14: Schematic drawings of the two RICH detectors. RICH1 is shown in the transverse plane and RICH2 is shown from above.

RICH 1 is located immediately after the vertex detector and has an angular acceptance of 25-300 mrad. The location of RICH1 close to the dipole magnet puts it in a 60 mT magnetic field. The photon detectors must be shielded from this field in order to operate correctly. The iron shielding house shown in red in Figure 2-14 attenuates the magnetic field by a factor of ~25. Two radiators are used in RICH 1: The first is an aerogel radiator of thickness 5 cm and refractive index $n = 1.03$ which provides π-K separation in the low momentum range 2-10 GeV/c. The second is a gas radiator, C_4F_{10}, of extent 85 cm. This gas has a refractive index of $n = 1.0014$ and allows 3σ separation of pions and kaons up to 50 GeV/c.

RICH 2 is located after the tracking stations and has a reduced acceptance of 120 mrad (horizontal) × 100 mrad (vertical), with an inner acceptance on 10 mrad. This detector contains only one radiator, the gas CF_4. The radiator has an extent of 200 cm and a refractive index of *n* = 1.0005. RICH 2 provides π-K separation up to and beyond 100 GeV/c. The principal characteristics of the three radiators are given in the upper part of Table 2.1. These numbers include the Cherenkov angles and threshold momenta for β=1 pions and kaons.

Material	CF_4	C_4F_{10}	Aerogel
L (cm)	200	85	5
n	1.0005	1.0014	1.03
$\theta_C^{\max}$ (mrad)	32	53	242
$p_{thresh}(\pi)$ (GeV)	4.4	2.6	0.6
$p_{thresh}(K)$ (GeV)	15.6	9.3	2.0
$\sigma_\theta^{emission}$ (mrad)	0.31	0.69	0.29
$\sigma_\theta^{chromatic}$ (mrad)	0.42	0.81	1.61
σ_θ^{pixel} (mrad)	0.18	0.62	0.62
σ_θ^{track} (mrad)	0.20	0.40	0.52
σ_θ^{total} (mrad)	0.58	1.27	1.89
N_{pe}	23.2	30.3	6.8

Table 2.1: Some characteristics of the 3 radiators used in the RICH detectors. Values have been obtained from simulation. The lower part of the table lists the contributions to the single photon resolution (emission-point, chromatic, pixel and tracking), the total resolution per photoelectron and the number of detected photoelectrons in the ring [lhcb03].

2.3.3 Mirrors

RICH 1 and RICH 2 use both spherical and flat mirrors to reflect the Cherenkov photons onto the photodetector planes. The spherical mirrors focus the photons and the flat mirros reflect the image onto the detector plane outside the spectrometer acceptance. The RICH 1 spherical mirrors are made up of 4 quadrants, each 820 mm × 600 mm. Each mirror can be individually adjusted to ensure that they all share the same centre of curvature. These mirrors are made from 3 mm thick beryllium with a 0.3 mm glass skin on which aluminium is deposited The RICH 2 spherical mirrors are each

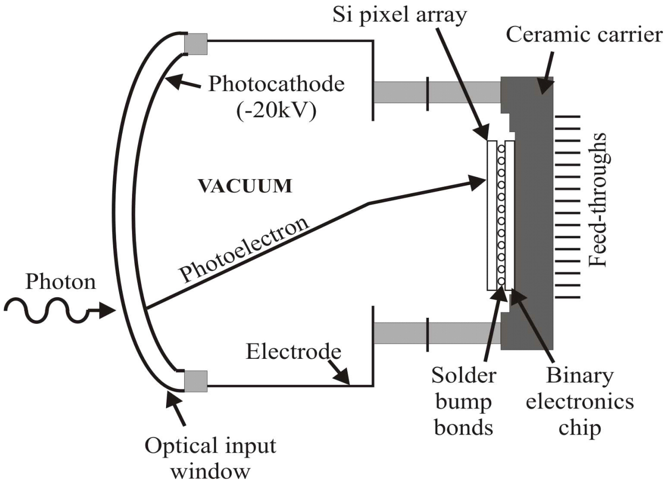

Figure 2-15: Schematic drawing of the Hybrid Photon Detector. Photons enter through a quartz window and are converted to photoelectrons at the photocathode. Photoelectrons are accelerated by a potential and cross focussed onto an anode. The anode consists of a silicon pixel array bump-bonded to a binary electronics chip.

made up of 21 hexagonal segments and 7 half hexagonal segments. The RICH 1 and RICH 2 flat mirrors are made from segments: 8 segments measuring 370 × 387 mm^2 and 20 segments measuring 410 × 380 mm^2 respectively. The RICH 2 spherical mirrors and all flat mirrors are made from 6 mm glass coated with aluminium. All mirrors are also coated with a protective layer which is designed to optimize the reflectivity for the wavelengths that the photodetectors have the largest quantum efficiency. The mirror alignment will need to be better than0.1 mrad in RICH2 in order to preserve good resolution on the Cherenkov angle. Data and a laser alignment system will be used to achieve this as described in [pap00].

2.3.4 Photon Detectors

The photon detectors used in the RICHes must detect single photons over a total area of $2.9m^2$. This will be done by a fine pixel matrix with effective granularity 2.5×2.5 mm^2. The pixel granularity is chosen by comparing the size of the contribution to the Cherenkov angle resolution of the pixel with the other contributing factors that are

Figure 2-16: The measured quantum efficiency of an HPD photocathode. Measurement courtesy of DEP.

summarised in Table 2.1. A finer pixel matrix would add additional cost without any significant improvement in performance. The detectors must have high quantum efficiency in order to maximise the number of detected photons, particularly in the visible region where unscattered aerogel photons exist. The photon detector readout must also be compatible with the LHC bunch crossing interval of 25 ns. The detectors are required to survive for 10 years in a radiation environment with doses of up to 3kRad/year and be able to operate in a magnetic field of up to 3 mT [lhcb03].

The detectors chosen to satisfy these requirements are Hybrid Photon Detectors (HPDs). A schematic of the HPD device being developed for LHCb in collaboration with industry[2] is shown in Figure 2-15. A photocathode is deposited on the inside of the 7 mm thick quartz entrance window. The photocathode used is a multi-alkali S20-type which has typical peak quantum efficiencies of 25% at wavelengths of 250 nm. The measured quantum efficiency against wavelength of one of these photocathodes is shown in Figure 2-16. A calibrated light source is used along with a set of calibrated filters to calculate how many Watts of light reach the HPD. The current drawn by the photocathode at each point is also recorded leading to a measurement of the Raidiant Sensitivity (mA/W). This can be converted to a quantum efficiency using the following relation:

$$R = 10 \times QE \times e \times \frac{\lambda}{hc} \qquad 2.4$$

where R is the Radiant Sensitivity, QE is the Quantum Efficiency, λ is the wavelength, e is the charge on an electron, h is Planck's constant and c is the speed of light.

The dip in efficiency at ~ 300 nm can be explained by considering the process by which incoming photons are converted to photoelectrons at the photocathode. An electron, excited by an incoming photon, has an energy equal to that of the photon, minus the band gap energy of the photocathode. This electron will loose energy through interactions in the photocathode and has a probability of escaping the vacuum if it retains enough energy to overcome the potential barrier. If the incoming photon has energy at least twice the band gap energy of the photocathode, the photon may excite a secondary photoelectron. These photoelectrons will consequently have less energy and therefore less chance of overcoming the potential barrier and escaping from the photocathode. It is this effect that causes the dip in quantum efficiency.

Emitted photoelectrons are accelerated by a potential of ~ 20 kV and cross-focused with a demagnification factor of ~ 5 onto the anode. The anode consists of a silicon pixel detector bump bonded to a binary readout electronics chip. When a photoelectron strikes the reverse-biased silicon ~ 5000 electron-hole pairs are produced. The charge is collected on a 32 × 32 array of pixels of dimensions 500 × 500 μm^2. The

---

[2] Delft Electronic Products B.V., Netherlands

Figure 2-17: Diagram showing μ-metal shield
around a single HPD

signal in each pixel is amplified, shaped and compared with a discriminating threshold by the readout chip.

The photon detectors are shielded within each of the RICH vessels from the stray magnetic field due to the dipole magnet. However there will be some residual field of up to 3 mT from which the photon detectors must be shielded. This is done by surrounding each HPD with a 0.9 mm thick μ-metal shield as shown in Figure 2-17. A prototype HPD has been tested in a μ-metal shield in fields of up to 5 mT. Figure 2-18 shows how the image of a cross on the photocathode is distorted by the presence of a magnetic field. In both cases the black dots show the shape of the undistorted image. In the case of a 3 mT axial field the image of the cross remains on the silicon sensor and the maximum displacement is 0.6 of a pixel in a 3 mT transverse field. In order to correct for these distortions a similar test must be performed when the detector is in place. The distortion of the image can be parameterised and a mapping can be defined which must be applied to all pixel hit data.

Figure 2-18: The image distortions due to a magnetic field. The black dots show the undistorted image. Green dots show image distortion due to 3 mT transverse field (left) and blue dots show image distortion due to 3 mT axial field (right).

2.3.5 Readout electronics

The readout electronics scheme for the RICH is shown in Figure 2-19. The HPD readout chip forms the first stage of the RICH readout. From there data are sent into the on-detector Level-0 electronics. The Level-0 electronics board takes data from the readout chips, multiplexes them and drives optical links over which the data are sent to the Level-1 electronics. The board also distributes control signals such as the global clock and the trigger signals to the pixel chips. Each Level-0 board processes the data from 2 HPDs. The HPD readout chip as well as components of the Level-0 electronics are discussed further in Chapter 3.

Figure 2-19: Schematic of the RICH readout architecture

The Level-1 electronics receives the Level-1 trigger decision and reduces the data further. The data are zero-suppressed and further multiplexed at this stage and sent on to the event building data acquisition (DAQ) network.

2.3.6 Cherenkov Angle Reconstruction and PID Performance

A Cherenkov angle is calculated for each hit pixel, assuming a parent track. Photoelectrons lying on the same ring will have the same value of Cherenkov angle, within the resolution of the measurement. The Cherenkov angle is calculated for each photon taking into account the geometry of the spherical mirror, the assumed emission point, the parent particle trajectory and the location of the hit pixel. This calculation is discussed in further detail in Chapter 4.

Equation 2.2 shows that the number of photoelectrons emitted in the radiator is dependent on the refractive index and length of the radiator. The number of photoelectrons expected to be produced in each of the three radiators is given in Table 2.1. Photons are known to undergo Rayleigh scattering in aerogel, which is described in more detail in Appendix A. This scattering results in a lower number of photons on each aerogel ring and is a source of background photons that must be considered. In order to reduce the number of Rayleigh scattered aerogel photons reaching the photodetector plane a 100 μm thick glass filter is placed after the aerogel which will absorb photons with a wavelength below 350 nm.

Resolution

The following factors contribute to the resolution obtained on a measurement of the Cherenkov angle for a single photoelectron.

- Emission point: the spherical mirror is tilted in order to bring the image out of the detector acceptance. Due to this tilt the focusing is not perfect and the photon hit point on the detector plane is dependent on the point on the track at which the photon was emitted. Reconstructed Cherenkov angles are smeared as the assumption is made that all photons are emitted at the mid-point of the track in the radiator.

- Chromatic: the refractive index of the radiator, and therefore the Cherenkov angle, is wavelength dependent.

- Pixel: an error on the detection point of the photon is introduced due to the granularity of the HPD anode.

- Track: errors in the reconstruction of the track direction.

For a perfectly aligned detector the emission point, chromatic and pixel error are uncorrelated. This leads to a total error on the measurement of the Cherenkov angle:

$$\sigma_\theta^{\text{total}} = \frac{\sigma_\theta^{\text{single}}}{\sqrt{\text{N}}} + \sigma_\theta^{\text{track}} \qquad 2.5$$

where $\sigma_\theta^{\text{single}}$ is the error on the Cherenkov angle for a single photon, N is the number of photons in the ring and $\sigma_\theta^{\text{track}}$ is the error on the reconstruction of the track direction. The size of each component of the error is given in Table 2.1 along with the total error on the Cherenkov angle for each of the three radiators. It is the chromatic error that gives the largest contribution to the total error in both RICH1 and RICH2.

Pattern Recognition

The high multiplicity of particles produced in proton-proton interactions at the LHC means that many rings will be imaged on the photodetector plane. Identifying which ring goes with which track will not be straightforward and some rings, for example aerogel rings made up of few photons, will be difficult to pick out. In order to facilitate this task pattern recognition algorithms have been developed.

The pattern recognition associates a particle type with each track in an event based on the position of the photon hits. A global likelihood fit is made which uses tracking information and the information from the three RICH radiators simultaneously. A comparison is made between the expected number and position of photons for a given particle type and the detected photons. The expected distribution of photons is calculated on the assumption that the track has one of the following particle types; electron, muon, pion, kaon and proton. The expected distribution is compared with the observed distribution in a log-likelihood function. The particle is identified as the assignment for which the log-likelihood function is maximal. Figure 2-20 shows rings identified by the pattern recognition in the photon detector planes of both RICH detectors [for98].

2.4 Expected RICH Particle Identification Performance

As explained in the previous section a likelihood is obtained for each mass

Figure 2-20: Pattern recognition applied to an event in RICH1 (left) and RICH2 (right). Reconstructed Cherenkov rings are superimposed.

hypothesis for every reconstructed track. The difference in log-likelihood of two hypotheses can be converted into a significance of separation in number of sigma. The difference in the case of the pion and kaon hypotheses is given by:

$$\Delta \ln L_{K\pi} = \ln L(K) - \ln L(\pi) \qquad 2.6$$

By assuming that for a large number of experimental observations the likelihood tends to be Gaussian distributed, for example

$$\mathcal{L}_{\pi} \approx \frac{1}{\sqrt{2\pi}\sigma} e^{\frac{1}{2}\frac{x_{\pi}^{2}}{\sigma^{2}}} . \qquad 2.7$$

Therefore the difference in log likelihood can be translated into a significance of π-K separation:

Figure 2-21: Significance of π-K separation in number of sigma as a function of momentum. Calculated for true pions in a sample of $B^0 \rightarrow \pi^+\pi^-$ events. The superimposed line shows the average separation.

$$N_{\sigma} = \sqrt{2\left|\Delta \ln L\right|}\,. \qquad 2.8$$

The distribution of this significance as a function of momentum is shown in Figure 2-21. The figure illustrates that good π-K separation is achieved over most of the momentum range, 2 – 100 GeV/c particularly for intermediate momenta where the mean value N_{σ} exceeds 10.

The performance can also be studied by looking at the probability that a particle type is correctly, or incorrectly identified as a function of momentum. Figure 2-22 shows the efficiency of positively identifying a kaon as a heavy particle (kaon or proton) and the efficiency of misidentifying pions. The plot is made only considering particles which are above threshold. The effect of crossing the Cherenkov threshold for each of

Figure 2-22: Kaon identification efficiency is shown in red. Pion misidentification rate is shown in blue. The dips in the kaon efficiency occur when the Cherenkov thresholds in each of the three radiators are crossed

Figure 2-23: Tracking performance: (a) efficiency as a function of momentum; (b) ghost rate, as a function of the track momentum cut used.

the three radiators is seen as a reduction in kaon identification efficiency at p ~ 2, 9 and 16 GeV/c.

2.5 Detector Simulation and Event Reconstruction

Results presented in chapter 5 on the potential for observing $\mathrm{B_d} \rightarrow \mathrm{K^+K^-}$ and $\mathrm{B_s} \rightarrow \pi^+\pi^-$ are obtained using the LHCb detector simulation and reconstruction programs described here. Firstly, proton-proton interactions at a centre-of-mass energy of 14 TeV are simulated using the PYTHIA 6.2 [sjos01] event generator. The main processes for b production are flavour excitation, pair creation and gluon splitting. The large data sets that are produced are filtered to provide data sets containing at least one b or $\overline{\mathrm{b}}$ hadron.

The particles are then tracked through the detector using a GEANT4 [all03] detector description. The LHCb detector is described in detail including active detector components, front-end electronics and passive components such as the beam-pipe, supports and shielding elements. The information provided by GEANT4 is used to produce digitised "raw-data" that mimic the detector output. At this stage the sensitivity and response of each detector is considered. Other effects such as electronics noise, cross talk and spill-over events from previous bunch crossings are also included.

Using the simulated detector signals as input, tracks are reconstructed using registered hits in the VELO, the TT and T1-T3. Initially candidate tracks are searched for in the VELO and T1-T3. Once candidate tracks have been found searches are made in remaining tracking stations within a region of interest around the candidate track. Tracks are finally fitted taking into account multiple scattering in inactive detector elements and dE/dx energy loss. After tracks have been found RICH, muon and electron particle identification is carried out.

2.6 Detector Performance

The detector performance can be assessed in terms of the tracking efficiencies, vertex resolutions and particle identification performance.

Figure 2-23 shows the tracking efficiency as a function of momentum. For tracks with momentum greater than 10 GeV/c the average efficiency is 94%. The corresponding rate for finding “ghost” tracks that are not due to a true simulated particle is also shown in the figure. The average value is approximately 3.5% with the situation at low momentum being worse. The momentum and impact parameter resolution for reconstructed tracks are shown in Figure 2-24. This is seen to rise from $\delta p/p = 0.35\%$ for low momentum to a value of $\delta p/p = 0.55\%$ at the higher end of the spectrum. This can be compared with the momentum distribution of B-decay particles that is also shown in the figure. The impact parameter resolution shown in the same figure as a function of $1/p_T$, can be parameterised by 14 μm + 35 μm/p_T, where p_T is in GeV/c. Again the $1/p_T$ spectrum is also plotted in the figure for comparison.

Figure 2-24: (a) momentum resolution as a function of track momentum; (b) impact parameter resolution as a function of $1/p_T$. The p and $1/p_T$ spectra are shown for comparison in the lower parts of the plots.

Figure 2-25: Muon identification efficiency as a function of momentum along with corresponding pion misidentification rate with scale on right of plot.

Muons are identified by taking tracks with $p > 3$ GeV and extrapolating to the muon stations. Hits are searched for within regions of interest around the track direction. The muon efficiency as a function of momentum which is close to 100 % across the full momentum range is shown in Figure 2-25, along with the corresponding pion misidentification rate which is around 3%. By combining information from the muon system, the calorimeters and the RICH muon identification performance can be improved still further. The likelihoods as determined from each of the subdetectors are combined as follows:

$$L(\mu) = L_{RICH}(\mu)L_{CALO}(\text{non e})L_{MUON}(\mu) \tag{2.9}$$

Figure 2-26: Difference in log likelihood between pion and muon hypothesis for true (a) muons and (b) pions.

where $L_{RICH}(\mu)$ is the muon likelihood found using the RICH system, L_{CALO}(non e) is the likelihood that the particle is not an electron, found using the calorimeter and $L_{MUON}(\mu)$ is the muon likelihood found using the muon system.

The difference in log likelihood between the muon and pion hypothesis for true pions and true muons from a sample of $B^0 \to J/\psi(\to \mu\mu)K_s^0$ is shown in Figure 2-26. By requiring the difference in log likelihood to be greater than −8 the pion misidentification rate reduces to 1% while the muon identification efficiency remains at 93%.

ECAL and preshower information are used to construct the likelihood that a particle is an electron. This can then be combined with likelihoods from the RICH and muon systems:

$$L(e) = L_{RICH}(e)L_{CALO}(e)L_{MUON}(\text{non } \mu) \tag{2.10}$$

where the definition of each term is self-evident.

This technique leads to average efficiency for electrons coming from $B^0 \to J/\psi(\to ee)K_s^0$ decays, of 95% with a pion misidentification rate of 0.7%. This can be seen in Figure 2-27.

As mentioned in 2.2.2 the primary vertex resolution achieved is 42 μm in the z direction and 10 μm in the x and y directions. Results showing the secondary vertex

Figure 2-27: Electron identification efficiency as a function of momentum after combination of likelihoods. The corresponding pion misidentification rate is also shown with scale on right.

reconstruction will be given in Chapter 5.

2.7 Summary

The LHCb detector will make detailed measurements of CP parameters in the B sector. It has been designed to make use of the large number of $b\bar{b}$ pairs that will be produced at the LHC. The detector provides excellent vertex, proper lifetime and momentum resolution. The RICH system provides the required particle identification performance and the trigger is optimised to select the B-decays of interest.

The photodetectors used in the RICHes are central to the particle identification performance. The development of prototype HPDs that meet the LHCb requirements is discussed in Chapter 3 and their performance in testbeam conditions is assessed in Chapter 4. In Chapter 5 the sensitivity of the detector to the rare charmless decays $B_d \to K^+K^-$ and $B_s \to \pi^+\pi^-$ is assessed.

Chapter 3

The development of a prototype HPD with 40 MHz readout

3.1 Introduction

The Hybrid Photon Detector (HPD) is being developed at CERN in collaboration with industry as the photon detector for the LHCb RICH project. In this chapter, the production and evaluation of anodes for the first HPD prototypes operating at 40 MHz is described.

The readout electronics for the RICH detectors were described briefly in Section 2.3.5. In this chapter the Level-0 RICH electronics is considered in more detail. In particular, the performance of the Analogue Pilot chip, which provides reference voltages to the HPD pixel chip, is studied.

3.2 HPD anode overview

3.2.1 Introduction

A description of the HPD device was given in section 2.3.4. HPD prototypes have been made in the past with the same electron optics, however the anodes used were not suitable for LHCb purposes [gys00]. In this chapter the anode designed for use in LHCb is described in greater detail and an account is given of the stages in the production of the first prototypes using this anode.

3.2.2 Silicon Detector

The silicon detector is manufactured in industry[1]. The side of the detector on which the photoelectrons are incident, known as the back side, is formed by a thin 150 nm n+ implant. The thickness of the n+ implant is designed to minimize the energy lost by incoming photoelectrons and thus maximize the number of electron hole pairs created in the bulk. Charge is collected on p+ implants segmented into an array of 256×32 pixels measuring 500 × 62.5 μm^2. The detector design includes a guard ring surrounding the pixel matrix that will sink any excessive leakage currents. A ring of aluminium is applied to the back side of the detector through which a reverse-bias of ~ 80 V applied. This voltage generates a high electric field which facilitates charge collection. A cross section schematic of the detector is shown in Figure 3-1.

Figure 3-1: Cross section of silicon detector. The back side of the detector is a thin n+ layer minimising the energy lost by the photoelectron before it passes into the bulk. p+ implants form the pixel matrix which is surrounded by a guard ring (orange). Reverse bias is applied to the detector via the aluminium ring.

---

[1] Canberra Semiconductors N. V. Belgium

Figure 3-2: Schematic showing 4 super-pixels, indicating their dimension and sub-division. 8 sub-pixels (blue) make up one super-pixel (black)

3.2.3 Readout chip

A brief description of the chip and its operation are given below. A more detailed description can be found in [wyl01].

The readout chip, termed LHCBPIX1, has pixels which match those on the sensor in number and dimension. Each readout chip pixel is bonded to a pixel on the silicon detector. It is possible to read out each of the 8192 channels (sub-pixels) individually (ALICE mode), and also to form an OR of the outputs of 8 sub-pixels grouped vertically, thus reading out 'super-pixels' (LHCb mode). Figure 3-2 shows the pixel dimensions and the arrangement into sub- and super-pixels. The two mode names, ALICE and LHCb, originate from the fact that the design of this readout chip is the outcome of a joint CERN project whose aim was to design a chip that could be used for both the LHCb HPDs and for the ALICE silicon pixel detector [cho03]. ALICE require that all 8192 channels are read out, although at a reduced frequency of 10 MHz. The chip design eventually diverged and the final ALICE and LHCb chips are not identical. However the mode name remains to describe the case where all channels are read out. ALICE mode will be used in LHCb for testing and calibration purposes. In LHCb mode, the operation intended for normal LHCb data-taking, super-pixels will

Figure 3-3: Schematic of a pixel cell

be read out. In this case there is an effective pixel array of 32×32, each pixel having dimensions 500×500 μm.

Figure 3-3 shows a schematic of the electronics that read out a single pixel cell. Each cell is divided into an analogue and a digital part. The signal is amplified, shaped and compared with a threshold setting in the analogue part of the chip. If the signal is above threshold a 1 is output by the digital part of the chip. In the digital part of the chip the signal is synchronised to the clock, delayed and stored for the duration of the trigger latency (4 μs). It is possible to give a test input to the chip by applying a voltage step across a capacitor (C_test in Figure 3-3).

3.3 Anode production and testing

3.3.1 Overview of HPD production chain

Figure 3-4 shows the first stage in the HPD production chain. This step involves the production and packaging of the anode which consists of the silicon detector bump-bonded to the readout chip. Readout and detector chips are both produced on silicon wafers, each of which contains many identical chips; these wafers are diced and bump-bonded in industry[2]. Bump-bonding is the name given to the technique used to attach the detector and readout chips. A solder bump is deposited on each pixel of the readout chip. The detector and readout chips are then aligned and attached so that each pixel on the sensor chip has an individual bond to the equivalent pixel on the readout chip. The bump-bonded assemblies are then packaged in ceramic carriers[3]. Before the packaging can take place the contacts on the carrier are gold-plated to prepare for the wire bonds that will be attached between the carrier and the chips and a Kovar ring is brazed to the carrier. This ring will later form the seal between the anode and the rest of the HPD tube body. Kovar is an alloy of cobalt, nickel and iron, chosen as it has the same thermal coefficient of expansion as glass. This property is required as the tube undergoes some high temperature thermal cycles during production and an expansion of the seal between anode and tube body could compromise the vacuum seal.

Figure 3-4: Stages involved in anode production

---

[2] VTT Electronics, Finland

[3] Produced in industry by Kyocera Corporation, Japan

Figure 3-5: Stages involved in HPD assembly. Vacuum sealing stage involves a thermal cycle with maximum temperature 300°C.

Figure 3-5 shows the second stage in the process, which is also conducted by an industrial collaborator[4]. The anode is first sealed onto the tube body; then, in a vacuum, the photo-cathode is deposited on the inside of the quartz window. The quartz window is then attached to the rest of the tube body in order to form a vacuum tight seal. The tube is subjected to a thermal cycle designed to reduce the amount of out-gassing that will occur during the lifetime of the tube. The temperature is increased over 6 hours to 300°C and remains at this temperature for 3 hours; it is then decreased to room temperature over a further 6 hours.

Testing is carried out at each stage of the production chain. This testing has two main aims: firstly, to select fully functional components, as only these should be sent through to subsequent stages of the production chain. Secondly, to identify stages where problems occur with the aim of avoiding these problems in the future.

Readout chips are first tested on the wafer in order to identify chips that perform to requirements. ALICE mode is used for testing so that the number of working sub-pixels can be established. The term 'pixel' is used in the remainder of the chapter to

---

[4] Delft Electronic Products B.V., Netherlands

refer to an ALICE pixel, or sub-pixel, unless stated otherwise. In order to maximise the proportion of good anodes only chips that pass these tests are used to bump-bond to detector chips. Detector chips cannot be tested before any readout electronics have been attached. However, some quality control is performed by the manufacturers and the yield for detector wafers is ~90%.

After bump-bonding the readout chip is tested again to ensure there has been no deterioration in performance as a result of the bump-bonding procedure. It is also possible to test the detector performance for the first time. Defects in the bump-bonding and excessive detector leakage currents can be identified at this stage.

Bare assemblies are then packaged in ceramic carriers. Tests are performed again after this procedure to ensure readout chip, detector performance and bump-bond quality have not degraded.

Finally, after the tube has been assembled, a full range of tests can be carried out to assess its performance. These include laboratory tests using a pulsed laser light source, and beam tests where Cherenkov photons are detected. The results from the beam tests are presented in Chapter 4.

3.3.2 Operating the readout chip

Configuring the readout chip

Bias voltages and currents must be provided to the circuitry within the pixel cells. These biases provide references to the pixel circuitry and define the amount of current flowing in components. The bias settings must therefore be set to the correct values in order that the chip operates correctly. An example is the value of the global threshold discussed in section 3.2.3. This threshold is defined by the value of one of the bias voltages, known as 'pre_VTH'. In total there are 42 biases that must be provided and this is done by 42 DACs (Digital-to-Analogue Converters) on board the chip.

It is possible to set each of these DACs with a digital value using a JTAG[5](Joint Test Action Group) interface. JTAG is a standard that specifies how to control and monitor the pins of a device. In order for the DACs to make a meaningful conversion from a digital code to an analogue value they require a reference voltage. Two external references are used to generate reference voltages for the pixel chip DACs. These two references are referred to as 'DAC_REF_VDD' and 'DAC_REF_MID'. A further two external references are used as thresholds which set the transition levels of the input signals. These transition level references are referred to as 'GTL_REF' and 'GTL_REFa'.

As explained in section 3.2.3 it is possible to provide the chip with a test input that comes from the discharge of an internal capacitor. The magnitude of this test pulse is set by two external reference voltages, 'analogue_test_hi' and 'analogue_test_lo'. A voltage step is generated in the chip by switching between these two levels and it is applied to the pre-amplifier input through a charge injection capacitor.

In addition there are five latches inside the pixel cell which provide additional functionality. One bit allows a pixel to be masked and unmasked. As mentioned above a global chip threshold is set for the chip by the pre_VTH DAC. Three bits in the pixel cell provide fine adjustment to the global threshold pixel-by-pixel. Finally, a fifth bit turns a pixel on or off to a test input.

In summary, the following must be provided:-

---

[5] IEEE Std 1149.1

- Digital values of 42 pixel chip DACs (including pre_VTH);
- Four reference voltages, DAC_REF_VDD, DAC_REF_MID, GLT_REF and GTL_REFa.

Optionally the following may be set for each pixel:-

- Pixel masked/unmasked;
- Fine adjustment of threshold setting.

When using the test pulse input the following must be set:-

- Reference voltages that set the magnitude of the test pulse, analogue_test_hi and analogue_test_lo;
- Pixel on/off to test input.

Data Acquisition

Figure 3-6 shows some required signals and their timing for chip data acquisition. The reader should also refer to Figure 3-3 for the pixel cell readout schematic. A charge input to the chip results in an output from the pre-amplifier and shaping stages (pre-amp) that has a peaking time of 25 ns. This signal is then compared to the threshold by

Figure 3-6: Relative timing of signals involved in readout chip operation.

a discriminator. If the signal is above threshold, the discriminator output is then synchronised to the chip's clock (CLK). The synchroniser output then goes through a delay line, the length of which can be tuned. In order for the signal to be read out, a trigger signal referred to in the figure as 'Strobe', must arrive on the same clock edge as the delay line output and the delay length is tuned so that this is the case. If Strobe arrives the delay line output is shifted into the pixel FIFOs. 'FIFO' stands for first-in-first-out and is a storage device, where during LHCb operation hits are stored for the duration of the Level-0 trigger latency which is 4 μs. As the name suggests events stored in the FIFO are read out in the time order that they were stored, with the oldest event being read out first. In order that events are read from the FIFO two more external logic signals are required. Firstly, the arrival of the logic signal 'NEVR' (Next-Event-Read) triggers the transfer of events stored in the FIFO into shift registers. A second logic signal, 'CE' (Chip Enable), must then arrive to allow these shift registers to be read out.

As explained in section 3.2.3 a test pulse can be injected into the pixel front end via the discharge of the capacitor 'C_test'. The capacitor discharge is triggered by the positive edge of a logic signal called 'TEST_PULSE'.

3.3.3 Test system

A test system has been designed to provide all of the required signals to the chip and bias to the detector, and to perform data acquisition. A schematic diagram of the

Figure 3-7: Test system schematic showing the direction of control signals and data.

system that has been used to perform all tests discussed in this chapter is shown in Figure 3-7. The test system is controlled by a PC using the LabVIEW[6] program.

The motherboard generates the six external voltages discussed in section 3.3.2. The values of these biases are set using the LabVIEW interface which sends instructions via a JTAG controller. The chip parameters, such as the digital values of the 42 chip DACs, are also set in this way.

The chip clock is generated by a 40 MHz crystal oscillator on the transmitter board. This board accepts resets and triggers from external sources. Once a trigger is received a FPGA (Field Programmable Gate Array) generates the control signals STROBE, NEVR and CE.

Data from the chip are read via the motherboard and buffered on the transmitter board. They are then serialized and sent on a twisted pair data link to the FLIC (Flexible I/O Card).

---

[6] National Instruments Corporation

The FLIC is a PC interface which was developed at CERN as an alternative to VME-based DAQ systems. More detailed information on this device can be found in [gui02]. The FLIC has a large data buffer, programmable logic and also sends triggers to the transmitter board. The FLIC trigger rate can be controlled by the LabVIEW program or by some external trigger source.

3.3.4 Wafer probing

LHCBPIX1 chips are produced on silicon wafers 200 mm in diameter and 750 μm thick. These wafers, commonly known as '8-inch' wafers, contain 71 LHCBPIX1 chips. Figure 3-8 shows a map of a wafer indicating the number of each chip.

As discussed in section 3.3.1 the readout chips are first tested on the wafer to select chips that perform to requirements. A number of tests are carried out that determine the quality of the chip.

Chips are tested on the wafer at a probe station. The connection between the test system (Figure 3-7) and the chip is made via a probe card. The card routes the signals

Figure 3-8: Wafer Map showing the layout of 71 chips on a silicon wafer. Grid is overlaid the circular wafer

Figure 3-9: Close up of probe needles (left) and schematic of readout chip I/O pads (right). There are two rows of I/O pads at either side of the chip. The probe card needles are aligned with the inner rows.

to two rows of needles that are aligned with rows of I/O (Input/Output) pads on the chip. Figure 3-9 shows a close up of the probe needles and a schematic showing the positions of the I/O pads on the chip. There are 2 rows of I/O pads at the top and bottom of the chip. The inner pads are used for probing as the outer rows are reserved for wire bonding.

The probe card is mounted on the probe station and fixed in place. The wafer is placed on a movable chuck underneath the needles. This chuck is then manoeuvred until the needles are aligned with the I/O pads on the chip. Finally the chuck is raised up until the needles are in contact with the chip.

Firstly, the analogue and digital chip currents are measured. The expected value for the analogue and digital chip currents under normal operation conditions are ~ 300 mA and ~ 400 mA respectively. Very high or low currents are a good first indication that there is a problem with the operation of the chip.

The next test checks that the chip can be configured correctly by the JTAG system. Digital codes (0 and 255) are sent to each of the pixel chip DACs and to the pixel configuration bits. The set bits are then read back; if the code read back is identical with that sent, the test is passed. If there is a failure in the configuration of the DACs, the chip can be immediately rejected as the chip's bias voltages cannot be set correctly. A failure of the pixel configuration implies, for example, that a pixel is permanently masked. A chip that fails in this way may still function, albeit with some missing pixels, and should be tested further.

The definitive test of the chip's performance is a threshold scan. The global threshold on the chip is set by the value of pre_VTH, one of the readout chip DACs. The scan tests the uniformity of this threshold across the chip and gives a result for the number of working pixels in the chip. The scan is performed at the 'minimum threshold', which is defined to be the lowest value of the threshold with negligible noise. Noise in this case is a pixel firing when no test pulse is sent to it. The minimum threshold is found by first setting the global threshold to a low level, and then triggering and reading out the chip, without enabling the test-pulsing. At the starting threshold many noise hits are counted, so the threshold is raised step by step until fewer than 3 hits over the whole chip have been counted after each pixel has been read out 50 times. The pre_VTH DAC then remains set at this minimum threshold value for the duration of the threshold scan.

In a threshold scan a number of test pulses are sent to each row of the chip in turn. As described in section 3.2.3, the size of the test pulse given to the chip is set by the values of the two externally applied bias voltages analogue_test_hi and analogue_test_lo. The test pulse is set to a value well above threshold (~ 20mV) for the first step in the scan. For the subsequent step the size of the test pulse is reduced by increasing the value of analogue_test_lo in 1 mV steps while keeping analogue_test_hi fixed. Test pulses are again sent to each row in turn and this process continues until analogue_test_lo is equal to analogue_test_hi and a test pulse of zero magnitude has been sent. The pixel efficiency is calculated for each stage of the scan as follows,

$$\text{Efficiency} = \frac{\text{h}}{\text{t}} \qquad 3.1$$

where h is the number of pixel hits counted and t is the number of test pulses sent.

Figure 3-10 shows a typical 'S-Curve', a plot of efficiency against magnitude of test pulse for one pixel. An ideal device would have 100% efficiency for a test pulse above threshold and 0% efficiency for a test pulse below threshold. Noise and fluctuations in the signal result in an S-Curve rather than a step function. The threshold value is defined to be the voltage at which the pixel efficiency is 50 %, which is typically around 11 mV.

Figure 3-10: S-Curve measured for one pixel. Threshold value is defined at 50 % efficiency which here is ~11.5 mV.

Wafer Number	Class I	Class II	Class III
1	30	11	30
2	32	10	29
3	23	13	35
4	27	10	34
5	36	8	27
6	27	9	35
7	40	14	17
Total	**215**	**75**	**207**

Table 3.1: Summary of chip yields for 7 tested wafers

Assuming Gaussian noise, it is possible to make an estimate of the noise in each pixel. The difference between the test pulse magnitude at 98% efficiency and 2% efficiency is approximately 4 times the sigma of the noise distribution.

Threshold values cannot be calculated from S-Curves that do not pass through 50% efficiency. Pixels for which no threshold value can be calculated are classed as non-operational.

Chip Classification

Chips are put into one of three categories as a result of these tests. This categorization identifies the chips that can be used for bump-bonding to detector chips as Class I. The other categories identify chips that operate below specification and chips that do not work at all.

Chips are classified in terms of the number of operational channels:-

- **Class I**: > 99% pixels operational;
- **Class II**: 0 < operational pixels ≤ 99%;
- **Class III**: 0 pixels operational.

Class III chips may fail for any of the reasons below:-

- JTAG test failed;

- DAC scan failed;
- Analogue and/or digital current > 800mA;
- No digital output;
- No minimum threshold can be found.

Chip yield and results

A batch of 7 wafers was tested in order to select readout chips to be bump-bonded to silicon detectors. A summary of the yield is given in Table 3.1. It can be seen that the yield of Class I chips is 43%.

600 HPDs are required from the final production. It is foreseen that the chips for this production will be taken from 48 wafers. With the above yield ~ 1500 chips would be expected to pass the test, more than sufficient for 600 HPDs. Wafers are produced by industry in batches of 24 as standard. Although the yield seems good enough to reduce the production to 24 wafers, this leaves little contingency and the production size remains unchanged as a result of these pre-production tests.

Figure 3-11: Analogue and Digital currents measured for all chips on 7 wafers. Currents for Class I and II chips are indicated by the shaded area and for Class III chips by the dotted blue line

Figure 3-11 shows the distributions of analogue and digital currents for all chips from the seven wafers. The currents for the Class I and II chips are shown by the shaded histogram and the currents measured for the Class III chips are indicated by the blue dotted line. From these plots it can be seen that it would be reasonable to add a classification condition, accepting only chips with analogue currents of 300-600 mA and digital currents of 300-700 mA. During wafer testing for the HPD production, time would be saved as chips could be rejected immediately on the basis of the current values measured, without having to perform any of the more time consuming tests.

Figure 3-12 shows the distribution of thresholds and noise across the channels on a sample chip. The threshold and noise are calculated from the S-Curve for each pixel. The mean threshold is 10.6 mV with Gaussian width, $\sigma = 0.9$ mV and the mean noise is 1.4 mV with $\sigma = 0.1$ mV. LHCb specifications require a threshold < 2000 e^- with a spread of < 200 e^- [rich00] in order to accommodate signals with size 3000-5000 e^-. The capacitor which generates the test input has a capacitance of

Figure 3-12: Threshold and noise distributions across a chip. Mean threshold 10.6 mV (width of fitted Gaussian = 0.9 mV), mean noise 1.4 mV (width of fitted Gaussian = 0.1 mV)

Figure 3-13: Distribution of mean threshold and noise across the sample of 7 wafers. Mean of mean threshold distribution = 9.81 mV (width of fitted Gaussian = 0.49 mV), mean of mean noise = 1.35mV.

16 fF. Therefore, using the relation Q=CV, 1 mV is taken to be equivalent to 100 e^-. It is seen that the threshold distribution for this chip is well within specifications.

The distribution of the mean threshold and noise for all Class I and II chips in the seven wafer sample is seen in Figure 3-13. It can be seen that all these chips have a mean threshold and noise within the LHCb specifications.

It is also required that the threshold/noise for each chip should be greater than 6. The left hand plot in Figure 3-14 shows the threshold/noise for each of the Class I and II chips in the seven wafer sample. It can be seen in the figure that a small fraction (~7%) of chips have a threshold/noise of less than 6. It has been established that these chips are equally likely to be Class I or Class II. Threshold is plotted against

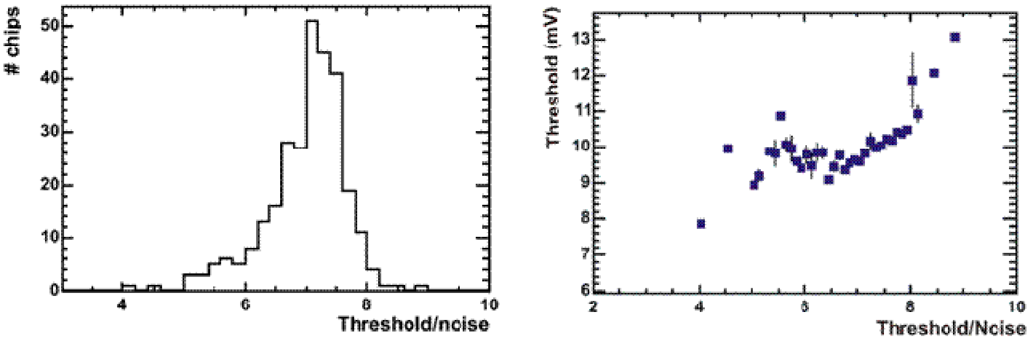

Figure 3-14: Threshold/noise for the chips on the sample of 7 wafers (left). Threshold plotted against threshold/noise (right).

threshold/noise on the right in Figure 3-14. It can be seen that chips with a threshold/noise of lower than 6 have average to low threshold values. A possible explanation of this correlation is that the minimum threshold was not correctly found when performing the threshold scans for these chips, resulting in a high noise level. In addition, the thresholds in these chips are well below the specification of 2000 e^- (~20 mV). Raising the threshold should lead to a decrease in noise and it is therefore expected that these chips can be operated within specifications by simply raising the threshold.

3.3.5 Anode assembly

The tested wafers are sent to an industrial collaborator[7] where the anode assembly takes place. High lead solder (90% Pb – 10% Sn) bumps are deposited on the readout chips, the wafers are diced and Class I chips selected for attaching to silicon detectors. Detector and readout chips are aligned and attached. The assemblies are then returned to the laboratory for the next stage of evaluation. Three batches of assemblies were produced from this sample of seven readout chip wafers. These are termed batches #1, #2 and #3, and contained 10, 11 and 11 assemblies respectively. The results of the assembly testing are reported in this section. The anodes from batch #1 were used to manufacture the first 40 MHz prototype HPDs. Due to problems described below a modification in the bump-bonding procedure was made before the production of batches #2 and #3.

---

[7] VTT Electronics, Finland

Assembly testing

The same test system shown in Figure 3-7 is used for assembly tests, which are again carried out at the probe station. The assembly is placed on a specially adapted chuck designed to hold an assembly in place, rather than a wafer as previously. An extra needle is also required in order to provide reverse bias to the silicon detector. The needle, which is independent of the probe card, must connect with the aluminium ring around the edge of the backside of the detector (see Figure 3-1).

The functionality of the chip is tested in order to verify that the chip has survived the bump-bonding process. This is done by repeating tests that were carried out when testing the readout chip on the wafer. The analogue and digital currents are checked, and then the minimum threshold is found and a threshold scan is carried out.

Once it has been established that the readout chip performance has not degraded as a result of the bump-bonding procedure, the bump-bond quality can be investigated and the detector itself can be tested for the first time. The quality of the bump-bonding is tested using a radioactive ^{90}Sr source emitting electrons with average energy 0.935 MeV. The source is placed ~ 5 cm above the assembly, one million random triggers are sent to the readout chip and the number of fired pixels is counted. The number of fired pixels in this time gives an estimate of the number of good bump-bonds. The detector is tested by measuring the leakage current, which is tracked as a function of the detector bias voltage.

ASSEMBLY NUMBER	BATCH #1			BATCH #2	BATCH #3
	Bare Assembly	After Packaging	After Bake Out	Bare Assembly	Bare Assembly
1	Chip Failure			99.7	99.4
2	Chip Failure			99.9	99.5
3	98.3	Short Circuit		90.2	99.4
4	99.4	Chip Failure		99.7	99.5
5	88.0	89.5		98.4	99.1
6	90.5	92.2	94.3	99.3	98.2
7	85.0	83.5		99.6	99.8
8	98.5	99.0		99.5	99.1
9	98.0	97.7		98.8	98.3
10	93.6	94.3	94.0	99.7	18.1
11				99.7	78.4

Table 3.2: Results from laboratory tests on all assembly batches. Numbers are % pixels fired after 1M random triggers have been sent to the chip. Uncertainty on numbers ~ 1%. Batch #1: numbers quoted for bare assembly tests and results of re-test after packaging and bake-out processes in the cases where it occurred (grey shading indicates process not carried out on that assembly). The red shading highlights the two assemblies used in the production of the first two 40 MHz prototype HPDs.

Results

The results of the tests are summarized in Table 3.2.

In batch #1 the chips used for assemblies 1 and 2 did not survive the bump-bonding process. The ^{90}Sr source test showed that of the remaining eight assemblies only four of them satisfied the LHCb requirement of > 95% operational channels [rich00]. Figure 3-15 shows the chip response, plotted column number against row number; non-fired pixels are indicated in white. It is clearly seen that in the bottom left hand corner of assembly 7 there is an area where many bonds are badly formed.

The bump-bonding process was reviewed as a result of these unsatisfactory results. It was found that a crust had formed on the surface of the bump before the anode was assembled. It is believed that this crust hindered the bonding process. Indeed, the industrial collaborator reported that during bonding higher than foreseen

Figure 3-15: Chip floor plans showing fired (black) and non-fired(white) pixels after 1M random triggers sent and using ^{90}Sr source. Batch #1, assembly 7 (left) and assembly 4 (right).

temperatures and forces were required. This treatment resulted in many badly attached bumps and short circuits, and is also believed to be the explanation for the two chip failures. Figure 3-16 compares photomicrographs of a 'crusted' bump and an ideal bump.

The composition of the bonds used to attach the detector and readout chips in batch #1 is different from the 'standard' composition used in industry, and that used in previous HPD development studies. Standard bonds are made using tin-lead (Sn-Pb) alloy solder containing approximately 60% Sn and 40% Pb with a melting point of 180°C, known as eutectic solder. The previous generation of HPD prototypes had similar anodes, consisting of a silicon sensor bump-bonded to a readout chip, however

Figure 3-16: Photomicrographs showing bump with crust (left) and perfect bump (right) operated at 10 MHz. The anodes for these 10 MHz prototypes were bump-bonded using eutectic solder. The anode quality deteriorated in these tubes after the final stage of HPD production including the bake-out (see section 3.2.1). This deterioration in the number of good bump-bonds is thought to be the result of the bake-out cycle which has a maximum temperature of 300 °C, higher than the melting point of the solder bonds. For this reason the bond composition was changed for the 40 MHz prototypes to a high lead content solder with a melting point of ~300 °C.

Before bump-bonds can be deposited on the readout chip a layer of copper is applied to the chip to provide a surface that the solder bumps will bond to easily. This copper layer is applied to the whole chip, the bonds are deposited and then the copper layer is removed by etching around the bump sites. Crusts like the one seen in Figure 3-16 form because the etchant used to remove the copper reacts with the lead in the solder bumps to form lead sulphate. This does not occur when standard solder is used as the tin content passivates the lead against this reaction taking place. Therefore, the bump-bonding procedure was modified for batches #2 and #3. In order to prevent the crusts from forming, an extra layer of eutectic solder was deposited after lead

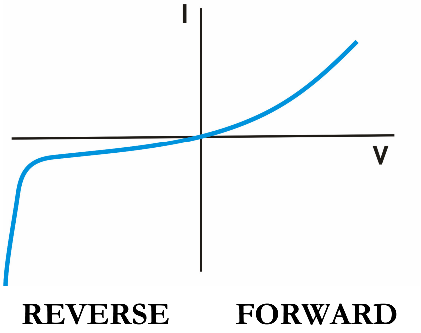

Figure 3-17: Expected I-V behaviour of a diode.

deposition. The tin in the eutectic solder passivates the lead surface and inhibits the formation of lead sulphate [cam04].

The detector leakage current (I) was measured as a function of bias voltage (V) for nine of the ten assemblies in batch #1. Only nine of ten were measured as one detector showed extremely high leakage currents, indicating a bad detector, and the test was abandoned. The expected I-V behaviour of a diode is shown in Figure 3-17. The reverse bias applied to the silicon detector is increased and a measurement of the leakage current is taken at each stage. The measurements made for the nine assemblies are shown in Figure 3-18. Six of the nine detectors measured show the expected slow rise of leakage current with increasing bias voltage, although two of these have an elevated leakage current value. The three other detectors display a sharp rise in leakage current at high values of bias voltage. This is thought not to be the sharp rise due to the breakdown of the detector, but the result of crystal imperfections at the detector edge caused when the detector is diced [wyl98]. These high leakage currents should be prevented from entering the pixels by the guard ring.

As there were insufficient readout chips prepared with the modified procedure

Figure 3-18: Measured I-V behaviour for assemblies in batch #I under reverse bias. Some detectors show expected behaviour (left) but others show a sharp rise in leakage current at high bias voltages (right) for bump-bonding, it was necessary to use chips with crusty bonds for assemblies 10 and 11. These show a poor performance characteristic of that seen in batch #1 giving further confidence that the problem with the bump-bonding is well understood. The results from batch #2 and batch #3 are summarized in Table 3.2. The results from the second two batches are clearly much improved, indicating the success of the revised bump-bonding procedure.

3.3.6 Packaging the anode

The next stage in the production requires that the bump-bonded assembly is packaged in a ceramic pin grid array (PGA) carrier. As shown in Figure 3-5 this forms the base of the HPD. Signals are routed to and from the readout chip through the carrier pins. A photograph of an assembly packaged in a carrier is shown in Figure 3-19. The assembly is glued using Ag glass at a temperature of 410 °C. When the assembly is in place wire bonds are made between the chip and the carrier using a

Figure 3-19: Photograph of an assembly packaged in a carrier. Wire bonds from the carrier to the sensor chip can be seen in the left.

technique called "gold ball wire bonding" (see Figure 3-1).

Tests are again carried out using the system shown in Figure 3-7. However, now the chip has been packaged the probe card is no longer required. The carrier pins plug directly into a socket mounted on a Printed Circuit Board (PCB). This PCB plugs directly into the test system motherboard.

Before going ahead with the packaging of assemblies, a readout chip, without being bump-bonded to a sensor, was glued and wire-bonded into a carrier in order to check that the signals are routed to and from the readout chip through the carrier pins correctly. The analogue and digital currents were measured, the DACs were scanned and a threshold scan was performed. The successful results of these tests proved that the signals were being routed correctly to and from the chip by the carrier. A threshold scan of a packaged chip can be seen in Figure 3-20. The mean and width of the Gaussian fit to the distribution are consistent with those seen previously (see Figure 3-12).

The packaged chip was used to evaluate the suitability of two alternate designs of the socket into which the carrier plugged. The standard socket used in the tests described here is a robust, customized socket. It is envisaged that the final system will use the 'Socket 7' which although less robust, is commercially available Socket 7 and considerably cheaper than the customized alternative.

Figure 3-20: Result of a threshold scan for a readout chip packaged in a ceramic carrier. The mean threshold is 10.3 mV and the width of the fitted Gaussian os 0.9 mV

The packaged chip was plugged into a Socket 7 chip and the usual tests were carried out: a check of the analogue and digital currents, DAC scans and a threshold scan. These results were compared with the results taken using the robust socket normally used for testing. Figure 3-21 shows a comparison of the results of threshold scans for the two sockets. Threshold scans were performed at three different threshold settings for both sockets. No significant performance difference is seen between the two sockets. As a result of this test, Socket 7 is confirmed as the socket to be used in the final design.

After the carrier had been tested using a readout chip and the socket tests, the 8 working assemblies in batch #1 were packaged in carriers. This process was again carried out in industry and the packaged assemblies were then returned to the laboratory for further tests. As discussed in section 3.2.1 the packaging process involves the gluing of the assembly into the carrier using silver glass. The silver glass is heated to 410 °C and the assembly is fixed in place. Due to the short duration of this process the temperature of the bump-bonds do not reach their melting point of 310 °C. However, once the assembly is fixed in place new strains may be exerted on the bonds and it must

Figure 3-21: Comparison between threshold scans carried out using Socket 7 (solid line) and the customized socket (dotted) at three different threshold settings

be verified that the bonds do not become unattached as a result. The series of tests carried out on bare assemblies described in section 3.3.5 are repeated for the packaged assemblies.

Results

The results of the tests on the packaged batch #1 assemblies are summarized in Table 3.2.

Two of the assemblies experienced problems during the packaging. In assembly 3, a short circuit developed between the sensor and the carrier as a result of some of the silver glass glue coming into contact with the sensor. Assembly 4 suffered a chip failure for unforeseen reasons. In the remaining assemblies no deterioration of the number of good bump bonds was seen with respect to the situation prior to packaging.

3.3.7 Bake Out tests

As part of the HPD production process described in section 3.3.1 the HPD tube, once assembled, undergoes a thermal cycle as part of the evacuation process. The temperature is increased over 6 hours to 300 °C and remains at 300 °C for 3 hours. The temperature is then decreased to room temperature over a further 6 hours. The melting point of the lead-solder bumps themselves is known to be 310 °C, which is above the bake-out cycle temperature. However, during the bump-bonding process the bonds can receive contamination with nickel from the under bump metallization. It is not known what effect this has on the melting point of the bumps.

In order to test the robustness of the bump-bonds to this thermal cycle, assemblies 6 and 10 from Batch #1 were subjected to the same temperature conditions. The assemblies were placed in a vacuum and the temperature was varied as in the manner described above.

The quality of bump-bonds was tested using the ^{90}Sr source after the thermal cycling. The results of these tests can be seen in Table 3.2. The apparent 'improvement' in the number of working pixels in assembly 6 is attributed to a statistical fluctuation in the measurement. No degradation in the number of good bump-bonds is seen and it is concluded that the bump-bonds survive the bake-out process.

3.3.8 Summary

Two prototype HPDs operating at 40 MHz were produced with numbers of operational channels that meet LHCb requirements. As a result of the comprehensive test carried out at each stage of the production process lessons have been learnt and modifications have been made. It is also now possible to define a strategy for carrying out quality control tests during the production of the full batch of 600 HPDs. The performance of these HPDs has been tested in the laboratory and in beam tests. Results from the beam test are described in Chapter 4.

3.4 HPD readout electronics and the Analogue Pilot

3.4.1 Overview

As explained in section 3.3.2 the readout chip requires 6 external reference voltages, two that set the magnitude of the test pulse and four that provide references for the 42 readout chip DACs. In the tests described above these references were provided by the motherboard in a dedicated system suitable for laboratory evaluation (see Figure 3-7). However, in reading out the RICH detectors during LHCb operation a different solution is required and in this system the six references are provided by a single chip called the Analogue Pilot. Figure 3-22 shows a schematic of the design for the front-end electronics to be used to read out the HPDs in LHCb. For a more detailed description of the readout electronics for the RICH detectors see [bib04]. Two HPDs will be served by one front-end electronics board as shown in the diagram. This board contains one Analogue Pilot which will provide the six references for both HPDs. The Pixel INTerface (PINT) provides the control signals required to read data from the HPD. These signals are described in detail in section 3.3.2. After each event, data are stored in the readout chip buffers until a Level-0 trigger decision had been made. The global experiment clock and L0 trigger decisions are received via the Timing and Trigger Control receiver (TTCrx). The Timing and Trigger Control (TTC) system is used to distribute synchronisation and trigger signals throughout the LHCb experiment. On the receipt of a positive L0 trigger decision, data are shifted out of the

Figure 3-22: Schematic of the front-end readout electronics board used to readout HPDs in the LHCb experiment

readout chip by the PINT and sent via optical links to the L1 electronics which are located at a distance of approximately 100 m away from the detector.

3.4.2 Analogue Pilot

A schematic of the Analogue Pilot chip is shown in Figure 3-23. The Analogue Pilot contains six 8-bit DACs that are configurable using JTAG which provide the six reference voltages. In addition to these the Analogue Pilot contains a 10-bit ADC (analogue to digital converter) and a multiplexer (MUX). This system of multiplexer and ADC allows 16 different analogue values to be monitored. The input to the ADC is chosen from one of the 16 multiplexer inputs. The 16 inputs include the 6 reference voltages that the analogue pilot is providing; the analogue and digital power supplies to the readout chip, VDDAPC and VDDDPC; two temperature monitoring inputs, T1 and T2; and the values of the readout chip DACs, DACPCV and DACPCI. In addition to these inputs a further 4 are unassigned, AUX1-4.

Figure 3-23: Schematic diagram of the analogue pilot functions

3.4.3 Analogue Pilot providing references for readout chip

The performance of the Analogue Pilot was tested by incorporating it into the readout chip test system. The Analogue Pilot was added to the test system in such a way that the source of each of the reference voltages was selectable as either coming from the test system motherboard or from the analogue pilot. As the value of the Analogue Pilot DACs are also set using JTAG, the LabVIEW software was adapted so that it could be used to control both the motherboard and the Analogue Pilot. Threshold scans were then carried out on a chip where references were provided first by the motherboard and then by the Analogue Pilot. Results using the two different systems were then compared.

Once the system was set up it became apparent that there was a problem with one of the 6 reference voltages supplied by the Analogue Pilot. The values of DAC_REF_VDD could not be set to the required value of 1.8 V. It was then realised that a buffer had been omitted from the design of the Analogue Pilot which meant that the output was not driving the required amount of current needed to supply the reference to the readout chip. Due to this fault the Analogue Pilot could only provide 5 of the 6 references, leaving the motherboard to provide DAC_REF_VDD. In order to eliminate the motherboard from the test DAC_REF_VDD was tied to the Analogue Pilot supply voltage VDD, which is also 1.8 V. Figure 3-24 show the results of threshold scans carried out firstly where all references are provided by the test system motherboard, and secondly where the Analogue Pilot provides 5/6 references and DAC_REF_VDD is tied to the Analogue Pilot VDD. The small increase in noise in the case where the Analogue Pilot was used to supply the references is attributed to imperfect grounding in the test setup.

Mean= 12.14
σ = 0.87
Mean= 10.66
σ = 0.99

Mean = 1.27
σ = 0.13
Mean = 1.42
σ = 0.18

Figure 3-24: Threshold (left) and noise (right) distributions. The black dotted line shows the distributions for the case where all references are provided by test system motherboard. The blue dotted line shows the distributions for the case where references are provided by the Analogue Pilot, however with DAC_REF_VDD tied to the Analogue Pilot VDD. The solid lines are Gaussian fits the mean and width of which are given above.

Mean = 8.85
σ = 0.95

Figure 3-25: Threshold scan where the Analogue Pilot-v2 is providing the six reference voltages

As a result of these tests the design of the Analogue Pilot was modified to include the missing buffer and the 'Analogue Pilot – v2' was produced. The above tests were repeated with the new version of the chip and it was found that all 6 references could now be supplied to the readout chip. Figure 3-25 shows the threshold distribution where the Analogue Pilot – v2 was used to provide all 6 references for the readout chip.

3.4.4 Variation of references with temperature

The 6 reference voltages that the Analogue Pilot provides are derived from a bandgap voltage reference circuit. This commonly used circuit provides a precise voltage reference of 1.2-1.3 V which is close to the theoretical bandgap of silicon at 0° K [bro74]. The voltage reference that the bandgap circuit provides has a dependence on operating temperature and therefore the 6 reference voltages which are derived from this reference they will also vary with temperature. Figure 3-26 shows the measured variation of the 6 references with temperature. The most significant variation is in DAC_REF_HI which shows a total voltage change of 75 mV over the interval 20 – 60 °C. The other five references show a change of

Figure 3-26: Plots showing the variation with temperature of the 6 reference voltages provided by the Analogue Pilot

~ 10 mV over the same range. The implication of this is that the operating temperature of the Analogue Pilot should be known in order to know the analogue value that corresponds to each digital code.

3.4.5 The analogue pilot ADC

The multiplexer and ADC on the analogue pilot chip allows 16 different values to be monitored, including temperature and the 6 reference voltages. It is envisaged that the ADC will be used to monitor these quantities during operation.

Threshold scans will be carried out for test purposes in the final system. In order to carry out a threshold scan successfully the values of the test pulse reference voltages, analogue_test_hi and analogue_test_lo, must be known with an accuracy of 1 mV, as the steps in the test pulse are of this order. The most reliable way to ensure that this requirement is met is to calibrate each individual analogue pilot. Every analogue pilot would have an entry in a database containing the analogue output corresponding to each of the 256 digital input codes. However, if the ADC were to give an accurate read back value then the calibration may be unnecessary.

Figure 3-27 shows the measured values of two of the references, DAC_REF_HI and analogue_test_lo, compared with the value read by the ADC over the temperature interval 20 – 60 °C. As the remaining four DACs are identical to analogue_test_lo and for this reason were not tested. The ADC values are the average of 100 readings taken. The values read back for DAC_REF_HI are close to those measured. For analogue_test_lo, an offset of ~ 5 mV is seen between the measured and the read back values. The operating temperature of the electronics is expected to be stable. In addition to this the offset and read back performance of the ADC does not vary with temperature. It is therefore expected that calibration of the analogue pilot chips will not be required.

3.5 Summary of Analogue Pilot studies

The Analogue Pilot will provide 6 reference voltages for the HPD readout chip and the Analogue Pilot-v2 is able to provide these references. Only one Analogue Pilot chip has been studied in these tests and the studies have shown that there can be an

Figure 3-27: Measured DAC value and those read back by the ADC for two reference voltages offset between the actual value of the reference and the value read back by the ADC. As the value of this offset could vary from chip to chip, a larger sample of chips must be tested in order to establish whether calibration of the Analogue Pilot chips is required. The temperature dependence of the voltage references should also be examined further, however this study indicates that the temperature dependence of the references is reasonably linear. It is particularly important to know the values of the two references that set the size of the test pulse accurately in order to be able to carry out a threshold scan and successfully set the minimum threshold of the HPD readout chip.

Chapter 4

HPD test beam analysis

4.1 Introduction

Two prototype HPDs operating at 40 MHz were produced as a result of the work presented in Chapter 3. In the autumn of 2003 these prototype HPDs were tested in a beam of charged particles on two occasions. The first of these, the HPD beam test, was designed to study the performance of the prototypes with Cherenkov photons produced in an air radiator. In the second, the Aerogel beam test, the prototypes were used to detect Cherenkov photons produced in an aerogel radiator. These tests allow

Figure 4-1: Schematic of the setup used in the HPD beam test. The beam enters the vessel from the right. Cherenkov photons are produced in the air and reflected off the mirror onto the HPD. Scintillators are arranged before and after the vessel to provide a trigger and limit the beam divergence.

the study of both the HPD performance and properties of the aerogel relevant to its performance as a Cherenkov radiator. Results of studies made on data taken in both test periods are presented in this chapter.

4.2 HPD Beam Test

4.2.1 Overview

These tests are designed to evaluate the performance of the two prototype 40 MHz HPDs in test beam conditions. The tests took place in station T9 of the PS beam at CERN. The experimental setup is shown in Figure 4-1. The beam enters the light tight vessel from the right and Cherenkov photons are produced in the air within the vessel. These photons are focused onto the HPD by a spherical mirror.

The HPDs used in these tests are the two prototype HPDs produced as a result

Figure 4-2: Measured Quantum efficiencies of the 40 MHz prototype HPDs. Measurements courtesy of DEP.

of the work described in Chapter 3. These prototypes were made using assembly numbers 8 and 9 from batch #1. These HPDs are referred to as HPD1 and HPD0 respectively from now on.

4.2.2 Experimental Arrangement

The beam is set to contain 10 GeV negative particles. The momentum resolution is of the order 1% and the composition of the beam is approximately 95% pions and 5% electrons.

A full-scale LHCb RICH prototype vessel, which is described in detail in [alb98] , was used. Figure 4-1 is a schematic drawing of this vessel, which contains air at room temperature and atmospheric pressure that serves as the Cherenkov radiator. Cherenkov photons that are produced in the air within the vessel are reflected onto the HPD by a spherical mirror mounted at the back of the vessel. The mirror is tilted with

Figure 4-3: Timing diagram of the HPD readout. An asynchronous signal arrives anywhere within a 25 ns clock period shaded in red. The discriminated signal is synchronised to the readout clock. The trigger signal must arrive such that it is at logic level 1 on the same clock edge as the synchronised signal. The trigger signal is also asynchronous and jitters within a 25 ns period shown by the red arrow.

respect to the beam in order to focus the Cherenkov photons onto the mounted HPD. The performance of two prototypes is studied using this arrangement with only one HPD mounted at a time. The measured quantum efficiencies of the two 40 MHz HPDs studied here are shown in Figure 4-2.

Two scintillators read out by photomultiplier tubes are placed either side of the vessel, as shown in Figure 4-1. A coincidence in all four scintillators is required to trigger readout of the HPD. The smaller scintillator on each side of the vessel has dimension ~ 1 cm^2. These scintillators are positioned ~ 8 m apart and limit the beam divergence to ~ 1.5 mrad. The beam and therefore the scintillator trigger are asynchronous to the 40 MHz readout chip clock. After a signal has been amplified, shaped and discriminated within the analogue front end of the chip, the signal is

Figure 4-4: The photoelectron yield as a function of the trigger delay. The measurement was performed with a 25 ns long trigger signal using HPD1. The measurement is taken at two different preVTH (threshold) settings where preVTH = 222 is the lower threshold.

synchronised to the 40 MHz clock. In order for the signal to be read out, the trigger signal must arrive at the chip so that it is at logic level 1 on the same clock edge as the synchroniser output. A timing diagram for this process is shown in Figure 4-3. The trigger signal produced as a result of a coincidence in the four scintillators is 25 ns long and can arrive anywhere in a 25 ns clock period. In order to optimise the efficiency, timing scans were made where the delay with which the trigger arrived at the chip was adjusted.

The result of the timing scan is shown in Figure 4-4. The triangular shape is due to the fact that there is only one optimal delay of the trigger when the trigger and synchroniser output are always at logic level 1 on the same clock edge. In the first measurement of the scan, the delay of the trigger is set such that the trigger arrives too soon and no hits are read out. As the trigger is asynchronous to the readout clock the trigger signal jitters within 25 ns and as the delay is increased the number of hits gradually increases until the optimum point where all hits are read out. If the delay is

Figure 4-5: The red line represents the signal in a pixel when a photoelectron loses its full energy. The blue line represents the signal in a pixel when the photoelectron energy has been shared between neighbouring pixels. The green line represents the level at which the signals are discriminated. The blue line the signal crosses the threshold at a later time and the signal is assigned to the following clock cycle.

increased further beyond this point the number of hits read out begins to decrease. The tail at high values of the trigger delay is due to charge sharing. The term 'charge sharing' describes the situation where the charge deposited in the silicon by one photoelectron is shared between neighbouring pixels. The signal in each pixel is smaller, but has the same peaking time as the full photoelectron signal. Consequently the discrimination of the smaller signals occurs later introducing a delay which can cause these signals to be synchronised to the following clock tick.

The HPD is read out using the test system described in detail in section 3.3.3. Data from the HPD can be read out in either ALICE mode, where each of the 8192 pixels are read out individually, or in LHCb mode, where the output of 8 pixels grouped vertically are coupled with a logical OR after the discriminator. A comparison of ALICE mode readout and LHCb mode readout is shown in Figure 4-6. Software routines developed by the author are used for offline conversion of raw binary data

Figure 4-6: Cherenkov ring from 10 GeV beam in HPD beam tests. LHCb readout mode (left) is compared with ALICE readout mode (right). A grey scale indicates pixel occupancy. The full cathode image is visible on the LHCb mode plot due to the logarithmic scale used. In the ALICE readout mode the ring from pions (inner ring) can be resolved from that ring due to electrons (outer ring) from the HPDs to a format suitable for analysis using ROOT [bru96].

4.2.3 HPD performance

A number of tests were carried out to verify that the HPDs perform as expected. These were done by measuring the photoelectron yield which is defined as the average number of photoelectrons detected per event. In order to calculate the photoelectron yield the number of hit pixels are counted. Charge sharing is accounted for when analysing the data read out in ALICE mode. This is done by using a clustering algorithm which finds hits in neighbouring pixels. All clusters of hits are assumed to originate from a single photoelectron. The clustering procedure results in an underestimation of the photoelectron yield as the probability for finding hits from two

Figure 4-7: Photoelectron yield as a function of discriminating threshold, preVTH.

Figure 4-8: The photoelectron yield as a function of the tube high voltage carried out at preVTH = 218.

photoelectrons in adjacent pixels is not zero. In LHCb mode no clustering is performed and the average number of fired pixels is taken as the photoelectron yield. Charge sharing is less important in LHCb readout mode as the dominant component of charge sharing is between vertical pixels and the pixel outputs are already grouped vertically. Applying no clustering correction does however result in a small overestimation of the photoelectron yield when analysing data taken in LHCb mode.

The photoelectron yield as a function of the readout chip discriminating threshold, preVTH, for HPD0 is shown in Figure 4-7. An increase in preVTH value corresponds to a decrease in the threshold. The HPD performs as expected, showing a gradual rise in the photoelectron yield with decreasing threshold, until the noise level is reached at a preVTH value of approximately 230, corresponding to ~ 2000 e^-.

Figure 4-9: Photoelectron energy spectrum measured using an ADC. The left hand peak is the pedestal. The thin peak shows where the threshold is set. The main full energy peak is on the right. Between the pedestal and full energy is the distribution due to backscattered photoelectrons. The integral of this part of the distribution is 18% of the main peak. Plot courtesy of T. Gys (CERN).

The photoelectron yield is also measured as a function of the tube high voltage. This scan was carried out at a threshold setting of preVTH = 218. The results for HPD1 are shown in Figure 4-8. The HPD again behaves as expected with a sharp increase in detector response once the readout chip discriminator threshold has been exceeded. The fact that a plateau in efficiency is not reached in Figure 4-8 can be explained by considering an effect called back-scattering. There is an 18 % probability [dar75] for photons to rebound at the silicon surface. These photons are said to have 'back-scattered'. Figure 4-9 shows the photoelectron energy spectrum where the left hand peak is the pedestal, the thin central peak indicated the position of the threshold and the full energy peak is on the right. Stretching between the pedestal and the full energy peak is the part of the spectrum due to back-scattering. At a given high voltage, the detected signal corresponds to the integral of the spectrum above the threshold. As the high voltage is increased the position of the high voltage peak changes. The photoelectron yield does not reach a plateaux once the main peak is completely above threshold because a component of the spectrum is due to back-scattering. This effect can be seen in both Figure 4-8 and Figure 4-7.

4.2.4 Photoelectron yield in ALICE and LHCb readout mode

The photoelectron yields measured in data taken in ALICE and LHCb readout modes are compared to verify that no losses are introduced in LHCb mode operation. Measurements are made using HPD1 at two threshold settings, preVTH = 222 and preVTH = 214, corresponding to approximately 1200 e^- and 1700 e^- respectively. The tube high voltage is set to 18 kV. The photoelectron yields in data in the two readout modes are given in Table 4.1

A Monte Carlo calculation has been performed for comparison with the observed data. The Monte Carlo program generates a number of photoelectrons on the anode according to a Poisson distribution. In the Monte Carlo the photoelectrons are distributed uniformly on a ring, the radius of which varies according to a Gaussian distribution. Charge sharing is simulated by specifying a probability for a hit pixel to share its charge with a neighbouring pixel, either vertically, horizontally or diagonally. All parameters are tuned to give good agreement between the analyses of the Monte Carlo and the ALICE mode data. The number of photoelectrons used as an input is chosen so that the proportion of two-pixel clusters per event is the same in data and Monte Carlo. The input values are 6.43 for pre_VTH = 214 and 6.90 for pre_VTH = 222. The same input parameters are used to generate Monte Carlo in both ALICE and LHCb mode.

preVTH	Readout mode	Data	MC Output
214	ALICE	6.27	6.25
	LHCb	6.43	6.40
	ALICE (offline LHCb)	6.38	6.40
222	ALICE	6.68	6.66
	LHCb	6.90	6.96
	ALICE (offline LHCb)	6.92	6.96

Table 4.1: Comparison of photoelectron yields found for two readout modes in data and Monte Carlo at two threshold values.

Table 4.1 gives the photoelectron yields found in both ALICE and LHCb mode in Monte Carlo. By grouping vertically sets of eight pixels it is possible to analyse data taken in ALICE mode as if they were taken in LHCb mode. The photoelectron yield is also calculated from the ALICE mode data in this way and is given in Table 4.1 as 'offline LHCb'. The good agreement between the number of photoelectrons found for data and Monte Carlo in LHCb mode confirms that no loss is introduced by in this readout mode. Approximately 3% of all photoelectron hits are lost in LHCb mode as they fall within the same large LHCb pixel. This effect is compensated due to extra hits from charge sharing in these tests. The ALICE mode data photoelectron yield shows the effect of the underestimation due to the clustering correction.

4.2.5 Photon detection efficiency

The expected photoelectron yield is calculated in order to compare with the observations made. This yield is calculated using equation 2.2 with the addition of factors that account for experimental losses. The expression that is used is

$$\mathrm{N}=2\pi\alpha\mathrm{L}\int \mathrm{R}(\lambda)\mathrm{QE}(\lambda)\frac{1}{\lambda^2}\left[1-\frac{1}{\left(\beta\mathrm{n}(\lambda)\right)^2}\right]d\lambda\,. \qquad 4.1$$

The quantity α is the fine structure constant and L is the length of the Cherenkov radiator, which in this case is 1000 mm as shown in Figure 4-1. $R(\lambda)$ is the reflectivity of the mirror, $QE(\lambda)$ is the quantum efficiency of the photodetector, $n(\lambda)$ is the refractive index, λ is the wavelength of the Cherenkov radiation and $\beta=v/c$.

Losses due to the presence of the glass filter are approximately 10% above 300 nm as can be seen in Figure 4-11. In laboratory tests using a laser light source losses due to missing pixels have also been calculated to be 1 – 2 % for HPD0 and HPD1 [mor04]. Taking these factors into account the expected number of photoelectrons detected per event, N = 8.6. At the lowest threshold, 6.9 photoelectrons are detected per event giving a photon detection efficiency of 80 %. This value compares with detection efficiencies of 88 % found in the laboratory tests where the tube high voltage is 20 kV.

4.2.6 Conclusions from the HPD beam tests

The HPD beam tests show that the two 40 MHz prototype HPDs are capable of detecting Cherenkov photons. The tests also demonstrate that the HPDs exhibit a good photoelectron yield that has the expected dependence on high voltage and discriminating threshold.

Readout of the HPD has been performed in both ALICE and LHCb mode. Photoelectron yields have been calculated for data taken in both modes. These numbers have been compared with a Monte Carlo calculation and it has been verified that no significant losses are introduced by readout in LHCb mode.

4.3 Aerogel Beam Tests

4.3.1 Overview

The aim of these beam tests is to study the properties of recently manufactured aerogel tiles as well as to study the performance of the HPD prototypes. The results from the beam tests are compared with a Monte Carlo simulation of the experimental

Figure 4-10: Schematic drawings showing the setup for the aerogel beam tests. The geometry of the vessel is shown where C indicates the centre of curvature of the mirror. The arrangement of the three HPDs in the plane and the position of the silicon telescope planes with respect to the vessel are also shown setup.

The tests took place in the T9 area of the CERN PS facility. The experimental setup consists of a light tight aluminium vessel, aerogel radiator, spherical mirror and 3 HPDs. Schematic drawings of the setup are shown in Figure 4-10. The beam enters the vessel from the right and the beam direction is measured for each event using a silicon telescope. Cherenkov photons are produced as charged particles pass through the aerogel, which is mounted on a table within the vessel. These photons are reflected by the spherical mirror onto the photodetector plane which contains three prototype HPDs. The two 40 MHz prototype HPDs are used along with another HPD prototype which has identical electron optics, but a different anode operating at 10 MHz.

4.3.2 Experimental Arrangement

The beam is set to have the same properties as used in the HPD beam tests, and the readout is triggered using an identical arrangement of scintillators. In these tests a silicon telescope is used to provide the beam direction on an event-by-event basis and to give a measurement of the beam divergence. The silicon telescope consists of three planes of silicon pixel detectors, each with 22 × 22 pixels of dimensions 1.3 × 1.3 mm. The three silicon telescope planes are placed along the beam line, arranged as shown in Figure 4-10, with the first and last planes separated by ~ 5 m. The right handed coordinate system is defined such that the nominal beam direction gives the z axis, y is vertical and the point $x = 0$, $y = 0$ is the centre of the front face of the vessel where it touches the floor. Tilts of the vessel of the order 10 mrads are introduced in order to account for the fact that the floor was not perfectly flat.

Figure 4-11: Transmission of the glass filter (D263 - 100μm) as a function of wavelength

Four aerogel tiles, each measuring approximately $10\times10\times4$ cm^3, are mounted on a table within the vessel. These aerogel tiles were manufactured at the Boreskov Institute of Catalysis in Novosibirsk [dan99]. The tiles are arranged 2×2 and are closely packed. Nitrogen is flushed through the vessel to protect the hygroscopic aerogel tiles from humidity. A 100 μm thick glass filter can optionally be placed immediately after the aerogel. Figure 4-11 shows the transmission of the filter used as a function of wavelength. Due to the dependence of refractive index on wavelength that can be seen in Figure 4-15, photons with low wavelength are produced at a larger Cherenkov angle. This effect leads to the presence of a tail in the Cherenkov angle distribution towards higher values which will lead to a degraded resolution on the measurement. The filter absorbs low wavelength photons and thus removes the ‘chromatic tail’ from the distribution, reducing measurement error. The filter will also remove Rayleigh scattered

Figure 4-12: Measured reflectivity of the spherical mirror used in the aerogel beam test. Measurements courtesy of T. Gys *et al.* (CERN)

photons that are more likely to have a low wavelength. Aerogel and Rayleigh scattering are discussed in more detail in section 4.3.4.

The spherical mirror is tilted with respect to the beam. The mirror has a radius of curvature of 949 mm and any Cherenkov photons produced in the nitrogen are focused in the insensitive region between the HPDs. The measured reflectivity of the mirror is shown in Figure 4-12. The dip in reflectivity at around 300 nm is due to interference effects in the aluminium mirror coating.

Three HPDs are arranged on the photodetector plane as shown in Figure 4-10. HPD0 and HPD1 are the two 40 MHz prototype HPDs studied in the HPD beam tests. HPD2 is prototype with identical electron optics, but a slightly modified anode which operates at 10 MHz. The anode of HPD2 has the same number of pixels as HPD0 and HPD1, but with individual dimensions of $425 \times 50\ \mu\text{m}^2$ as opposed to $500 \times 62.5\ \mu\text{m}^2$. The measured quantum efficiencies of HPD0 and HPD1 are

Figure 4-13: Measured quantum efficiencies of the three HPDs used in the aerogel beam tests. Measurements on the left courtesy of DEP. Measurements on the right courtesy of T. Gys, CERN

compared with that of HPD2 in Figure 4-13. The measurements taken by the tube manufacturers are compared with similar measurements performed at CERN. The difference between the two measurements gives an indication of the error on the quantum efficiency measurement. HPD0 and HPD1 were produced in the same batch in 2003 whereas HPD2 was produced in a separate batch two years earlier. The quantum efficiency of the tubes may vary between batches.

As HPD2 can only be read out at a maximum of 10 MHz, all three HPDs are read out at this frequency. The test system used previously for 40 MHz operation is replaced by a readout system designed for use with ALICE pixel chips[10]. Data are read out from the HPDs using VME pilot cards. This VME card contains a pilot chip which has been designed to zero suppress data from pixel chips. Data are sent from the VME pilot card to the FLIC. LabView software is again used to control data taking and configure the pixel chips in the three HPDs. Software routines have been developed by

---

[10] ALICE pixel chips are operated at 10 MHz

the author for offline conversion of raw binary data from the HPDs into formats suitable for performing analysis (ASCII and ROOT [bru96]).

4.3.3 Data taking

A number of data runs, each containing of the order 30k triggers, were taken using different settings. For most of the runs the beam passed through the centre of the aerogel tile positioned on the top left of the arrangement and the high voltage of the three HPDs was set to 18 kV. In order to assess the effect of the glass filter on the results, consecutive runs were taken with the filter in place and then removed. In another subset of runs, the beam remained in its standard position, but the tube high voltage was varied in steps of 2 kV from 14 kV to 20 kV.

Data runs were also taken in order to assess the contribution to the background from various sources. Using a random trigger and with the aerogel tiles removed, data were taken off the beam spill which are used to give an indication of background due to electronic noise and dark counts in the HPDs. Another run using a random trigger and without the aerogel, but now on the beam spill, are used to assess the contribution of beam related background. Finally, to assess the contribution to the background coming from the aerogel, a run was taken with the aerogel in place using a random trigger on beam spill. In this run a black screen was placed behind the aerogel blocking signal photons. The photons detected by the HPDs in this case could be wide angle scatter photons produced in the aerogel, as well as beam related background, electronic noise or dark counts.

Tile	**1**	**2**	**3**	**4**
Thicknesss (cm)	**4.4**	**4.2**	**4.4**	**4.2**
N	**1.0286**	**1.0292**	**1.0272**	**1.0307**
A (%)	**86**	**87**	**88**	**96**
C (μm^4/cm)	**0.0052**	**0.0056**	**0.0054**	**0.0061**

Table 4.2: Thickness, refractive index (n) measured at λ = 543.5 nm, A and C of the four aerogel tiles. Tile 1 is the tile that was used in the test discussed in this chapter. Measurements made by Tito Bellunato, University of Milano-Bicocca and INFN, Milano Italy.

Other data runs that were taken are not discussed in this thesis. These included runs where the aerogel was removed and smaller nitrogen rings were detected. The HPD positions were adjusted so that the full ring could be captured by each HPD in turn. Other runs left the HPD high voltage at 18 kV, but scanned the beam across the aerogel tiles so that edge effects could be assessed.

4.3.4 Aerogel Radiator and Rayleigh scattering

Aerogel is a very low density silicon based material with refractive index n ≈ 1.03. Charged particles with $\beta \approx 1$ passing through the aerogel produce Cherenkov photons at an angle of 242 mrad with respect to the particle trajectory.

The transmission, T, of light through aerogel is well described by

$$T = Ae^{-CL/\lambda^4} \qquad 4.2$$

where A is the limiting transmission in the high-λ region, C is the clarity coefficient and L is the thickness of the sample. A and C have been determined for the aerogel tiles by measuring the light transmission as a function of wavelength and aerogel thickness and fitting the result using equation 4.2. The properties of each of the four aerogel tiles are given in Table 4.2.

Figure 4-14: ADC counts on the three silicon telescope planes for a representative run

Cherenkov photons may undergo Rayleigh scattering in aerogel. Rayleigh scattering is a wavelength dependent effect which is described by the exponent in expression 4.2. The distribution of Rayleigh scattered photons has a $1+\cos^2\theta$ dependence and must be considered as a source of background. Rayleigh scattering is described in further detail in Appendix A.

4.3.5 The Silicon Telescope

The silicon telescope allows calculation of the beam direction on an event-by-event basis. When a pixel is hit by a beam particle, the charge deposited is converted to a digital value using an ADC (Analogue-to-Digital Converter). The ADC spectra of the three planes for a representative run are shown in Figure 4-14. Cuts are applied to the telescope data that remove the noise pedestal below 125 ADC counts and the saturation effects above 770 ADC counts. The possibility of charge sharing between pixels is taken into account by using a clustering algorithm to find hits in neighbouring pixels. Clusters containing fewer than 5 pixels are assumed to arise from the passage of a single particle and a centre of gravity is found for the cluster. Events with a single cluster on each of the three silicon planes are selected. A least squares linear fit is then made in the XZ and YZ plane independently, giving the beam direction for each event. The best alignment of the silicon planes is found by minimising the residual between the fitted coordinate and the actual coordinate and the central position found in each plane defines the nominal beam direction (0, 0, 1).

4.3.6 Monte Carlo Simulation

A detailed simulation of the beam tests has been developed using GEANT4 which describes the geometry of the experimental setup and the various physics processes [eas04]. A beam of charged pions passes through the vessel. As these charged particles pass through the aerogel, Cherenkov photons are produced with a uniform distribution in energy.

The refractive index of the aerogel is dependent on the wavelength of the photons which leads to the chromatic error on the reconstructed Cherenkov angle described previously. This dependence has been parameterised in two ways. The first parameterisation uses the Sellmeier dispersion relation

$$n^2(\lambda) - 1 = \frac{F_1}{E_1 - \lambda^2} + \frac{F_2}{E_2 - \lambda^2} \qquad 4.3$$

where the Sellmeier coefficients F_i and E_i are material dependent parameters. In order to model the aerogel dispersion, these parameters have been taken from quartz, with F_i scaled down to the density of aerogel. The resulting curve is then further shifted so that it matches the measured refractive index of aerogel at

Figure 4-15: Parameterisations of the wavelength dependence of refractive index, n, for aerogel. n-1 plotted for Clausius-Mossotti method (blue dots); Sellmeier parameterisation scaled from quartz (red) and then shifted to match measurement at 543.5 nm (black).

543.5 nm.

The second method uses the Clausius-Mossotti equation for mixtures

$$\frac{(\mathrm{n}(\lambda)^2-1)}{(\mathrm{n}(\lambda)^2+2)}=\mathrm{V}_\mathrm{s}\frac{(\mathrm{n}_\mathrm{s}(\lambda)^2-1)}{(\mathrm{n}_\mathrm{s}(\lambda)^2+2)}+\mathrm{V}_\mathrm{a}\frac{(\mathrm{n}_\mathrm{a}(\lambda)^2-1)}{(\mathrm{n}_\mathrm{a}(\lambda)^2+2)} \qquad 4.4$$

where the subscript s indicates silica and a indicates air. Measurements of the refractive index are taken at two wavelengths and the equation is solved for V_s and V_a, taking values of the refractive index of silica and air from [pal97], [bor99]. The results of these parameterisations are shown in Figure 4-15. Comparing results from the two parameterisations will give some indication of the error due to the description of the refractive index of the aerogel.

A description of Rayleigh scattering distributed according to $(1+\cos^2\theta)$ is included in the simulation together with a probability for a photon to be absorbed within the aerogel. The resulting transmission curve in the Monte Carlo matches that measured for the tile studied in this chapter. Refraction and reflection at all optical boundaries, for example the aerogel surface, are described using the Fresnel equations [jac75]. The mirror reflectivity is described using the measured reflectivity of the mirror shown in Figure 4-12 [eas04].

The photoelectric process in the HPDs is modelled using the measured quantum efficiencies for each of the three tubes which are shown in Figure 4-13. Photoelectrons are produced with momentum 20 keV/c and are transported to the silicon anode surface using a description of the HPD focusing. Photoelectrons result in a hit on the pixel with an efficiency based on laboratory measurements of the HPDs. The effective efficiency used accounts for these losses due to the back-scattering of photons at the silicon surface. The Monte Carlo output gives a list of hit pixels in each HPD, for each event, just as is obtained from the data.

4.3.7 Cherenkov Angle Reconstruction

The analysis is performed in the same way for both data and Monte Carlo in the coordinate system defined previously. A Cherenkov angle, θ_C, is calculated for each

Figure 4-16: Definition of parameters used in the calculation of the reflection point on the spherical mirror.

Figure 4-17: The reconstructed hits on the HPD photocathodes are plotted, along with the emission points in the aerogel and the calculated reflection points on the spherical mirror for a whole data run.

photon hit on the detector plane. Figure 4-16 shows the parameters used in the calculation. The centre of the hit pixel is taken as the detection point, D. The emission point, E, is assumed to be the midpoint of the track in the aerogel radiator. E is calculated on an event-by-event basis using the beam direction, which in data is calculated using silicon telescope information and which is known in Monte Carlo. The centre of curvature of the mirror, C, is known from measurements. With D, E and C it is possible to calculate the point of reflection on the mirror, M. M, C, D and E all lie on the same plane, therefore the angle β between E and M about C can be calculated. After solving the quartic equation [for98],

$$\begin{aligned}4e^2d^2\sin^4\beta - 4e^2d_yR\sin^3\beta + (d_yR^2 + (e+d_x)^2R^2 - 4e^2d^2)\sin^2\beta \\ + 2ed_y(e-d_x)R\sin\beta + (e^2-R^2)d_y^2 = 0 \qquad 4.5\end{aligned}$$

to find β, the coordinate of M can be determined. Figure 4-17 shows the results of this calculation where D, E and M are plotted for all the events in a data run. The direction of the photon emission $\overline{P}$ is then found using E and M and finally θ_C, which is the angle between $\overline{P}$ and the beam direction.

Figure 4-18 shows the reconstructed Cherenkov angle distributions for HPD0. The distributions for the case with the filter in data and Monte Carlo are shown on the left, with the Gaussian fit to the distributions shown in blue. The equivalent distributions for the no filter case are shown on the right. The 'chromatic tail' discussed in section 4.3.2 is clearly visible on the right hand side of the distribution when the filter is not present for both data and Monte Carlo. The distributions for the no filter case are

Figure 4-18: Reconstructed Cherenkov angle distributions for HPD0 in data with filter (top left), Monte Carlo with filter (bottom left), data without filter (top right) and Monte Carlo without filter (bottom right). Gaussian fits to the distributions are shown in blue. The enhanced 'chromatic tail' to the right of the peak is clearly visible in data and Monte Carlo in the no filter case.

fitted with a superposition of two Gaussians, one describing the central part of the distribution and the other describing the 'chromatic tail'. The mean and Gaussian width,σ, of these fits are summarised in Table 4.3.

A comparison between the reconstructed Cherenkov angle distributions in data and Monte Carlo are shown in Figure 4-19 on a logarithmic scale with and without the filter in place. These plots show a difference in the background distributions between data and Monte Carlo in both cases. The Monte Carlo simulation includes a description of Rayleigh scattering in the aerogel together with several other sources of background, such as Cherenkov photons produced in the N_2 which are reflected onto the HPDs from the filter or the aerogel, and similar reflections at the quartz entrance window and photocathode of the HPDs. It is clear however that there is a further contribution to the background in the data which is unaccounted for in the Monte Carlo. This badly modelled background in the data could be due to an additional scattering contribution in the aerogel, or possibly due to the backscattering effect which could have a distribution dependent on the signal photons. The increase in resolution from the filter

	Filter				**No filter**			
	Data		**Monte Carlo**		**Data**		**Monte Carlo**	
	θ_C (mrad)	σ (mrad)	θ_C (mrad)	σ (mrad)	θ_C (mrad)	σ (mrad)	θ_C (mrad)	σ (mrad)
HPD0	239.5	3.25	239.8	2.85	240.9	3.02	239.1	2.59
					(246.8)	(7.26)	(247.0)	(5.59)
HPD1	238.3	3.29	239.3	2.44	238.5	3.09	238.5	2.11
					(243.6)	(8.05)	(245.8)	(4.98)
HPD2	241.5	3.60	240.6	2.39	242.5	3.23	240.0	2.02
					(244.9)	(7.93)	(247.4)	(4.99)

Table 4.3: Mean Cherenkov angle and Gaussian width, σ, resulting from a Gaussian fit to the Cherenkov angle distributions for each of the three HPDs. The values in brackets in the no filter case are the mean and width of the 'chromatic tail' distribution.

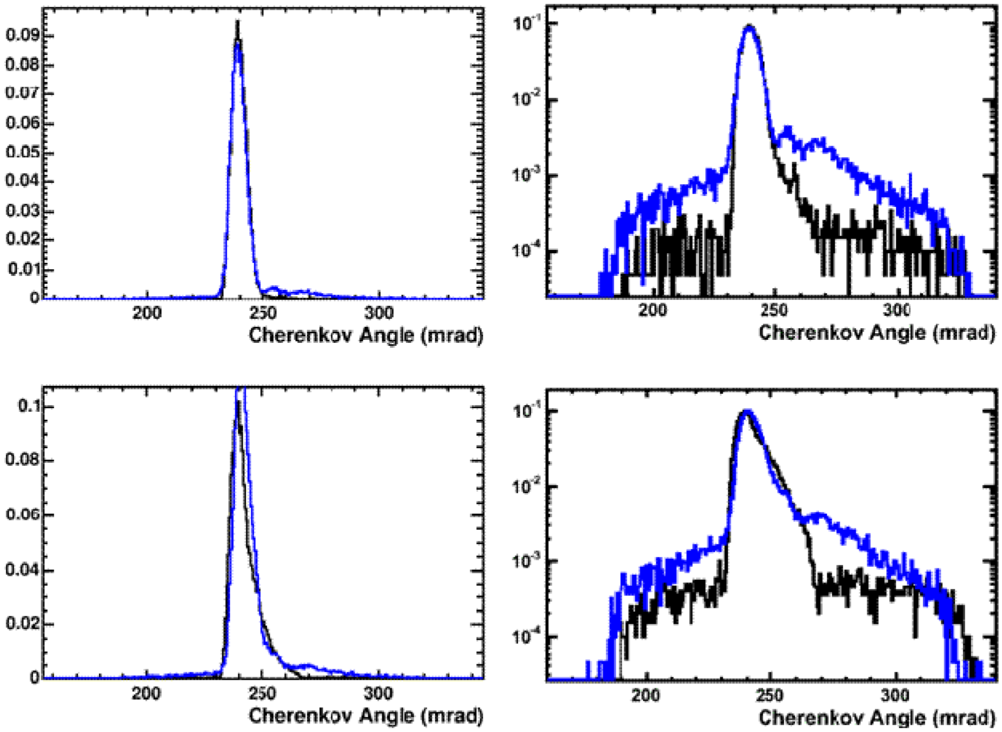

Figure 4-19: Cherenkov angle distribution in HPD0 for data (black) and Monte Carlo (blue), with filter (top) and without (bottom). The right hand plots show the distributions on a logarithmic scale.

case to the no filter case is also clearly seen in the figure.

4.3.8 Photoelectron Yield

The photoelectron yield is calculated for each HPD in data runs with and without filter. The values obtained from these runs are then compared with those obtained from the equivalent Monte Carlo simulation. In this section the Sellmeier relation, equation 4.5, is used to parameterise the aerogel refractive index in Monte Carlo.

In order to account for charge sharing a clustering algorithm is used to find hits in neighbouring pixels. With the high voltage at 18 kV and a detector bias of 80 V, the fraction of two pixel clusters found is 8.4 % (8.6 %), 14.7 % (14.8 %) and 9.4 % (9.6 %) in HPD0, HPD1 and HPD2 respectively for the case where the filter is present (removed). The fraction of clusters containing more than two pixels is negligible. All clusters are assumed to originate from a single photoelectron which results in an underestimation of the number of photoelectrons per event, as the probability of two photoelectrons striking neighbouring pixels is not zero. This underestimation can be corrected for as the Monte Carlo contains no description of charge sharing. In Monte Carlo it is found that a cluster due to two photoelectrons in neighbouring pixels occurs with a probability of approximately 1% both for the case with the filter and without.

The photoelectron yields are calculated using two different methods:

Method 1

A band is defined around the mean Cherenkov angle inside which photons are counted. In the filter case the band is defined by $(\theta_{\mathrm{Ckv}} - 3\sigma_{\mathrm{Ckv}}) < \theta < (\theta_{\mathrm{Ckv}} + 3\sigma_{\mathrm{Ckv}})$, where σ_{Ckv} is the Gaussian width of the fit to the θ_C distribution and θ_{Ckv} is the mean. In the no filter case this band is extended to include the chromatic tail of the distribution and is defined by $(\theta_{\mathrm{Ckv}} - 3\sigma_{\mathrm{Ckv}}) < \theta < (\theta_{\mathrm{Chr}} + 3\sigma_{\mathrm{Chr}})$, where σ_{Chr} is the width of the widest of the two fitted Gaussians and θ_{Chr} is its mean. An estimate of the background due to electronic noise and beam related background is made by considering a background run which was taken on beam spill using a random trigger. The aerogel was in place within the vessel, however a black screen was placed in front of the aerogel preventing Cherenkov photons produced in the aerogel from reaching the mirror. Hits within the defined band are counted and the mean number of background hits from these sources was found to be 0.012 hits per event across the three HPDs.

The distribution of background hits in the defined signal band is subtracted from the equivalent distribution in the data. Distributions showing the number of hits obtained for a data run with the filter in place after the subtraction of background, for HPD0 is shown in Figure 4-20.

The photoelectron yields calculated for data and Monte Carlo with and without filter present are summarised in Table 4.4. The comparison between data and Monte Carlo in the two cases shows that the agreement is good for HPD0 and HPD1 with a worse agreement in HPD2.

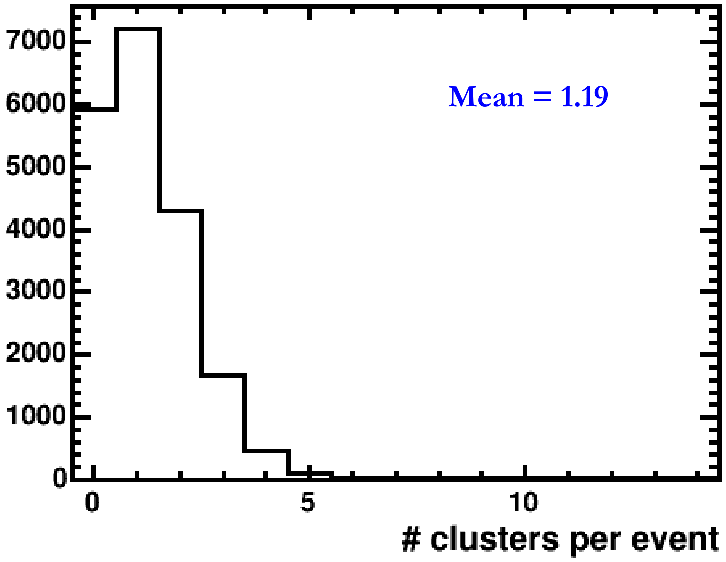

Figure 4-20: Number of hit per event in HPD0 with the filter in place.

Figure 4-21: Monte Carlo Cherenkov angle distributions in HPD1 where hits inside band region have been removed for Monte Carlo with filter in place. The background distribution before acceptance correction is shown on the left and the distribution after the correction is applied on the right.

Method 2

Although the agreement between the photon yield in data and Monte Carlo using method 1 is fairly good, Figure 4-19 shows that the background distributions in data and Monte Carlo are different. Indeed it is seen that the background in data has some other component that is not described by the Monte Carlo. For this reason a second analysis is performed where the contribution from the background distribution in the signal band is assessed separately so that a comparison of non-scattered signal photons in data and Monte Carlo is made.

The same 3σ band is used to define regions on the HPD, with all hits lying

HPD Number		**0**	**1**	**2**
Filter	**Data**	1.19 ± 0.01	1.00 ± 0.01	0.86 ± 0.01
	MC	1.22 ± 0.01	1.09 ± 0.01	1.21 ± 0.01
	Data/MC (%)	**98**	**92**	**71**
No Filter	**Data**	1.60 ± 0.01	1.41 ± 0.01	1.21 ± 0.01
	MC	1.62 ± 0.01	1.47 ± 0.01	1.59 ± 0.01
	Data/MC (%)	**99**	**96**	**76**

Table 4.4: Numbers given are mean of the Poisson fitted distribution of the number of hits within the defined signal region with statistical error.

outside this band considered as background. By selecting only these hits that lie outside the defined band, the background distribution can be considered alone. The background distribution for HPD1 in Monte Carlo with the filter in place is shown on the left in Figure 4-21. The sharp peak is part of the chromatic tail of the Cherenkov distribution that has been discussed previously. The Monte Carlo simulation contains a description of Rayleigh scattering in the aerogel which is expected to result in a background distribution with a $\cos^2\theta$ shape peaked around 242 mrad. The efficiency for detecting photons is dependent on θ_C as there are more pixels available to detect mid-range Cherenkov angles. A correction can be made which takes into account the variation of efficiency with θ_C. Figure 4-22 shows the distribution of θ_C reconstructed for all pixels lying within the image of the photocathode. The distribution is normalised so that mid-range θ_C has unit efficiency. The background distribution shown on the left in Figure 4-21 is divided by the

Figure 4-22: Normalised acceptance distribution as a function of Cherenkov angle in HPD0 distribution in Figure 4-22 resulting in a corrected background distribution which is shown on the right in Figure 4-21.

A contribution to the background is again estimated from the background run where the aerogel is in place and a black screen blocks signal photons. The Cherenkov angle is reconstructed for each hit within the signal band for the run and the resulting distribution is normalised to the number of events. The normalised, acceptance corrected distribution for HPD0 is shown in Figure 4-23. The equivalent distribution for each HPD is subtracted from the normalised θ_C distribution for the data run being studied.

The background distribution for HPD0 in data run where the filter is in place, containing hits lying outside the signal band after the background subtraction has been made is shown in figure Figure 4-24. The peak due to the chromatic tail of the

Figure 4-23: Background distribution for HPD0 calculated from background run with aerogel in place and black screen blocking signal photons.

Figure 4-24: Normalised Cherenkov angle distribution of hits lying outside the defined band for data run 16, after subtraction of background estimate.

Cherenkov angle distribution can again be seen to the right of the band however the distribution has a very different shape from that seen in Monte Carlo. The Gaussian fit to this distribution is shown in the figure. When fitting only the left hand side of the distribution is used so that the presence of the chromatic tail does not bias the fit.

The background distributions are fitted in data and Monte Carlo. A single Gaussian is used to fit the distribution in data and a straight line in Monte Carlo. In both cases the left hand side of the distribution alone is used to make the fit in order that the presence of the chromatic tail on the right does not bias the fit. The contribution from the background within the signal band is calculated from the fit and subtracted from the total number of photons in the signal band giving the number of non-scattered photons within the band. In addition to this the total number of hits outside the band region is also counted. The yields obtained for data with and without filter and equivalent expected values calculated using Monte Carlo simulations are summarised in Table 4.5.

The ratio between the number of signal photoelectrons found in the defined band in data and Monte Carlo is calculated for the filter and the no filter case. As seen using the first method the agreement between data and Monte Carlo is reasonable for HPD0 and HPD1, but poor for HPD2.

A loss in photoelectron yield of 27% is seen across the three HPDs as a result of using the filter. In considering the use of aerogel in LHCb itself, the impact of this loss must be balanced with the improved resolution on the Cherenkov angle measurement when deciding whether or not the inclusion of a filter is beneficial.

			0	**1**	**2**
Filter	**Total in 3σ**	**Data**	1.19 ± 0.01	1.00 ± 0.01	0.86 ± 0.01
		MC	1.22 ± 0.01	1.09 ± 0.01	1.21 ± 0.01
	Background in 3σ	**Data**	0.058 ± 0.00	0.069 ± 0.00	0.072 ± 0.00
		MC	0.005 ± 0.00	0.004 ± 0.00	0.004 ± 0.00
	Signal in 3σ	**Data**	1.13 ± 0.01	0.93 ± 0.01	0.79 ± 0.00
		MC	1.22 ± 0.01	1.09 ± 0.01	1.21 ± 0.01
		Data/MC (%)	**93**	**85**	**65**
	Background outside 3σ	**Data**	0.252 ± 0.01	0.222 ± 0.00	0.123 ± 0.00
		MC	0.060 ± 0.00	0.057 ± 0.00	0.063 ± 0.00
No Filter	**Total in 3σ**	**Data**	1.59 ± 0.01	1.41 ± 0.01	1.22 ± 0.01
		MC	1.64 ± 0.01	1.47 ± 0.01	1.60 ± 0.01
	Background in 3σ	**Data**	0.133 ± 0.00	0.101 ± 0.00	0.115 ± 0.00
		MC	0.019 ± 0.00	0.015 ± 0.00	0.017 ± 0.00
	Signal in 3σ	**Data**	1.46 ±0.01	1.31 ± 0.01	1.10 ± 0.01
		MC	1.62 ± 0.01	1.45 ± 0.01	1.59 ± 0.01
		Data/MC (%)	**90**	**90**	**69**
	Background outside 3σ	**Data**	0.400 ± 0.00	0.322 ± 0.00	0.206 ± 0.00
		MC	0.292 ± 0.00	0.314 ± 0.00	0.369 ± 0.00

Table 4.5: Summary of the photoelectron yields found using method 2.

4.3.9 Alternative Monte Carlo description

As discussed in section 4.3.6 the Monte Carlo calculation has been made using two possible parameterisations of the aerogel refractive index. Photoelectron yields have also been calculated using the Claussius-Mossotti equation, equation 4.6, and the results are summarised in Table 4.6. The photoelectron yields calculated using method 1 and the Claussius-Mossotti description of the aerogel refractive index vary only a little from those calculated using the Sellmeir description. The error on the calculated yield in Monte Carlo due to uncertainty on the refractive index of the aerogel is estimated to be ~2%.

HPD Number	Claussius-Mossotti	Sellmeier	Data
0	1.20	1.22	1.19
1	1.08	1.09	1.00
2	1.18	1.21	0.86

Table 4.6: Photoelectron yields calculated in Monte Carlo where two different parameterisations of the aerogel refractive index are used. These yields can be compared to those found in data.

4.3.10 High Voltage Scan

During the beam tests a scan of the HPD high voltage was made with the filter removed. The photoelectron yield is calculated for each run in the scan and the results, using the first method, are shown in Figure 4-25. This can be compared to the high voltage scan carried out during the HPD beam tests. It can be seen that the photoelectron yield increases slowly as the high voltage increases from 14 to 20 kV. This can be compared to the same scan made during the HPD beam tests shown in Figure 4-8. In the range 14-20 kV the efficiency is increasing due to the increased probability of detecting back-scattered photoelectrons.

Figure 4-25: Photoelectron yield calculated for each HPD for the steps in a high voltage scan. The data are taken without filter.

4.4 Conclusions

The results from both beam test show that the prototype HPDs perform well in beam conditions. The agreement between the photoelectron yield found in data taken in the aerogel beam tests and a Monte Carlo simulation is reasonable. The differences between data and Monte Carlo are ~ 10-15 % in HPD0 and HPD1, with a larger discrepancy of ~ 30 % in HPD2. As mentioned in 4.3.3 runs were taken where the aerogel was removed and the nitrogen in the vessel was used as the Cherenkov radiator. The photoelectron yield was again calculated and the same discrepancy between data and Monte Carlo was seen for HPD2 [cal05]. The large difference is attributed to the description of the quantum efficiency used for HPD2 which is thought to be less accurate than the descriptions for HPD0 and HPD1.

Chapter 5

Search for $B_d^0 \to K^+K^-$ and $B_s^0 \to \pi^+\pi^-$ events at LHCb

5.1 Introduction

As discussed in Chapter 1, the channels $B_d^0 \to K^+K^-$ and $B_s^0 \to \pi^+\pi^-$ may be used to determine the angle γ. As these decays may only proceed via penguin annihilation and exchange processes, which are amongst the contributions to $B_d^0 \to \pi^+\pi^-$, these channels most interestingly provide information on the importance of these amplitudes in this benchmark decay.

In this chapter a simulation study is used to investigate the possibility of observing $B_d^0 \to K^+K^-$ and $B_s^0 \to \pi^+\pi^-$ at LHCb for given assumptions about their branching ratios. In the final part of the chapter a simple simulation is used to investigate how well the CP asymmetry could be measured for $B_d^0 \to K^+K^-$.

5.2 Selection of $B_d^0 \to K^+K^-$ and $B_s^0 \to \pi^+\pi^-$ events

5.2.1 Event Generation

Monte Carlo data samples have been produced and passed through the detector simulation, digitisation and reconstruction chain as described in section 2.5. The event generator uses the production processes shown in Figure 2-2. Samples of signal events have been generated, each containing at least one $B_d^0 \to K^+K^- (B_s^0 \to \pi^+\pi^-)$ or $\overline{B}_d^0 \to K^+K^- (\overline{B}_s^0 \to \pi^+\pi^-)$ decay. The signal $B_{d,s}^0$ is required to be produced with a polar angle smaller than 400 mrad, so that the decay products are likely to fall within the detector acceptance. This requirement corresponds to a geometrical efficiency of 34.7% [lhcb03].

The LHCb trigger is expected to heavily suppress events that do not contain a b-hadron. With the trigger scheme assumed at the time of the study, the make-up of the events is assumed to be 0.15:0.15:0.60 ($b\overline{b}:c\overline{c}:q\overline{q}$, where q = u,d,s) [lhcbt03][11]. Although the $b\overline{b}$ are not the dominant component of this sample, they are expected to be much more resistive to specific event selection cuts than the other categories. It is assumed that any cut which is demonstrated to be effective in reducing $b\overline{b}$ background will have much higher suppression in rejecting the residual events from non-$b\overline{b}$ events. Thus the background rejection performance of the offline cuts is best studied with generic $b\overline{b}$ events. Therefore an estimate of the amount of combinatorial background from interactions not containing a signal decay which will pass the selection cuts is made by studying a sample of 4.3×10^6 inclusive $b\overline{b}$ events[12]. For this sample a geometrical cut is made requiring that at least one of the b-hadrons is in the forward direction and has a polar angle within 400 mrad. This corresponds to a geometrical efficiency of 43.2% [lhcb03] which is larger than the efficiency for signal $B^0_{d,s}$ as in this case either b-hadron can satisfy the requirement. The statistical uncertainty on the efficiencies for signal B events and for inclusive $b\overline{b}$ events are small [sch05].

---

[11] Recent improvements to this trigger strategy have changed these numbers to 0.4:0.25:0.25[teu05].

[12] In fact, 15% more events were processed, but some events were duplicated due to a random seed bug.

b-hadron	Production Fraction (%)
B_d^0	39.1±0.13
B_s^0	10.0±0.13
Λ_b^0	11.8±0.21

Table 5.1: Probability of hadronisation for each of the hadrons of interest in this analysis. Numbers taken from [eid04].

The hadronisation fractions, or the probability that a b-quark results in the weakly decaying hadron of interest, are given in Table 5.1. Specific backgrounds of decays that are topologically similar to $B_d^0 \rightarrow K^+K^-$ and $B_s^0 \rightarrow \pi^+\pi^-$ are also studied in this analysis. The sizes of the samples used in this study are given in Table 1.1, along with the assumed branching ratio of each decay. In the case of a misidentification of one decay product, these topologically similar decays can survive the selection cuts. The importance of the RICH detectors to provide particle identification can be demonstrated clearly by the consideration of these backgrounds. The excellent mass

Figure 5-1: Schematic of the $B_d^0 \rightarrow K^+K^-$ decay showing the geometrical parameters used in event selection resolution of LHCb means that three-body (and higher) b-decays are not a background to the two-body signal. Previous studies [vag03] have examined the make-up of the combinatoric background in the B→hhh analysis and found it to be from random mis-associations of tracks from different decaying b-hadrons, or tracks from one b-hadron and one badly reconstructed track.

The simulation does not include the effects of the magnetic field in the RICH. However, this effect has been shown to be negligible in dedicated studies [lhcb03]. These studies were performed after the sample used in this study was generated and they have also found that other effects, for example delta rays in the aerogel, are not dominant.

The current upper limit $BR(B_d^0 \to K^+K^-) < 0.6\times10^{-6}$ [bab02] is consistent with the estimated branching ratio used here. No upper limit has yet been placed on $BR(B_s^0 \to \pi^+\pi^-)$. Conservative estimates of the branching ratios for the decays $\Lambda_b^0 \to p\pi^-$ and $\Lambda_b^0 \to pK^-$ are used. It should however be noted that the current upper limit from CDF on the total branching ratio is $BR(\Lambda_b^0 \to p\pi^-, pK^-) \leq 22\times10^{-6}$ [cdf04] at the 90% confidence level. In addition to the experimental upper limit, theoretical calculations predict branching ratios $BR(\Lambda_b^0 \to p\pi^-) = (0.8-1.2)\times10^{-6}$ and $BR(\Lambda_b^0 \to pK^-) \approx (1.4-1.9)\times10^{-6}$ [moh01]. These limits indicate that these decays will have a smaller contribution to the background than is estimated here. The decays $B_d \to p\overline{p}$ and $B_s \to p\overline{p}$ have not been considered in this analysis. Both are heavily suppressed, and will be easily rejected by the RICH.

5.2.2 Event Selection

A schematic representation of the event to be reconstructed is shown in Figure 5-1. The $B^0_{d,s} \to h^+h^-$ selection program [vag03] written for the LHCb analysis package, DaVinci [lhcb05] is used to select $B^0_{d,s}$ mesons decaying to two charged kaons or pions. Candidate $B^0_{d,s}$ mesons are selected by employing a number of cuts that exploit the nature of the decay. Pairs of oppositely charged tracks that are found to form a vertex must have momentum larger than p_{min} and lower than p_{max}. The lower cut on momentum excludes the region where there is a high background from 'ghost' tracks. The higher cut on momentum represents the upper limit of the RICH system in terms of good separation of pions and kaons. The track pairs must also have high transverse momentum, p_T, in order to exploit the high rest mass of the $B^0_{d,s}$. These tracks are also required to be inconsistent with having come from the primary vertex and therefore are required to have a high impact parameter significance. The impact parameter of each kaon is marked IP in Figure 5-1 and is defined as the distance of closest approach between the particle trajectory and the primary vertex, where the particle track is extrapolated back towards the primary vertex. The impact parameter significance is defined as IP/σ_{IP} where σ_{IP} is the error on the measurement of the impact parameter. The impact parameter significance for a kaon is typically greater than 6 whereas for a $B^0_{d,s}$, which is required to be consistent with having come from the primary vertex, it is typically below 3. The impact parameter of the candidate $B^0_{d,s}$ is also marked in Figure 5-1 as IP_B. The lifetime of the $B^0_{d,s}$ is further exploited by requiring a minimum separation between the primary and secondary vertices. A requirement is also placed on the minimum p_T of the candidate $B^0_{d,s}$ in order to exploit the hard fragmentation of b quarks. In summary, each charged track is required to have:

- $p_{min} < p < p_{max}$;
- p_T larger than $(p_T)_{min}$;
- IP/σ_{IP} larger than $(IP/\sigma_{IP})_{min}$.

Pairs of tracks having opposite charge are made for which it is required that:

- at least one of the pair should have p_T larger than $(p_T)_{one}$;
- at least one of the pair should also have IP/σ_{IP} larger than $(IP/\sigma_{IP})_{one}$.

Pairs fulfilling these requirements are fitted to a common vertex and are used to form a candidate $B^0_{d,s}$ for which the following requirements must be satisfied:

- the χ^2 of the vertex fit must be smaller than χ^2_{max};
- the p_T of the candidate $B^0_{d,s}$ must be greater than $(p^B_T)_{min}$;
- an impact parameter significance less than $(IP_B/\sigma_{IP_B})_{max}$;
- distance of flight, normalised by the measurement uncertainty, greater than $(L/\sigma_L)_{min}$ from the primary vertex ;
- an invariant mass within $\pm^{hi}_{lo}$ of the nominal $B^0_{d,s}$ mass.

These criteria are exploited in two stages: an initial pre-selection; and a final set of cuts to maximise the signal significance.

	Pre-selection cuts	**Tight selection cuts**
p_{min} (GeV/c)	0.5	2.5
p_{max} (GeV/c)	100	100
$(p_T)_{min}$ (GeV/c)	0.4	1.2
$(p_T)_{one}$ (GeV/c)	0.5	3.2
$(IP/\sigma_{IP})_{min}$	1.5	6
$(IP/\sigma_{IP})_{one}$	1.5	12
χ^2_{max}	20	4
$(p_T^B)_{min}$ (GeV/c)	0.4	1.6
$(IP_B/\sigma_{IP_B})_{max}$	10	2.25
$(L/\sigma_L)_{min}$	2	19

Table 5.2: Selection cuts used in selection of $B_d^0 \rightarrow K^+K^-$ and $B_s^0 \rightarrow \pi^+\pi^-$. Mass and particle identification cuts are not included.

Pre-selection and N-tuple creation

Using DaVinci and the $B_{d,s}^0 \rightarrow h^+h^-$ selection package an initial selection of events is made, filtering the full sample using the pre-selection cut values given in Table 5.2. A ROOT N-tuple [bru96] is created in which to store information for all $B_{d,s}^0$ candidates that pass the pre-selection. For each $B_{d,s}^0$ candidate the N-tuple entry contains

- the reconstructed primary vertex position;
- the impact parameter significance;
- the transverse momentum;

- the distance of flight;
- the momentum 3-vector;
- the position of the reconstructed secondary vertex;
- the χ^2 of the vertex fit.

In addition to this reconstructed information the Monte Carlo true primary and secondary vertex locations are stored. For each of the two charged tracks that have been reconstructed to give the $B^0_{d,s}$ candidate the N-tuple entry contains

- the momentum 3-vector.
- the impact parameter significance;
- the transverse momentum.

The invariant mass is not stored in the N-tuple, but calculated afterwards using the 3-vectors of the charged tracks, as this depends on which particle assignment has been made to the tracks, and is hence different for the $B^0_d \to K^+K^-$ and $B^0_s \to \pi^+\pi^-$ analyses.

In addition to the information required for the selection cuts the outcome of the

Figure 5-2: Distributions of the selection variables. Background bb events shown by solid circles and $B_d \rightarrow K^+K^-$ shown by solid line. Plots are obtained after pre-selection and in the mass window 5.0 – 5.5 GeV/c^2, but before trigger and selection cuts are applied. Final cut values are shown by dotted blue lines. The meaning of each cut is explained in the text. The invariant mass cut is chosen to be asymmetric and the reasons for this choice are outlined in section 5.2.4. The scale is arbitrary.

Level-0 and Level-1 trigger decision for each event is retained. In order for particle identification requirements which are not imposed in the pre-selection to be applied later, the log-likelihood value for each of the five particle hypotheses are stored. Finally the true particle type of each charged track is stored.

Selection cut values

The values of the tight cuts have been optimised for selection of $B_d^0 \rightarrow \pi^+\pi^-$ [vag03]. The same cut values are used for the $B_d^0 \rightarrow K^+K^-$ and $B_s^0 \rightarrow \pi^+\pi^-$ selections, the values for which are given in Table 5.2. In this study limits are placed on the background in order to show the potential for observing $B_d^0 \rightarrow K^+K^-$ and $B_s^0 \rightarrow \pi^+\pi^-$ decays. The distributions of the key selection variables for the $B_d^0 \rightarrow K^+K^-$ selection are seen in Figure 5-2 for both signal and the $b\bar{b}$ background events. The difference in the shape of the signal and background distributions is exploited by the cuts. The cut values are indicated by blue dotted lines for each distribution and the plot vertical scales are arbitrary.

Figure 5-3: Reconstructed invariant mass for $B_d^0 \rightarrow K^+K^-$ (left) and $B_s^0 \rightarrow \pi^+\pi^-$ (right) prior to the use of RICH information. The signal is completely obscured by the contribution from the two-body backgrounds in both cases.

5.2.3 Particle Identification

In addition to the selection cuts outlined above, a requirement on the particle identification results is also used, which is based on information from the RICH system. As described in 2.3.6 a likelihood is constructed for each track for each particle hypothesis. A cut is placed on the difference in log-likelihood between two hypotheses

$$\Delta \ln \mathcal{L}_{\mathrm{ij}} = \ln \mathcal{L}(\mathrm{i}) - \ln \mathcal{L}(\mathrm{j}) \, ,$$

for example

$$\Delta \ln \mathcal{L}_{\mathrm{K}\pi} = \ln \mathcal{L}(\mathrm{K}) - \ln \mathcal{L}(\pi) \, ,$$

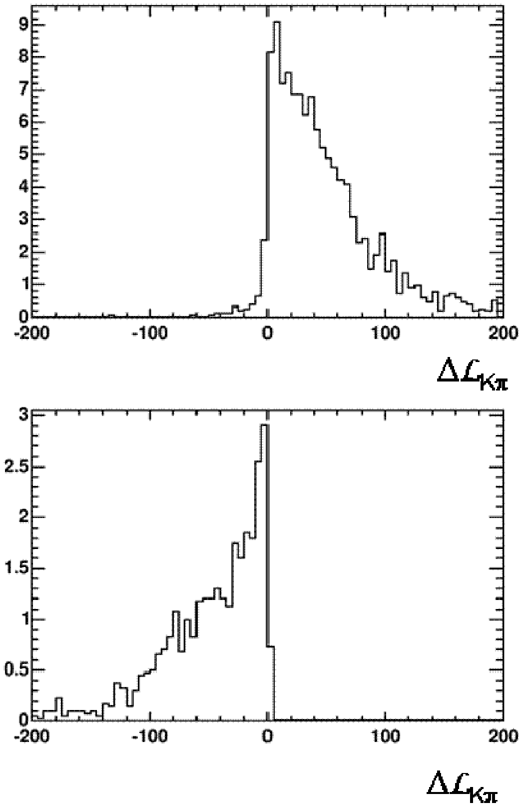

Figure 5-4: Distribution of $\Delta\mathcal{L}_{K\pi}$ for true kaons in $B_d \to K^+K^-$ decays (top) and for true pions in $B_s \to \pi^+\pi^-$ decays (bottom)

which tends to be positive for true kaons and negative for true pions. The distribution of $\Delta\ln\mathcal{L}_{K\pi}$ for true kaons and pions are shown in Figure 5-4.

For the $B_d \rightarrow K^+K^-$ selection only tracks having good separation between the kaon and pion hypothesis are selected using the requirement $\Delta\ln\mathcal{L}_{K\pi} > 2$. In order to reduce background from the two-body decays of Λ_b which have a proton in the final state, $\Delta\ln\mathcal{L}_{Kp} > -2$ is also demanded. The left hand plot in Figure 5-3 shows the reconstructed invariant mass for $B_d^0 \rightarrow K^+K^-$ prior to the use of any RICH information. The signal is submerged under the background from the other two-body decay modes. The top right hand plot in Figure 5-5 shows the result of applying particle

Figure 5-5: The invariant mass plots of events surviving the particle identification cuts are shown on the left for $B_d^0 \rightarrow K^+K^-$ (top) and $B_s^0 \rightarrow \pi^+\pi^-$ (bottom). The signal peaks are already visible above the background. On the right the same plot shows the situation after a tight mass cut is applied. The two-body background is reduced to a minimum.

identification requirements. The peak due to signal events becomes visible above the background.

For the $B_s^0 \rightarrow \pi^+\pi^-$ selection, in order to select pions, only tracks with $\Delta\mathcal{L}_{K\pi} < 2$ are selected. It can be seen again on the right of Figure 5-3 that before the particle identification requirement is imposed the signal is swamped beneath the background. In the bottom left plot in Figure 5-5 the effect of imposing the particle identification is seen and the signal peak is visible above the background.

5.2.4 Tight mass cut

A single Gaussian is fitted to the invariant mass distributions for both decay channels as shown in Figure 5-6 in the absence of background. The Gaussian distributions have width 16.5 ± 0.7 MeV/c^2. The good mass resolution of LHCb means that a tight mass cut can be applied which will further reduce the two body background seen on the left in Figure 5-5. For $B_d^0 \rightarrow K^+K^-$ the dominant background source is from $B_d^0 \rightarrow K^+\pi^-$ decays which lie at higher masses. It is therefore sensible to

Figure 5-6: Invariant mass distribution of selected B candidates for $B_d^0 \rightarrow K^+K^-$ (left) and $B_s^0 \rightarrow \pi^+\pi^-$ (right). Gaussian fits to the distributions have width, σ = 16.5 ± 0.7 MeV/c^2.

apply an asymmetric tight mass window. A mass cut is introduced where the reconstructed mass of the B_d^0 is required to be within the range $(m_{B_d^0} - 0.06) < m_{reconstructed} < (m_{B_d^0} + 0.01)$ measured in GeV/c^2. The result of applying this cut is seen on the top right of Figure 5-5.

For $B_s^0 \to \pi^+\pi^-$ the major backgrounds lie at significantly lower masses and a symmetric mass cut can be applied. Candidate B_s^0 are selected so that the mass of the selected events are in the range $m = m_{B_s^0} \pm 0.05$ GeV/c^2. The effect of imposing this cut can be seen in the bottom right of Figure 5-5.

Figure 5-7: Distribution of signal events for both channels in proper time. B candidates from $B_d^0 \rightarrow K^+K^-$ after pre-selection, trigger, lifetime, particle identification and mass cuts. Fitted with equation 5.1 resulting in α = 103 (±19), τ = 1.47 (±0.09) ps and μ = 1.51 (±0.14). The generator value for the lifetime is 1.532 ps

5.2.5 Results

Characteristics of the selected signal

When reconstructing $B_d^0 \rightarrow K^+K^-$ and $B_s^0 \rightarrow \pi^+\pi^-$, rejection of backgrounds with the same topology would not be possible without the particle identification performance of the RICH and good invariant mass resolution.

The distribution of signal events in proper time is shown in Figure 5-7. This distribution shows the expected exponential fall-off with proper time with an inefficiency at low proper times caused by the trigger and offline cuts. The distribution contains candidate B mesons from $B_d^0 \rightarrow K^+K^-$ after the trigger, impact parameter and distance of flight cuts on the B candidate, particle identification and tight mass cut. This distribution is fitted with the empirical form

$$y = \alpha\left(e^{-\frac{t}{\tau}} \times \frac{(\mu t)^3}{1+(\mu t)^3} \right) \qquad 5.1$$

Mass Resolution (MeV/c²)	16.5 ± 0.7
Primary Vertex Resolution (z) (μm)	40 ± 2
Secondary Vertex Resolution (z) (μm)	125 ± 5
Proper Time Resolution (fs)	37 ± 2

Table 5.3: Summary of the resolutions for the two decay channels.

Figure 5-8: Plots showing the resolution on the primary and secondary vertices (in z) and proper time. Distributions are fitted with a Gaussian and have widths σ=40μm, σ=125μm and 37 fs respectively.

where α, τ and μ are parameters to be fitted. The exponential factor describes the lifetime of the B and τ is the mean lifetime. The second factor within the brackets is a parameterisation of the combined efficiency of the selection and the trigger. The term accounts for the inefficiency in detecting signal events at low proper times seen

		Pre-selection	Trigger	Selection cuts	PID	Tight mass cut	Total
$B_d^0 \rightarrow K^+K^-$	**Efficiency(%)**	7.3	31.6	35.8	84.1	71.9	0.4
	Purity(%)	1.4	1.4	1.4	7.2	82.4	-
$B_s^0 \rightarrow \pi^+\pi^-$	**Efficiency(%)**	7.1	32.9	37.3	92.9	89.5	0.7
	Purity(%)	1.4	1.4	1.4	8.2	96.4	-

Table 5.4: Efficiency and purity of each stage of both selections. Purity=S/(S+B) and efficiency is measured relative to the previous stage. Numbers are corrected for the geometrical acceptance. PID stands for Particle Identification.

in Figure 5-7. Its form is entirely empirical and has been used for other studies on LHCb [lhcb03]. It can be seen to describe the data well.

The resolutions on the primary and secondary vertices for $B_d^0 \rightarrow K^+K^-$ decays are shown in Figure 5-8 along with the proper time resolution. All distributions have been fitted with a single Gaussian. A good proper time resolution is necessary for measuring CP asymmetries, particularly important in the case of the fast oscillating B_s^0.

	Events surviving trigger & pre-selection	Events surviving selection cuts – no PID	Events surviving PID cut	Events surviving tight mass cut
$B_d^0 \rightarrow K^+K^-$	8652	3094	2602	1872
$B_d^0 \rightarrow K^+\pi^-$	337742	123650	3097	261
$B_d^0 \rightarrow \pi^+\pi^-$	84239	31302	24	0
$B_s^0 \rightarrow K^+K^-$	98609	34068	29324	108
$B_s^0 \rightarrow \pi^+K^-$	24662	9179	480	0
$B_s^0 \rightarrow \pi^+\pi^-$	8063	3076	0	0
$\Lambda_b \rightarrow pK^-$	50611	14232	514	30
$\Lambda_b \rightarrow p\pi^-$	9175	2130	0	0

Table 5.5: Estimated annual yield of events passing each stage of the $B_d^0 \rightarrow K^+K^-$ selection.

The oscillation period of the B_s^0 is $\frac{2\pi}{\Delta m_s}$ which is 433 fs. The proper time resolution must be much better than this in order to be sensitive to the oscillations. A proper time resolution of 40 fs would be good enough to achieve this. All resolutions for $B_d^0 \to K^+K^-$ and $B_s^0 \to \pi^+\pi^-$ are summarised in Table 5.3.

Results of selection

The efficiencies and purities for both channels at each stage of the selection are given in Table 5.4. The efficiencies are given relative to the previous stage and the pre-selection efficiency is calculated using the sample size corrected for the geometrical efficiency discussed in 5.2.1. Purity is defined as $S/(S+B)$ where S is the number of signal events and B is the number of two-body background events.

The annual yields of each stage of the $B_d^0 \to K^+K^-$ selection are given in Table 5.5. An annual signal yield of 1872 events is expected with contamination from 399 background events from other two-body decays. Table 5.6 gives the equivalent yields for the $B_s^0 \to \pi^+\pi^-$ selection. Here an annual signal yield of 2682 events is expected with contamination from 634 events from two-body backgrounds. The annual signal yield, S, is calculated using the following relation:

$$S = L_{int} \times \sigma_{b\bar{b}} \times 2 \times f_B \times BR \times \varepsilon \qquad 5.2$$

	Events surviving trigger & pre-selection	**Events surviving selection cuts – no PID**	**Events surviving PID cut**	**Events surviving tight mass cut**
$B_s^0 \to \pi^+\pi^-$	8665	3228	2998	2682
$B_d^0 \to K^+\pi^-$	296780	112050	5653	101
$B_d^0 \to \pi^+\pi^-$	75815	28615	26708	138
$B_d^0 \to K^+K^-$	7522	2785	3	0
$B_s^0 \to K^+K^-$	86109	30756	194	0
$B_s^0 \to \pi^+K^-$	23263	8600	500	144
$\Lambda_b \to pK^-$	83547	28776	163	54
$\Lambda_b \to p\pi^-$	14533	5125	543	197

Table 5.6: Estimated annual yield of events passing each stage of $B_s^0 \to \pi^+\pi^-$ selection .

where $L_{int} = 2\ fb^{-1}$ and is the nominal annual integrated luminosity and $\sigma_{b\bar{b}}$ is the $b\bar{b}$ production cross section which is estimated to be 500 μb [lhcb03]. The factor 2 takes into account the fact that either quark can hadronise with the hadronization probabilities, f_B, which are given in Table 5.1. The branching ratios, BR, are given in Table 1.1. Finally ε, the efficiency of the selection is calculated using the following expression:

$$\varepsilon = \frac{n_{pass}}{s/f_{eff}} \qquad 5.3$$

where n_{pass} is the number of events passing the selection cuts, s is the size of the sample which is given in Table 1.1. The factor f_{eff} takes into account the efficiency of the requirement imposed at generation of the event samples that the signal meson should be produced within 400 mrad which for signal B events is 0.347.

5.2.6 Reduced branching ratios

The results given so far have assumed that the branching ratio of $\mathrm{B_d^0 \to K^+K^-}$, $\mathrm{BR(B_d^0 \to K^+K^-)}$ to be one tenth of $\mathrm{BR(B_d^0 \to \pi^+\pi^-)}$. If $\mathrm{BR(B_d^0 \to K^+K^-)}$ were in fact one hundredth of $\mathrm{BR(B_d^0 \to \pi^+\pi^-)}$ using the cut values given in Table 5.2, a purity of only 32% would be achieved. In this scenario the purity of the selection can be improved by tightening the particle identification requirements. If the requirements placed on the kaon identification are tightened to $\Delta\mathcal{L}_{K\pi} > 10$ and $\Delta\mathcal{L}_{Kp} > -1$, further reducing the pion and proton contamination of the signal, the purity of the selection after the tight mass increases to 40.9%. Table 5.7 gives efficiencies and purities for this selection with reduced branching ratio and these tightened particle identification requirements. The number of events passing each stage of the selection are given in Table 5.8. In this case the expected annula signal yield is 148 with contamination from 214 two-body background events. Although an observation would be more difficult, by using tighter particle identification requirements it can be seen that the contamination from two-body backgrounds can be significantly reduced.

		Pre-selection	**Trigger**	**Selection Cuts**	**PID**	**Tight Mass Cut**	**Total**
$\mathrm{B_d^0 \to K^+K^-}$	**Efficiency (%)**	7.3	31.6	35.8	65.4	73.3	0.40
	Purity (%)	0.1	0.1	0.1	0.9	40.9	-
$\mathrm{B_s^0 \to \pi^+\pi^-}$	**Efficiency (%)**	7.1	32.9	37.3	44.7	90.3	0.35
	Purity (%)	0.1	0.1	0.1	1.1	47.5	-

Table 5.7: Efficiencies and purities for each stage of the selection. Reduced branching ratios and tightened particle identification requirements are used.

	Events surviving pre-selection	**Events surviving cuts – no PID**	**Events surviving PID requirement**	**Events surviving tight mass cut**
$B_s^0 \to \pi^+\pi^-$	866	323	144	130
$B_d^0 \to K^+\pi^-$	296780	112050	303	34
$B_d^0 \to \pi^+\pi^-$	75815	28615	13189	83
$B_d^0 \to K^+K^-$	7522	2785	0	0
$B_s^0 \to K^+K^-$	86109	30756	0	0
$B_s^0 \to \pi^+K^-$	23263	8600	39	0
$\Lambda_b \to pK^-$	83547	28776	0	0
$\Lambda_b \to p\pi^-$	14533	5125	48	27

Table 5.9: Expected annual yield passing selection cuts with $BR(B_S^0 \to \pi^+\pi^-) = 0.01 \times BR(B_S^0 \to K^+K^-)$. Numbers are evaluated in mass window 5.0 – 5.5 GeV/c². The tight mass window covers the range $m_{\text{reconstructed}} = m_{B_s^0} \pm 0.5$ GeV/c² measured in GeV/c²

	Events surviving pre-selection	**Events surviving cuts – no PID**	**Events surviving PID requirement**	**Events surviving tight mass cut**
$B_d^0 \to K^+K^-$	865	309	202	148
$B_d^0 \to K^+\pi^-$	337742	123650	672	112
$B_d^0 \to \pi^+\pi^-$	84239	31302	0	0
$B_s^0 \to K^+K^-$	98609	34068	22173	72
$B_s^0 \to \pi^+K^-$	24662	9197	92	0
$B_s^0 \to \pi^+\pi^-$	8063	3076	0	0
$\Lambda_b \to pK^-$	50611	14232	393	30
$\Lambda_b \to p\pi^-$	9175	2130	0	0

Table 5.8: Expected annual yields passing selection cuts with $BR(B_d^0 \to K^+K^-) = 0.01 \times BR(B_d^0 \to \pi^+\pi^-)$ and tightened particles identification requirements $\Delta L_{K\pi} > 10$, $\Delta L_{Kp} > -1$.

The branching ratio of $B_s^0 \to \pi^+\pi^-$ has also been assumed to be one tenth of the $B_s^0 \to K^+K^-$ branching ratio. If this assumption is changed to a more pessimistic one hundredth, the purity of the selection with the same cuts is reduced to 6.8%. As was shown for $B_d^0 \to K^+K^-$, the purity can be improved by introducing tighter particle identification requirements. Placing a tighter requirement on the identification of the pion and requiring $\Delta\mathcal{L}_{K\pi} > -20$, the purity of the selection after the tight mass cut is increased to 47.5%. The efficiencies and purities of each selection stage are given in Table 5.7. Table 5.9 gives the numbers of events passing each stage of the selection. Again in this case it is clear that making an observation would be more difficult; it is also seen that with tighter particle identification requirements the two-body background contribution is significantly reduced. The possibility of making an observation would rely on LHCb providing the required mass resolution, as a poorer resolution would lead to further contamination of the signal by these backgrounds.

5.2.7 Combinatorial Background

In order to estimate the contribution from combinatorial background the selection cuts have been applied to a sample of 4.3×10^6 inclusive $b\bar{b}$ events. The pre-selection is first run on the sample of $b\bar{b}$ events. In order to extract maximum information from the available statistics, in the following discussion the basic selection cuts of Table 5.2, the tight mass cuts and the PID cuts are applied independently, and are assumed to be uncorrelated.

Having applied the selection cuts, excluding the particle identification and invariant mass cuts, to the $b\overline{b}$ sample the number of events passing these cuts, n, is found. Knowing n, it is possible to place an upper limit the number of events expected to pass the cuts in a sample of this size to a certain confidence limit. The upper limit, x_{up}, on the true mean number of events, θ, is found such that the probability of θ exceeding x_{up} is 10 % (see Appendix B for further details). Selecting kaons for $B_d^0 \to K^+K^-$ from the full $b\overline{b}$ sample it is found that 4 events pass the trigger and selection cuts in the mass range 5.0 – 5.5 GeV/c^2. Taking values from tables, x_{up}=7.99 with 90% confidence [eid04]. Selecting pions for $B_s^0 \to \pi^+\pi^-$ from the sample of inclusive $b\overline{b}$ events it is found that 6 events pass the trigger and selection cuts before particle identification and tight mass cut have been made. This gives x_{up}=10.53 with 90% confidence. The two-body decay modes are included in the $b\overline{b}$ sample. In order to conform that these background events are not double counted a check has been performed using the Monte Carlo truth information. The invariant mass of each of the background events passing the cuts was calculated using the true momentum of the particles. If the calculated invariant mass were exactly the B mass, this would indicate that the pair of particles came from a two body decay. This is not the case for any of the combinations, therefore there is no double counting.

Figure 5-9: Events passing intermediate cuts (black) in mass window 5.0 – 5.5 MeV/c^2 where kaons are selected. Events from this intermediate set that pass the tight mass cut are shown in blue. Events from the intermediate set passing the particle identification cuts are shown in red.

The reduction power of the uncorrelated mass and particle identification cuts are then deduced. This is done by first making an intermediate set of cuts between the pre-selection and trigger and the full set of selection cuts in order to increase statistics. It is required that $\chi^2 < 10$, $\mathrm{IP_B}/\sigma_{\mathrm{IP_B}} < 5$ and $\mathrm{L}/\sigma_{\mathrm{L}} > 10$, which leaves a sample of 1601 events for the $\mathrm{B_d^0} \to \mathrm{K^+K^-}$ selection and 860 for the $\mathrm{B_s^0} \to \pi^+\pi^-$ selection. The tight mass cut and the particle identification cuts are then applied separately to the set of events that pass these intermediate cuts.

Figure 5-9 shows in black the 1601 events that survive the intermediate selection cuts from the $\mathrm{B_d^0} \to \mathrm{K^+K^-}$ selection. In blue, the 218 events from this set that survive the tight mass cut are shown giving the reduction power of the tight mass cut as 218/1601. The 23 events which survive the intermediate cuts and the particle identification cuts are shown in red. This gives the reduction power of this cut to be 23/1601 and also indicates that the particle identification cut is indeed uncorrelated with invariant mass within the statistics of this study. The upper limit on background events in a sample of this size, taking account of the reduction power of the invariant mass and particle identification requirements is $x_{up} = 0.016$ to a 90% confidence level.

The invariant mass distribution of the 860 events that pass the intermediate cuts for the $B_s^0 \to \pi^+\pi^-$ selection is shown in Figure 5-10. The events which pass the intermediate cuts and the tight invariant mass cut are shown in blue, showing the reduction power of this cut to be 108/860. The events that pass the intermediate cuts and then the particle identification cuts are shown in red in the figure. The particle identification cuts have a reduction power of 222/806. Applying these factors gives an

Figure 5-10: Events passing intermediate cuts (black) in mass window 5.0 – 5.5 MeV/c^2 where pions are selected. Events from this intermediate set that pass the tight mass cut are shown in blue. Events from the intermediate set passing the particle identification cuts are shown in red.

upper limit, $x_{up} = 0.34$ events to a 90% confidence level.

5.2.8 Estimates of observation significance

Using the results of background studies described above it is possible to place a lower limit on the signal to background ratio for each channel and absolute background level. For $B_d^0 \rightarrow K^+K^-$ taking values from Table 5.5 the annual contribution from two-body backgrounds is 399 events. The upper limit on the contribution from combinatorial background is calculated to be $x_{up}=0.016$. This limit comes from a sample of background events containing 4.3×10^6 events. At LHCb 10^{12} $b\overline{b}$ events are expected each year giving an annual upper limit to the number of events coming from combinatorial background to be 3.7 k. The total background from both sources is therefore 4.1 k events and the signal to background ratio, $S/B = 1872/4.1\text{k} = 0.46$. In order to claim a signal observation it is conventional to require that there is an excess of 5σ above the background expectation. One must take into account possible fluctuations in signal and background and therefore require that $S/\sigma_{tot} > 5$ where σ_{tot} is the total uncertainty on signal and background. Calculating σ_{tot} gives

$$\begin{gathered}\sqrt{\left(\frac{\sqrt{S}}{S}\right)^2+\left(\frac{\sqrt{B}}{B}\right)^2} > 5 \\ \frac{S}{\sqrt{S+B}} > 5.\end{gathered} \qquad 5.4$$

A signal in excess of $5\times\sqrt{1872+4.1\text{k}} = 386$ is therefore required. With a signal yield of 1872 events the observation of an excess above the background is expected in less than one year of operation.

For $B_s^0 \to \pi^+\pi^-$, reading from Table 5.6 the expected annual contribution to the background from two-body decays is 634 events. The upper limit on the combinatorial background contribution is 79.0 k, giving a total background of 79.6 k. In order to be sure that the events observed are not due to a fluctuation in the background distribution we require a greater number of signal events than $5 \times \sqrt{2697 + 79.6\mathrm{k}} = 1434$. With an expected signal yield of 2697 events, an observation within a year of running is also possible for this mode.

The procedure has been repeated for the case where the branching ratio for each channel is reduced by a factor of 10. Table 5.10 summarises the efficiencies and expected signal and background yields for one year of running. The table also contains the number of years running required in order to make an observation for each value of the assumed branching ratio. These numbers show clearly that although $B_d^0 \to K^+K^-$ has a smaller branching ratio, an observation is expected after a shorter amount of running. This is due to the fact that because of the information provided by the RICH it is easier to reject pairs of kaons than pairs of pions from the combinatorial background.

	Assumed BR	**ε (%)**	**Annual S**	**Annual $B_{\text{two-body}}$**	**Annual B_{comb}**	**Total annual B**	**Years for observation**
$B_d^0 \to K^+K^-$	0.48×10^{-6}	0.499	1872	399	3.7 k	4.1 k	0.21
	0.48×10^{-7}	0.395	148	102	1.1 k	1.2 k	1.24
$B_s^0 \to \pi^+\pi^-$	1.85×10^{-6}	0.725	2682	634	79.0k	79.6 k	0.53
	1.85×10^{-7}	0.351	130	144	44.1 k	44.3 k	8.11

Table 5.10: Summary of efficiencies and annual signal and background yields for a given branching ratio. The number of years of running needed in order to make a reliable observation is given in the final column.

5.3 Estimating the CP sensitivity

In the previous section it has been demonstrated that it would be possible to make an observation of $B_d^0 \to K^+K^-$ and $B_s^0 \to \pi^+\pi^-$ at LHCb for the range of branching ratios considered. As discussed in Chapter 1, measurements of the branching ratios of these decays would give information about the relative contribution to other two-body decays from exchange and annihilation penguin processes. It could also be interesting to study the decay asymmetry of these channels. In this chapter a simple Monte Carlo study is used to show how well the CP asymmetry could be measured at LHCb for the decay channel $B_d^0 \to K^+K^-$, given the event yields and signal to background ratios found previously.

The CP asymmetry as a function of proper time, t, is given by,

$$A_{CP}(t) = \frac{\Gamma(B_d^0 \to K^+K^-)(t) - \Gamma(\overline{B}_d^0 \to K^+K^-)(t)}{\Gamma(B_d^0 \to K^+K^-)(t) + \Gamma(\overline{B}_d^0 \to K^+K^-)(t)}. \qquad 5.5$$

As was shown in Chapter 1 this is expected to take the form

$$A_{CP} = A \cdot \cos(\Delta mt) + B \cdot \sin(\Delta mt). \qquad 5.6$$

A Monte Carlo study is used in order to assess the statistical sensitivity to the parameters A and B. Δm is already well known and is fixed in the fit.

The number of events expected in 10 years are distributed in proper time according to relation 5.1 and with parameter μ fixed at 1.51, the value found by fitting the distribution shown in Figure 5-7. The true value of A_{CP} is calculated using equation 5.6 for fixed values of A and B. The values used in this study for these parameters are chosen to be A = 0.6, B = 0.8 and $\Delta m = 0.502\ \mathrm{ps}^{-1}$, where A and B are chosen arbitrarily and Δm is set to the current world average value [eid04]. The probability of a generated event having originated as a B_d^0, P_B, is calculated using the expression

$$P_B = \frac{1}{2}(A_{CP} + 1). \qquad 5.7$$

In order to introduce the expected statistical error which would be seen in the experiment, background and mis-tagged events are added to the generated sample. The

Figure 5-11: CP asymmetry for $B_d^0 \rightarrow K^+K^-$ decays in ten years of running.

background to signal ratio $\frac{B}{S} = 2.4$, calculated in the previous section, is used to determine the number of background events generated per signal event. Background events are distributed in proper time in the same way as the signal events. The percentage of events wrongly identified as B_d^0 or $\overline{B}_d^0$ after flavour tagging has been performed is known as the mis-tag fraction, ω. Studies of the full Monte Carlo simulation found ω for some two-body B decays. Table 9.8 in [lhcb03] shows that ω does not vary within the errors for two-body decays. For $B_d^0 \rightarrow K^+K^-$ ω was not calculated and the most conservative value, ω = 34.9%, calculated for $B_d^0 \rightarrow \pi^+\pi^-$ is used in this case. The resulting asymmetry distribution after generating the number of events expected in 10 years is shown in Figure 5-11.

The distribution has been fitted using the following function which takes into account the presence of background contamination and mis-tag probability [eid04]

$$A_{CP_{eff}} = \frac{1}{1-2\omega}\frac{1}{1+\frac{B}{S}}\left(A\cdot\cos\Delta mt + B\cdot\sin\Delta mt\right). \qquad 5.8$$

The fit is an unbinned maximum likelihood, with the likelihood function given by expression 5.8. Five hundred simulated experiments are performed. The distributions of the values found for the two parameters are shown in Figure 5-12 along with the Gaussians that have been fitted to the distributions. The central values of the fits are close to the input value in each case. The widths of the distribution indicate that if such a fit was made after 10 years of data taking, a determination of the parameters A and B

cc

Figure 5-12: The results of the log-likelihood fit for the parameters A and B. The distributions are fitted with a Gaussian; A is centred at 0.59 with width 0.08, B is centred at 0.81 with width 0.12.

Figure 5-13: The pull distributions for the two fitted parameters. The distributions are fitted with a Gaussian; for A the fit is centred around −0.07 with width 0.94 and for B it is centred around 0.04 with width 1.01.

The 'pull' on each of these distributions is calculated using the following expression

$$\text{pull}=\frac{x-x_{\text{true}}}{\text{err}_x} \qquad 5.9$$

where x is the result of the log-likelihood procedure for the parameter, x_{true} is the value used as an input to the toy Monte Carlo and err_x is the error on the result. The pull is expected to be centred around 0 with width approximately equal to one for an unbiased fit with well assigned errors. The assigned errors coming from the fit are in general asymmetric. In calculating the pulls the negative error is used if $x > x_{\text{true}}$ and the positive error is used if $x < x_{\text{true}}$. The width of each distribution is close to one in each case indicating that the estimate of the errors is correct.

Using the background to signal ratio calculated in the previous section as an input this study indicates that after 10 years of data taking at LHCb the parameters A and B could be determined with a precision of ± 0.15.

5.4 Discussion of results

In the case where there is no direct CP violation the parameter B would simply be equal to sin2α and if B = 0.8, α would have a value of 26.6°. An error on the measurement of B of ± 0.15 would limit α between 20° and 45°.

In order to properly account for the penguin diagrams a the results from $B_d \rightarrow K^+K^-$ and $B_s \rightarrow \pi^+\pi^-$ combined [fle04]. For this to be possible CP violation has to be measured in $B_s \rightarrow \pi^+\pi^-$. This would be harder than in the case of $B_d \rightarrow K^+K^-$ due to a lower signal significance and the fact that the asymmetry is diluted by the fast B_s oscillation. However, if this were achieved a determination of γ would be possible. As the diagrams contributing to this case are very different to those contributing to $B_d \rightarrow \pi^+\pi^-$ and $B_s \rightarrow K^+K^-$ the γ found in the two cases could be significantly different.

The results found here come from a simulation which does not model the response of the LHCb detector perfectly. At the start of LHCb running there will be difficulties understanding the detector performance. There will however be many control signals that can be used for calibration, such as life time unbiased J/Ψ particles and many $D^*(D^0\pi, D^0 \rightarrow K\pi)$ events. These can be used to calibrate, for example, vertex resolution, proper time resolution, mass resolution, particle identification. The analysis done here is also limited by the low statistics, particularly in the case of the asymmetry study.

5.5 Conclusion

An observation of the decay channels $B_d^0 \rightarrow K^+K^-$ and $B_s^0 \rightarrow \pi^+\pi^-$ can be made within one year of data taking at LHCb if the branching ratios are assumed to be one tenth of $B_d^0 \rightarrow \pi^+\pi^-$ and $B_s^0 \rightarrow K^+K^-$ respectively. An observation would still be possible if the branching ratios were a factor of 10 smaller and would be achieved using tighter particle identification cuts and would require an increased amount of time. In this case success would rely heavily on the particle identification performance of the RICH system.

Although $B_d^0 \rightarrow K^+K^-$ and $B_s^0 \rightarrow \pi^+\pi^-$ are primarily interesting because of the information they can provide on the contribution of exchange and annihilation penguin processes to $B_d^0 \rightarrow \pi^+\pi^-$ and $B_s^0 \rightarrow K^+K^-$, if an observation of these decays is made within a year of data taking at LHCb it may be interesting to go on to measure the CP asymmetry in these channels. The results of a simple simulation study show that with 10 years worth of data at LHCb, the parameters A and B could be determined with an error of 20 %.

Chapter 6

Conclusions

CP violation in the B sector has become an established phenomenon and as a result of the work done by the B factories, one of the angles of the unitarity triangle is now very well constrained through the measurement of sin2β in the decay of $B_d \rightarrow J/\psi K_s$. LHCb will build on the work done at the B factories by exploiting the large number of $b\overline{b}$ pairs that will be created at the LHC. The high statistics will give access to rare decays and make precision measurements of already known parameters possible. The B_s sector will also be available for study at LHCb where work initiated at the Tevatron will be continued.

LHCb is designed to fully exploit the potential of the LHC for B physics. In particular it will benefit from its dedicated trigger system, its excellent proper time resolution, and the hadron identification provided by the RICH system. The development and evaluation of aspects of the RICH system have been the topic of this thesis. This chapter briefly reviews what has been learnt in this work, and the next steps for LHCb.

6.1 HPD Development

The HPD has been chosen as the photodetector to be used in the LHCb RICH system. The HPDs must be reliable and efficient, detecting single photons at the LHC bunch crossing rate over 10 years. During the production of two prototype 40 MHz HPDs, the results following each stage of the production process have been analyzed.

This analysis highlighted the presence of a problem with the process of attaching sensor and readout chips. The formation of crusts on the bump-bonds made attaching the two chips difficult and resulted in a number of good bonds lower than specifications. The reason for the formation of the crusts has been identified and a new process has been developed. This process has been shown to result in a number of good bonds that meets specifications.

Six hundred HPDs will be produced for the LHCb experiment and this process is now underway. Testing procedures for each stage of the production process have been defined as a result of the studies made for the prototype production. It is vital that the selection procedure at each stage works well as this will ensure that only the most efficient anodes are chosen for HPD fabrication. The RICH detector can then be equipped with photodetectors that will provide high photon detection efficiency.

6.2 The Analogue Pilot

The electronics used to read out data from the HPDs used in laboratory testing will not be the solution used in LHCb. Electronics for reading out the HPDs in the LHCb RICH have been developed and the Analogue Pilot chip forms part of that system. The Analogue Pilot will provide 6 reference voltages needed by the HPD readout chip.

Studies of the Analogue Pilot have shown that the reference voltages provided are dependent on temperature. The values of the references can be read back by an ADC on board the chip, however studies have also shown that there can be an offset between the true reference value and the value read back by the ADC.

The tests conducted in this thesis need to be carried out on a large sample of chips in order to come up with a final calibration strategy for the Analogue Pilot. It should be verified that the reference voltages vary linearly with temperature for such a sample. The tests should also establish if the offset seen between the ADC read back value and the actual value is constant for all chips, or whether it varies from chip to chip. It can then be decided what information needs to be stored for each chip in order to be able to calculate precise values of the six reference voltages when LHCb is operating.

6.3 HPD and Aerogel Performance

Two prototype 40 MHz HPDs were produced using anodes selected from the first batch of anode assemblies produced. These prototypes have been tested in beam conditions on two occasions.

The prototype HPDs were first tested individually, using air as the Cherenkov radiator. The detectors exhibited a good photoelectron detection yield which had the expected dependence on high voltage and discriminating threshold. The two readout modes of the detectors, Full and LHCb, were tested and the results compared. Further comparison with a Monte Carlo calculation shows that no significant losses are introduced as a result of readout in LHCb mode.

The second beam test used both 40 MHz prototypes together with a third 10 MHz prototype HPD. This array of three HPDs was tested in conjunction with the Cherenkov radiator aerogel. The HPDs again demonstrated good photoelectron detection efficiency. A comparison between the results of these beam tests and a detailed Monte Carlo simulation has been made. Reasonable agreement is seen between the Monte Carlo with the data, with the two 40 MHz prototype HPDs showing a 10 – 15 % loss with respect to Monte Carlo and a 30 % loss in the 10 MHz prototype. Small losses in the number of photoelectrons per ring would not lead to a significant degradation in particle identification performance [lhcb03].

A larger batch of HPD prototypes will be produced before the final six hundred HPDs are produced. The prototypes tested here were made using anodes from the batch in which the crusted bump-bonds were discovered. The next set of prototypes will be made using anodes made with the modified procedure and higher photoelectron detection efficiencies would be expected. The larger number of prototypes available will mean that beam tests using an array of HPDs will be possible. Tests could be performed with the detectors arranged in a close packed array and read out using the electronics designed for use in the experiment. Such a test will give greater insight into the challenges faced in constructing and using the RICH detector and a better indication of performance.

6.4 Search for rare decay modes

It has been shown that an observation of the rare decay modes $B_d \to K^+K^-$ and $B_s \to \pi^+\pi^-$ will be possible within one year of nominal LHCb operation assuming branching ratios one tenth of that for $B_d \to \pi^+\pi^-$ and $B_s \to K^+K^-$ respectively. If these branching ratios were a further factor of ten smaller, an observation would also be possible using tighter requirements on the particle identification information provided by the RICH system. In this case an observation would require a greater length of time;

1.2 years in the case of $B_d \to K^+K^-$ and 8.1 years for $B_s \to \pi^+\pi^-$. In both cases, the analysis exploits the high performance expected from the RICH system.

It will be important for LHCb to map out as precisely as possible the relative branching ratios of all the charged two-body decay modes and to measure CP asymmetries where possible. This may allow for hadronic contributions to be better understood in the key decay modes such as $B_d \to \pi^+\pi^-$.

Appendix A

A requirement of a Cherenkov radiator for a RICH detector is that scattering of the photons should be minimal, as this will lead to a reduced precision of the measurement of the Cherenkov angle. Photons are known to undergo Rayleigh scattering in the aerogel. This scattering can be described by considering that a photon is scattered by an electron, which is described as an individual small dielectric sphere [jac75]. The incident field is given by

$$\overline{E}_{inc} = \overline{\in}_0 E_0 e^{ik\overline{n}_0 \cdot \overline{x}} \qquad (A.1)$$

where $\overline{n}_0$ is the unit vector describing the incident direction, $\overline{\in}_0$ is the incident polarization vector and $k = \omega/c$ where ω is the angular frequency. The resulting scattered wave far away from the electron is given by

$$\overline{E}_{sc} = k^2 \frac{e^{ikr}}{r}[(\overline{n} \times \overline{p}) \times \overline{n}] \qquad (A.2)$$

where the unit vector $\overline{n}$ describes the direction of observation, r is the distance from the scatterer and $\overline{p}$ is the dipole field induced in the small scatterer by the incident field. The differential cross section for scattering is given by

$$\frac{d\sigma}{d\Omega}(\overline{n}, \overline{\in}; \overline{n}_0, \overline{\in}_0) = \frac{r^2 \left| \in^* \cdot \overline{E}_{sc} \right|^2}{\left| \in_0^* \cdot \overline{E}_{inc} \right|^2} \qquad (A.3)$$

where $\overline{n}$ and $\in$ are the direction and polarization vector respectively after scattering. Substituting equations A.1 and A.2 into A.3, this can be written

$$\frac{d\sigma}{d\Omega}(\overline{n},\overline{\in},\overline{n}_0,\overline{\in}_0)=\frac{k^4}{E_0^2}\left|\overline{\in}^*\cdot\overline{p}\right|^2$$

The electric dipole moment of a small dielectric scattering sphere is

$$\overline{p}=\left(\frac{\in-1}{\in+2}\right)a^3\overline{E}_{inc}$$

and the differential scattering cross section becomes

$$\frac{d\sigma}{d\Omega}=k^4a^6\left|\frac{\in-1}{\in+2}\right|^2\left|\overline{\in}^*\cdot\overline{\in}_0\right|^2$$

The scattered radiation is linearly polarized in the plane defined by $\overline{\in}_0$ and $\overline{n}$. This leads to the expression for the differential cross section, summed over the scattered polarisation

$$\frac{d\sigma}{d\Omega}=k^4a^6\left|\frac{\in-1}{\in+2}\right|^2\tfrac{1}{2}(1+\cos^2\theta) \qquad \text{(A.4)}$$

Individual scatterings of photons in the aerogel follow this relation. The differential cross-section is proportional to k^4, or inversely proportional to λ^4, so that photons produced at lower wavelengths are more likely to scatter. The expected scattered distribution has a $\cos^2\theta$ shape peaked around 242 mrad.

Appendix B

An experiment counts events that follow a Poisson distribution. If in one such experiment n events are counted, an upper limit can be placed on the mean of the distribution being counted to a certain confidence level. Using the Neyman construction for confidence intervals [eid04] the probability that x lies between x_1 and x_2 is given by $P(x_1 < x < x_2) \equiv 1 - \alpha$, which is

$$P(x_1 < x < x_2) = 1 - \alpha = \int_{x_1}^{x_2} f(x;\theta)dx$$

where $f(x;\theta)$ is a probability distribution function with x being the outcome of the experiment and θ the unknown mean of the distribution. Setting $x_2 = \infty$ and $\alpha = 0.9$ x_1 becomes an upper limit, x_{up}, where the probability of θ exceeding x_1 is 10 %.

$$1 - \alpha = \int_{x_1}^{\infty} \frac{\theta^x}{x!} e^{-x} dx$$

can be expressed

$$\alpha = e^{-x_{up}} \sum_{m=0}^{n} \frac{x_{up}^m}{m!}$$

which can be solved numerically. This equation can be solved numerically to give x_{up} for different n and these values can be found in tables.

References

[alb98]
E. Albrecht *et al.*, Nucl. Instr. and Meth. A 411 1998.

[all03]
J. Allison *et al.*, GEANT4 – a simulation toolkit, NIM A 506 2003.

[bab01]
BaBar Collaboration, Observation of CP violation in the B^0 system, Phys. Rev. Lett. 87 2001.

[bab02]
BaBar Collaboration, Measurements of Branching Fractions and CP-violating Asymmetries in $B^0 \to \pi^+\pi^-, K^+K^-, K^+K^-$ decays, Phys. Rev. Lett. 89 2002.

[bel01]
Belle Collaboration, Observation of large CP violation in the neutral B meson system, Phys. Rev. Lett. 87 2001.

[bib04]
J. Bibby *et al.,* The Readout Electronics of the LHCb RICH detectors, LHCb 2004-067.

[bor99]
M. Born, E. Wolf, Principles of Optics, Cambridge University Press, 7th Edition, 1999.

[bro74]
A. P. Brpkaw, "A simple three-terminal IC bandgap reference, IEEE J. Solid-state Circuits, 6, 1974.

[bru96]
R. Brun and F. Rademakers, ROOT – An Object Oriented Analysis Framework, Proceedings AIHENP'96 Workshop, Lausanne, Sep. 1996, Nucl. Inst. & Meth. in Phys. Res. A 389 1997.

[cab63]
N. Cabibbo, Unitary Symmetry and leptonic decays, Phys. Rev. Lett. 10 1967.

[cal05]
M. Calvi *et al.*, Test Beam results from a RICH detector prototype using aerogel radiator and pixel hybrid photon detectors, as yet unpublished.

[cam04]
Private communication from Michael Campbell (CERN).

[cdf04]
CDF Collaboration, Search for $\Lambda_b \to pK$ and $p\pi$ decays, CDF note 7143.

[chr64]
J. H. Christenson, *et al.*, Evidence for the 2π decay of the K(2)0 meson, Phys. Rev. Lett. 13, 1964.

[cho03]
P. Chochula *et al.*, The Alice Silicon Pixel Detector, Nucl. Phys., A 715 2003.

[ckm05]
The CKM Fitter Group, CP violation and the CKM Matrix: assessing the impact of the asymmetric B factories, Eur. Phys. J. C 41, 2005.

[dan99]
A. Danilyuk *et al.*, Synthesis of aerogel tiles with high light scattering length, Nucl. Intstr. Meth. A 433, 1999.

[dar75]
E. H. Darlington, Back-scattering of 10-100 keV electrons from thick targets, J. Phys D 8 1975.

[eas04]
Produced by Sajan Easo, 2004.

[eid04]
S. Eidelman *et al.*, Phys. Lett. B 592, pages 104-185, 2004.

[eli04]
J. Ellis, Physics at the LHC, Eur. Phys. J C 34 2004.

[ell90]
N. Ellis and Anne Kernan, Heavy quark production at the CERN $p\bar{p}$ collider, Phys. Rep. 195, 1990.

[fle99]
R. Fleischer, New strategies to extract β and γ from $B_d \rightarrow \pi^+\pi^-$ and $B_s \rightarrow K^+K^-$, Phys. Lett. B 459 1999.

[fle04]
R. Fleischer *et al.*, Anatomy of Prominent B and K Decays and Signatures of CP-violating New Physics in the Electroweak Penguin Sector, Nucl. Phys. B697 2004

[for98]
R. Forty and O. Schneider, RICH Pattern Recognition, LHCb 1998-040.

[jac75]
J. D. Jackson, Classical Electrodynamics, 2nd Edition, John Wiley & Sons Inc., 1975.

[gla61]
S. L. Glashow, Partial symmetries of weak interactions, Nucl. Phys. 22, 1961.

[gui02]
A. Guirao *et al.*, Readout of high speed S-LINK data via a buffered PCI card, 4th International Workshop on Personal Computers and Particle Accelerator Controls 14-17 October 2002, Frascati(Italy).

[gys00]
T. Gys *et al.*, Performance of hybrid photon detector prototypes with 80% active area for the RICH counters of LHCb, Nucl. Instrum. Methods Phys. Res., A 442 2000.

[har98]
Editors P. F. Harrison and H. R. Quinn, The BaBar Physics Book, SLAC-R-504, October 1998.

[kob72]
M. Kobayashi and T. Maskawa, CP violation in the renormalizable theory of the weak interaction, Prog. Theor. Phys. 49 1972

[lhcb98]
LHCb Collaboration, LHCb Technical Proposal, LHCC 1998-4, 20 February 1998.

[lhcb00]
LHCb Collaboration, LHCb Calorimeters, LHCb TDR 2, 6 September 2000.

[lhcb03]
LHCb Collaboration, LHCb Technical Design Report, LHCC 2003-030, 9 September 2003.

[lhcbt03]
LHCb Collaboration, LHCb Trigger System technical Design report, 9 September 2003.

[lhcb05]
LHCb Collaboration, DAVINCI – The LHCb Analysis programme, http://lhcb-comp.web.cern.ch/lhcb-comp/Analysis.

[lyo92]
L. Lyons, Statistics for nuclear and particle physicists, Cambridge University Press, 1992.

[moh01]
R. Mohanta *et al.*, Charmless two-body decays of the Λ_b baryon, Phys. Rev. D Vol. 63, 2001.

[mor04]
Measurements made at CERN by M. Moritz *et al.*

[pal97]
E. Palik, Handbook of optical constants of solids, Academic Press (Inc.) London, v. 1-5, 1997.

[pap00]
A. Papanestis *et al.*, Monitoring alignment and control of the RICH detectors, LHCb 2000-80

[rich00]
LHCb Collaboration, LHCb RICH Technical Design Report, LHCC 2000-037.

[sak67]
A. D. Sakharov, Zh. Eksp. Teor. Fiz. Pis'ma Red. 5,32 (JETP Lett., 5 24) 1967.

[sal68]
A. Salam, Weak and electromagnetic interactions, Elementary Particle Theory, Proceedings of the Nobel Symposium held 1968 at Lerum, Sweden, edited by N. Svartholm, Amkvist and Wiksell, Stockholm, 1968.

[sch05]
Private Communication from Olivier Schneider (CERN).

[sjos01]
T. Sjöstrand *et al.*, Computer Physics Commum. 135 2001.

[teu05]
Frederick Teubert,LHCb Trigger Working Group, Private communication

[vag03]
V. Vagnoni *et al.*, Selection of $B^0_{(s)} \to h^+h^-$ decays at LHCb 2003-123.

[vag203]
V. Vagnoni *et al.*, CP sensitivity with $B^0_{(s)} \to h^+h^-$ decays at LHCb, LHCb 2003-124.

[wei67]
S. Weinberg, A model of leptons, Phys.Rev.Lett. 19, 1967.

[wol83]
L. Wolfenstein, Parameterization of the Kobayashi-Maskawa matrix, 51, 1983.

[wu57]
C. S. Wu *et al.*, An experimental test of parity conservation in beta decay, Phys. Rev. 105, 1957.

[wyl98]
K. Wyllie, The design and development of radiation-tolerant silicon microstrip detectors for tracking at the future large hadron collider, RAL-TH-1998-013 October 1998, Phd Thesis.

[wyl01]
K. Wyllie *et al.*, LHCb Pixel Chip Review Documentation, June 2001, Available: http://kwyllie.home.cern.ch/kwyllie/pixel_doc/review.pdf.